The Dissertation Committee for Junfei Li

certifies that this is the approved version of the following dissertation:

Model-Based Signal Processing for Radar Imaging of Targets with Complex Motions

Committee:

Hao Ling, Supervisor

Melba M. Crawford

Mercea D. Driga

John A. Pearce

Edward J. Powers

Model-Based Signal Processing for Radar Imaging of Targets with Complex Motions

by

Junfei Li, BSEE, MSEE

Dissertation

Presented to the Faculty of the Graduate School of
the University of Texas at Austin
in Partial Fulfillment
of the Requirements
for the Degree of
Doctor of Philosophy

The University of Texas at Austin
August 2002

ProQuest Information and Learning Company
300 North Zeeb Road
PO Box 1346
Ann Arbor, MI 48106-1346

To my wife Ning and daughter Cara

Acknowledgements

First, I would like to thank my thesis advisor, Professor Hao Ling for his guidance and mentorship, both academically and personally. Without the numerous interesting and enlightening discussions with him, this work would be impossible. His continued support will be remembered for the many years to come.

I also appreciate Professors Melba Crawford, Mercea Driga, John Pearce, and Edward Powers for graciously giving of their time to serve on my dissertation committee and for their welcomed comments and suggestions.

I acknowledge the support from Office of Naval Research under contract No. N00014-98-1-0615. I would like to thank Dr. Victor Chen with Naval Research Laboratory for his help with the data.

I would like to thank all of the students, faculty, and staff for your help and support over my stay here at the University of Texas at Austin. I would most especially like to thank Drs. Yuanxun Wang and Tao Su for all the helps and good company.

My family deserves special thanks, since they have supported me a lot longer than the duration of this research. My parents were always there for me if needed. To Ning, I express my deepest appreciation. Your unconditional love, constant encouragement, and unwavering devotion sustained me during the many long days of this hard process.

Model-Based Signal Processing for Radar Imaging of Targets with Complex Motions

Publication No. ___________________

Junfei Li, Ph.D.
The University of Texas at Austin, 2002

Supervisor: Hao Ling

Model-based signal processing for inverse synthetic aperture radar (ISAR) imaging of targets with complex motions is proposed in this dissertation. Target motion is the most important issue in radar imaging of an unknown target. Although widely recognized as a promising tool in target recognition, ISAR imaging is not yet fully operational in real-world data processing. This is mainly due to the fact that an unknown target, especially a non-cooperative target could have complex motions.

First, the performance of existing motion compensation algorithms is evaluated. For this purpose, three sets of radar images of an aircraft, including blind motion compensated images, truth motion compensated images, and predicted images using electromagnetic-code simulation are generated. The limitations of existing radar imaging algorithms are identified after a comparison of the radar images.

The remaining part of this research focuses on how to overcome these limitations. This is achieved by performing target feature extraction in the presence of complex motions, including three-dimensional (3D) motion, non-rigid body motion and high order motion. For a target with non-planar motion, an algorithm based on the phase analysis of multiple point scatterers is proposed to blindly detect the existence of 3D motion from radar data. An adaptive feature extraction technique is also applied for 3D ISAR image reconstruction from undersampled radar data when the target pose data is known. For a target with non-rigid body motions, adaptive chirplet signal representation is used to first separate signals from the main body and the rotating parts. Better extraction of target geometric features and micro-Doppler features are achieved after individual processing of the separated signal. For a target with high order motions, genetic algorithms are used to replace exhaustive search to reduce the computational time.

Throughout the research, the use of physical models is emphasized for better understanding of the radar data. Model-based processing, including adaptive joint time-frequency techniques and genetic algorithms are applied in the information extraction process. Point scatterer simulations are extensively used to test the correctness and to demonstrate the concept of the proposed methods. Results from measurement data are included to demonstrate the effectiveness of the work on real-world problems.

Table of Contents

Acknowledgements-- v

List of Figures --- xi

Chapter 1 Introduction -- 1

1.1 The problem of ISAR imaging -- 1

1.2 Background knowledge --- 5

1.3 Motivations--- 12

1.4 Organization -- 13

Chapter 2 Comparison of high-resolution ISAR imagery from measured data and synthetic signatures -- 15

2.1 Introduction --- 15

2.2 Measured and synthetic image generation-- 17

2.3 Image comparisons-- 23

2.4 Problematic areas-- 26

2.5 Conclusions --- 30

Chapter 3 An algorithm to detect the presence of 3D target motion from ISAR data -- 32

3.1 Introduction --- 32

3.2 2D and 3D motion models --- 34

3.3 Problem of existing motion compensation algorithms with 3D target motion -- 36

3.4 3D Motion detection algorithm --- 40

3.5 Results -- 47

3.6 Conclusions -- 55

Chapter 4 3D ISAR Image reconstruction of a target with motion data using adaptive feature extraction--- 56

4.1 Introduction -- 56

4.2 3D point scatterer model --- 59

4.3 Adaptive feature extraction algorithm--- 60

4.4 Results --- 63

4.5 Conclusions -- 73

Chapter 5 ISAR feature extraction from non-rigid body targets using adaptive chirplet signal representation-- 75

5.1 Introduction -- 75

5.2 Signal model and formulation --- 77

5.3 Point scatterer simulation results-- 86

5.4 Measurement data results --- 90

5.5 Conclusions -- 97

Chapter 6 Use of genetic algorithms in ISAR imaging of targets with higher order motions -- 99

6.1 Introduction -- 99

6.2 ISAR motion compensation using joint time-frequency projection ------------- 100

6.3 Use of genetic algorithms for phase parameter search----------------------------- 103

6.4 Point scatterer simulation --- 107

6.5 Measurement data processing -- 110

6.6 Conclusions --- 115

Chapter 7 Conclusions -- 117

7.1 Summary -- 117

7.2 Contributions-- 119

7.3 Further work --- 121

Bibliography-- 123

Vita --- 132

List of Figures

Fig. 2.1 Fine motion compensation is carried out by extracting the Doppler frequency versus dwell time behavior of the strong point scatterer in the signal.

Fig. 2.2 Trajectory of a strong scatterer in the (dwell time)-(Doppler-frequency) plane from measured data. (a) Before JTF motion compensation. (b) After JTF motion compensation.

Fig. 2.3 Global and local coordination systems of the problem (figures not drawn to scale).

Fig. 2.4 Shooting and bouncing ray technique for radar signature simulation.

Fig. 2.5 ISAR images from: (a) JTF-mocomp, (b) GPS reference, and (c) Xpatch-synthetic.

Fig. 2.6 Correlation coefficients between JTF and GPS images, and between JTP and Xpatch images.

Fig. 2.7 Correlation between JTF and Xpatch images after JEM removal.

Fig. 2.8 Effect of imaging plane variation on ISAR image.

Fig. 3.1 Illustration of 2D motion vs. 3D motion.

Fig. 3.2 Phase linearization achieved by rotational motion compensation (a) Phases of two point scatterer with 2D rotational motion. (b) Both phases are linearized with rotational motion compensation. (c) Phases of two point scatterers with 3D motion. (d) Only one phase is linearized with rotational motion compensation.

Fig. 3.3 Problem with a typical motion compensation algorithm (a) Target undergoes a 2D motion. (b) Image after translational motion compensation. (c) Image after rotational motion compensation. (d) Target undergoes a 3D motion. (e) Image after translational motion compensation. (f) Image after rotational compensation.

Fig. 3.4 (a) (Dwell time)-(Doppler frequency representation of radar signal in a range cell with three point scatterers. (b) The basis function that is best matched to the dominant point scatterer is found by the AJTF project method.

Fig. 3.5 Measure of the nonlinearity of two phase functions.

Fig. 3.6 Effect of the number of point scatterers used on 3D motion detection result.

Fig. 3.7 Data processing flow chart.

Fig. 3.8 (a) Detected 3D motion from simulated radar data. (b) Degree of 3D motion from truth motion data.

Fig. 3.9 (a) Detected 3D motion from aircraft radar data. (b) Degree of 3D motion from truth motion data.

Fig. 3.10 3D motion and resulting ISAR image (frame 18).

Fig. 3.11 3D motion and resulting ISAR image (frame 14).

Fig. 3.12 2D motion and resulting ISAR image (frame 2).

Fig. 3.13 Frame no.11 showing focused ISAR image with 3D motion.

Fig. 3.14 3D motion detection result from radar data of a ship (a) Detected 3D motion. (b) ISAR image from frame 3. (c) ISAR image from frame 14. (d) ISAR image from frame 20.

Fig. 4.1 Possible 3D motions encountered in real ISAR data collection. (a) Slight 3D motion deviating from 2D motion. (b) Severe wave-like 3D motion. (c) Multiple flight paths of 2D motion.

Fig. 4.2 Original 9 point scatterers within in one range cell. (a) (y, z) distribution . (b) y projection. (c) z projection.

Fig. 4.3 Reconstruction result using AFE. (a) Motion data in a 3 deg by 3 deg aperture. (b) (y, z) image. (c) y projection. (d) z projection.

Fig. 4.4 Reconstruction results using the Fourier transform. (a) (y, z) image. (b) y projection. (c) z projection.

Fig. 4.5 AFE reconstruction from data with a slight 3D motion. (a) Motion data. (b) (y, z) image. (c) y projection. (d) z projection.
Fig. 4.6 AFE reconstruction from data with a slight 3D motion based on a 2D motion model.

Fig. 4.7 Reconstruction results using AFE. (a) Motion data in a 3 deg by 0.3 deg aperture. (b) (y, z) image. (c) y projection. (d) z projection.

Fig. 4.8 Reconstruction using noisy data. (a) -20dB white noise in the radar data. (b) 1% randomness in the angular positions.

Fig. 4.9 Point scatterer representation of an aircraft. (a) 3D point scatterer representation. (b) Top view. (c) Side view. (d) Front view.

Fig. 4.10 3D motion data from an air target.

Fig. 4.11 3D image reconstructed by AFE based on the 3D motion model. (a) 3D view of the top 600 extracted point scatterers (b) Top view. (c) Side view. (d) Front view.

Fig. 5.1 (a) Joint time-frequency representation of a chirplet basis. (b) Distribution of chirplet parameters for the main body (blue) and rotation parts (red), and separation thresholds (dashed).

Fig. 5.2 Point scatterer representation of the original target consisting of five rigid points (1-5) and one rotating point (6) with strengths 2, 5, 2, 1, 1, and 3.33, respectively.

Fig. 5.3 Simulated ISAR image of the target with non-rigid body motion.

Fig. 5.4 Spectrogram of the radar signal through range cell 65.

Fig. 5.5 Spectrogram of the parameterized radar signal using 100 chirplet bases.

Fig. 5.6 Separated body and rotating part signal. (a) Spectrogram of the three main body scatterers. (b) Spectrogram of the rotating part.

Fig. 5.7 Reconstructed ISAR image using the main body signals only.

Fig. 5.8 Rotation rate estimation using autocorrelation. (a) Result from the rotating part signal after separation. (b) Result from the original signal before separation.

Fig. 5.9 ISAR imaging of an aircraft during frontal view.

Fig. 5.10 ISAR image of the aircraft with JEM lines.

Fig. 5.11 Aircraft body and JEM line separation. (a) Body ISAR image with Doppler frequency gating only. (b) Body ISAR image with Doppler rate gating only. (b) Body ISAR image based on both Doppler frequency and Doppler rate parameters. (d) Separated JEM signal.

Fig. 5.12 ISAR imaging of a walking person.

Fig. 5.13 Radar data after range compression.

Fig. 5.14 Spectrogram of the radar signal containing body and arm components.

Fig. 5.15 Separated signal components of (a) the body, and (b) the swinging arm.

Fig. 5.16 Arm swing rate estimation using autocorrelation. (a) After signal separation. (b) Before signal separation.

Fig. 6.1 Flowchart of GA.

Fig. 6.2 Examples of crossover and mutation operations in binary and real-coded GA. (a) Binary-coded GA. (b) Real-coded GA.

Fig. 6.3 GA for third-order phase estimation. (a) Multi-modal objective function. (b) GA convergence curves. (c) GA-estimated phase compared to the original truth phase.

Fig. 6.4 Performance of GA compared to exhaustive search. (a) Computational complexity as a function of the number of parameters. (b) Accuracy.

Fig. 6.5 Translation motion compensation applied to measurement data using a third-order motion model. (a) Image before fine motion compensation. (b) Binary-coded GA. (c) Real-coded GA. (d) Exhaustive search.

Fig. 6.6 Comparison of the performance of GA and exhaustive search using measurement data. (a) Projection value. (b) Computation time.

Fig. 6.7 Motion compensation example for another measurement data set. (a) Image after third-order translation motion compensation using real-coded GA. (b) Spectrogram of the signal in range cell 64.

Fig. 6.8 Higher-order translation motion compensation. (a) Image after fourth-order translation motion compensation using real-coded GA. (b) Spectrogram of the signal in range cell 64. (c) Spectrogram of the signal in range cell 71.

Fig. 6.9 Higher-order rotational motion compensation. (a) Image after fourth-order rotational motion compensation using real-coded GA. (b) Spectrogram of the signal in range cell 64. (c) Spectrogram of the signal in range cell 71.

Chapter 1 Introduction

1.1 The Problem of ISAR Imaging

Radar imaging is a technique to form a target image by processing radar data reflected from the target [1, 2]. A typical radar imaging system consists of a radar sensor, a radar platform, and an image formation processor. The radar sensor transmits the electromagnetic wave signal to the target and records the data returned from the target. Important radar parameters include carrier frequency, bandwidth, pulse repetition frequency (for pulsed radar), polarization, and power level. The radar platform carries the radar. Usually, a radar system is supported on a vehicle, a ship, an aircraft, or a satellite. Sometimes the radar platform steers the antenna pointing direction for the radar to observe the desired target or scene. The image formation processor converts the received raw signal into a focused image of the observed target. Imaging radar is a coherent system, meaning that the radar received both amplitude and phase information from the target. A correlation process based on an optical or digital system is usually used to focus the complex radar signal (I/Q) into a radar image.

1.1.1 Different Radar Imaging Modes

According to the configuration and operation modes, there are different types of imaging radar. The most common modes include synthetic aperture radar (SAR) and inverse synthetic aperture radar (ISAR). In SAR, the radar moves with the radar platform and the target is stationary. In ISAR, the radar is stationary while the target moves during the imaging interval. Recently, interferometric synthetic aperture radar (INSAR or IFSAR) is gaining increased interest in the radar remote sensing community. It is a special case of SAR and relies on two antennas or two repeating flights to get information on an extra third dimension of the scene.

Different modes of imaging radar operations lead to different applications. For example, satellite-borne SAR is useful for earth resources monitoring; ISAR is regarded as an effective tool for target identification; IFSAR is used to generate the digital elevation models of the Earth. Despite of their respective applications, SAR and ISAR are equivalent in theory because only the relative motion between the target and radar matters. Therefore, the problem ISAR imaging can be considered as equivalent to a SAR imaging problem [3].

However, the ISAR imaging problem is more challenging than SAR imaging. In SAR, the well-controlled radar platform motion is usually known. In ISAR, the target motion is unknown. Therefore, how to deal with unknown target motions is a critical issue in ISAR imaging.

1.1.2 Range and Cross-Range Resolution in ISAR Imaging

Resolution is the ability to resolve two neighboring objects by using an imaging system. High-resolution radar imaging is useful for target identification as it provides detailed information about the target. Unlike an optical camera that resolves the target in the two dimensions perpendicular to the sensor, an imaging radar actually resolves the target in the range-Doppler domain. Radar range resolution is due to frequency diversity. High range resolution is achieved by increasing the system bandwidth, usually through linear frequency modulation or step frequency modulation. The radar range resolution is related to the radar system bandwidth through

$$\rho_r = \frac{c}{2f_{bw}} \tag{1.1}$$

where ρ_r is the range resolution, c is the speed of light, f_{bw} is the system bandwidth.

Another independent observable variable of imaging radar is Doppler or range rate. Therefore, radar imaging is also called range-Doppler imaging. Doppler resolution is achieved by angular motion of the target. As will be seen later, when a rigid body target undergoes a uniform rotational motion, the target cross-range position is proportional to the Doppler frequency. In this case, the cross-range resolution is determined through

$$\rho_x = \frac{c}{2f_c\Theta} \tag{1.2}$$

where f_c is the radar carrier frequency and Θ is the target rotational angle extent during the imaging interval.

1.1.2 The Role of Target Motion in ISAR

Only the relative motion between the radar and the target is important in radar imaging. In ISAR imaging, this corresponds to the target motion since the radar is stationary. The effect of the target motion on ISAR imaging is two-fold. A desired target motion is needed for the Doppler or cross-range resolution. A radar image cannot be formed without the target motion in ISAR. However, undesired motions, unless compensated, lead to blurred ISAR images.

The desired motion for the target is to have uniform rotational motion only. Under this case, a simple 2D Fourier transform brings the radar data in (frequency, aspect angle) domain into (range, cross-range) domain after pulse compression. All other motions are undesired motions and are detrimental to the ISAR imaging process. For example, uncompensated translational motion causes range walk in the range direction while uncompensated non-uniform rotational motion causes image blurring in the cross-range direction.

It is rare for a real-world target to have the kind of ideal motion for ISAR image formation. Therefore, additional processing beyond the simple Fourier transform is needed. One way is to carry out motion compensation to remove the undesired motion from the radar data. The motion compensation process can be thought of as an operation on the radar in the (frequency, aspect angle) domain, after which radar data appears to come from a target with ideal motion. After the motion compensation process, a 2D Fourier transform can thus be applied to bring the radar data into a focused ISAR image. In this case, the main challenge is to develop a good motion compensation algorithm. Another way is to adopt a non-Fourier based method. In case motion compensation is difficult or even impossible, some model-based methods can still be applied to extract useful target information out of the radar data.

1.1.3 Applications

ISAR imaging in the microwave frequency range has several advantages over other types of imaging sensors. First, radar imaging has all-weather, day and night operation capability. The active electromagnetic wave used by radar does not rely on sunlight and can penetrate clouds. Second, the distance at which a target can be imaged by a radar system is usually greater than that of an optical system. Third, operating in the microwave frequency band, image radar can expose complimentary target information not seen in optical or infrared sensors.

These attractive traits make ISAR imaging a candidate tool in many military and civilian applications, including target identification, aircraft traffic control, landing assistance, and security.

1.2 Background Knowledge

This section provides the background of the research work while more specific examples can be found in later chapters. In an approximate form, the radar data are related to the target feature through a point scatterer model. The challenge of ISAR imaging is caused by unknown target motion in the phase term. Both translational and rotational motion compensation can be realized after phase estimation of one or more point scatterers on the target.

1.2.1 Point Scatter Model

In order to form a radar image of a target, how the radar data are generated from the target is needed to know first. A physical model is used to describe the interaction mechanism between the radar wave and the target. The imaging processor is based on this model. There are two problems associated with radar data processing. The forward problem is to generate the radar data given the target configuration. The inverse problem is to derive the target characteristics from the radar data. In both cases, the radar system parameters are given. ISAR imaging is an inverse problem while radar data simulation is a forward problem. In both the forward problem and the inverse problem, the underlying theory is the same.

The electromagnetic scattering model [4] is a full wave model based on electromagnetic theory. When the target is complex, the scattering model is usually in the form of a scattering integral equation. As it is based on the exact Maxwell's equations, it is rigorous. It can be used to simulate the radar data given the radar target and the radar system parameters. There exist electromagnetic prediction codes, e.g. Xpatch [5] and FISC [6], which can calculate radar responses from a complex target. While useful for the forward simulation problem, a full wave model is too complex to be used for radar imaging. This is because the inverse scattering problem is much more difficult than the forward scattering problem. Inverse scattering is inherently an ill-posed problem.

To make things easier, ideal point scatterers are commonly used to represent a target. The effect of an ideal point scatter in space on the radar wave is characterized by a two-way time delay and a change in strength, i.e.

$$e_i = \sigma_i \exp(-j\frac{4\pi f}{c}d_i) \tag{1.3}$$

where f is the radar instantaneous frequency, c is the speed of light, and σ_i is the scattering coefficient. The distance from the radar to the i^{th} scatterer is d_i. As an equivalent SAR imaging problem, the target is fixed in space and the radar moves. Suppose the scatterer has position (x_i, y_i) and the radar moves with translation motion R and rotational motion Φ, d_i can be expressed into

$$\begin{aligned} d_i &= \sqrt{(R\cos\phi - x_i)^2 + (R\sin\phi - y_i)^2} \\ &\approx R - x_i\cos\phi - y_i\sin\phi \\ &\approx R - x_i - y_i\phi \end{aligned} \tag{1.4}$$

where far field and small angle approximations are used. When there are multiple scatterers, only first-order scatterering without the interaction between different scatterers are considered. In this case, the radar data can be assumed to be the summation of responses of each individual scatterer. From equations (1.3) and (1.4), the following equation is derived

$$E(f, t_D) = \sum_{i=1}^{Ns} \sigma_i \exp\{-j\frac{4\pi f}{c}[R(t_D) - x_i - y_i\phi(t_D)]\} \tag{1.5}$$

where t_D is the dwell-time (also called slow time), which corresponds to the radar pulse number. The target is assumed to consist of N_s scatterers.

From the point scatterer model in (1.5), if there is only uniform rotation motion of the target, meaning R is constant and Φ is a linear function of t_D, the radar image is a simple Fourier transform of the radar data E with respect to frequency f and dwell time t_D. However, when the target has undesired translation motion and non-uniform rotational motion, the so called motion compensation process is needed to form a focused ISAR image from the radar data.

1.2.2 ISAR Motion Compensation

For the real-world problem of ISAR imaging, where the target always has undesired motion, a direct Fourier transform cannot form a good ISAR image. Instead, motion compensation is needed to remove the undesired motion from the radar data. As the target motion can be decomposed into translation and rotational motion, the translation motion compensation and rotational motion compensation are usually carried out separately in the ISAR imaging process.

The first step is the coarse range alignment [1], which places the scatterers in their respective range cells. After range compression using the Fourier transform of the original radar data with respect to frequency, the resulting data in the range domain is called a range profile. Each range profile at a different dwell time is correlated with a reference range profile. Relative range shifts for all range profiles are then derived by examining the location of the maximum value of the correlation output. The range shift is then smoothed using a polynomial procedure to better approximate the actual translation motion. Suppose the final detected range shift is *$R_0(t)$*, the coarse range alignment is done by multiplying the conjugate of the phase term as follows

$$\begin{aligned} E(f,t_D) &= E(f,t_D)\exp[j\frac{4\pi f}{c}R_0(t_D)] \\ &= \sum_{i=1}^{Ns}\sigma_i \exp\{-j\frac{4\pi f}{c}[\Delta r(t_D) - x_i - y_i\phi(t_D)]\} \end{aligned} \tag{1.6}$$

where *$\Delta r(t_D)$* is the residual translation motion. After computing Fourier transform with respect to *f*, equation (1.6) becomes

$$E(r,t_D) = \sum_{i=1}^{Ns}\sigma_i \mathrm{sinc}[\frac{2\pi f_{bw}}{c}(r - x_i)]\exp\{-j\frac{4\pi f_0}{c}[\Delta r(t_D) - y_i\phi(t_D)]\} \tag{1.7}$$

where *f_0* and *f_{bw}* are the center frequency and the bandwidth of the radar, respectively. After range alignment, the residual translation motion is usually smaller than the range cell size and can be ignored in the *sinc* function. However, this term is still must be included in the phase as it is non-trivial compared to the wavelength of the radar. Therefore, further translation motion compensation is needed. Fine Doppler tracking [3] is designed to achieve this task. First, choose a range cell *r_0* with a prominent point scatterer. The radar signal through the particular range cell is

$$E_{r_0}(t_D) = \sum_m \sigma_m \exp\{-j\frac{4\pi f_0}{c}[\Delta r(t_D) - y_m\phi(t_D)]\} \tag{1.8}$$

where *m* is the index for different scatterers in the range cell. The phase of the prominent point scatterer is then estimated (the phase estimation problem will be discussed later). Fine Doppler compensation is done by multiplying the conjugate of the phase term to obtain

$$E(r,t_D)=\sum_{i=1}^{Ns}\sigma_i\mathrm{sinc}[\frac{2\pi f_{bw}}{c}(r-x_i)]\exp[+j\frac{4\pi f_0}{c}[(y_i-y_M)\phi(t_D)] \qquad (1.9)$$

where scatterer *M* is assumed to the prominent point scatterer for phase estimation. Up to this stage, the translation motion has been removed from the radar data. For rotational motion compensation, phase estimation of another point scatterer is needed. Suppose a phase estimation algorithm has been applied, the resulting phase would not be a linear function of dwell time due to the non-uniform rotational motion. Resampling in dwell time can make the phase function linear, i.e.

$$\varphi_N(t_D^{'})=\frac{4\pi f_0}{c}(y_N-y_M)\varpi t_D^{'} \qquad (1.10)$$

where $t_D^{'}$ is the newly defined dwell time after time resampling, ϖ is the effective rotation rate, and scatterer *N* is assumed to be the prominent scatterer with estimated phase φ_N. If the radar data is resampled at the new dwell-time, equation (1.9) becomes

$$E(r,t_D^{'})=\sum_{i=1}^{Ns}\sigma_i\mathrm{sinc}[\frac{2\pi f_{bw}}{c}(r-x_i)]\exp[+j\frac{4\pi f_0}{c}[(y_i-y_M)\varpi t_D^{'})] \qquad (1.11)$$

which can be mapped into a radar image by Fourier transforming with respect to $t_D^{'}$:

$$E(r,\chi)=\sum_{i=1}^{Ns}\sigma_i\mathrm{sinc}[\frac{2\pi f_{bw}}{c}(r-x_i)]\mathrm{sinc}\{\frac{2\pi f_c\Theta}{c}[\chi-(y_i-y_M)]\} \qquad (1.12)$$

where χ is the target cross range and Θ is the total aspect angle interval. From this equation, after the motion compensation, the target is correctly resolved in both range and cross range according to the target position. The well-known range and cross-range resolution expressed in equations 1.1 and 1.2 can also be easily derived from this equation.

Phase estimation is an indispensable step to achieve both translation and rotational motion compensation discussed so far. This is a challenging problem because the phase of one point scatterer is needed to be estimated in the presence of multiple point scatterers. Several phase estimation algorithms have been developed to address this problem. The phase gradient autofocus (PGA) method in [7] estimates the phase function by using its derivatives and uses an iterative zooming process to focus on the prominent point scatterer. RELAX in [8] uses an iteration process with positions and motions as unknown parameters alternatively. More recently, the joint time-frequency (JTF) method in [9-11] has been proposed as an effective tool to extract the phase information. The JTF algorithm assumes the phase function to be a polynomial function of dwell-time and exhaustively search the parameters for the best match. Besides the high accuracy, JTF representation is a convenient visualization tool for the time-frequency structure of the radar signal. Therefore, the JTF phase estimation technique will be extensively used in this dissertation.

1.3 Motivations

The goal is to improve the performance of ISAR imaging. This research is mainly motivated by the limitations of existing algorithms for ISAR imaging. The fundamental limitations are two motion assumptions used in conventional ISAR imaging [1-3, 8-12]. The first motion assumption is the 2D motion assumption, meaning that the target has a fixed rotational axis during the imaging interval. The 2D motion assumption is evident in the point scatterer models in Section 1.2 (as well as most existing work on ISAR imaging) because only one variable Φ is used to describe the target rotational motion. However, actual targets could have time-varying rotational axis, which is termed 3D motion in this dissertation. In this case, two independent variables, namely azimuth Φ and elevation θ are needed to describe the 3D target motion. The second motion assumption is the rigid body assumption, meaning that all the components of the target moves the same way. This is also evident in the previous point scatterer models because motion parameters R and Φ are independent of the point scatterer number. For a non-rigid body target, different parts of the target could have different motions.

The ISAR imaging of targets with complex motions is the research topic. Clearly, traditional ISAR imaging has difficulties to deal with a target with 3D motion and non-rigid motion as the assumed motion models do not hold. The previous point scatterer models for these complex motions are first extended. Next, the problem of how to make use of the extended models for better target feature extraction is addressed.

1.4 Organization

The dissertation is organized as follows. In Chapter 2, a comparison study of three sets of ISAR images from in-flight aircraft data is made. The three sets of images are generated respectively from blind motion compensated radar images, truth motion compensated radar images using motion parameters recorded by Global Positioning System (GPS) sensors onboard the aircraft, and Xpatch simulated radar images. A comparison of the three sets of images is made to assess the effectiveness of ISAR imaging for the purpose of target identification. In general, good target features can be observed from the resulting ISAR images using the joint time-frequency motion compensation. Two challenging situations where conventional ISAR imaging algorithms have difficulties are also identified. They are due to the non-planar motion and the non-rigid body motion of the target. Chapters 3 to 5 are dedicated to address these problems. In Chapter 3, an algorithm is proposed to detect the presence of 3D motion (i.e., non-planar motion) based on the phase linearity analysis of multiple point scatterers of a target. The effectiveness of the algorithms is demonstrated using measured aircraft and ship data. The problem of 3D image formation with the known 3D target motion is studied in Chapter 4. In Chapter 5, feature extraction from non-rigid body targets is investigated. The adaptive chirplet signal representation is applied to separate the body and the rotating part signals.

More meaningful target feature extraction is possible after the separation. As the joint-time frequency analysis technique is used extensively in this dissertation, study is also sought to improve the JTF phase estimation performance. In Chapter 6, genetic algorithms are proposed for targets with higher order motions to speed up the process of motion parameter search. The research contributions and future work are summarized in the last chapter.

Chapter 2 Comparison of High-Resolution ISAR Imagery from Measured Data and Synthetic Signatures

In this chapter, ISAR images generated from measured data are compared to those from computer simulation in order to evaluate the effectiveness of ISAR-based target identification. Three sets of images are generated including: (i) motion compensated images from measured data using a joint time-frequency technique, (ii) reference images from measured data and GPS-derived aircraft attitude data, and (iii) synthetic images predicted by Xpatch. Visual examination and correlation analysis are undertaken to compare the three sets of images. In addition, two problem areas including jet engine modulation (JEM) line corruption of the measured images and three-dimensional rotation of the target are identified.

2.1 Introduction

High-resolution inverse synthetic aperture radar (ISAR) imaging has been regarded as a possible tool for target identification [1, 12]. There are two important components to an ISAR-based target ID system. The first component is the image formation algorithm in which the raw data collected from an imaging radar are processed and motion compensated to form a focused image of the unknown target. The second component is an image database of known targets populated by either actual measurements or computer simulation. The focused image obtained from measurements is then matched against the image database in order to determine the unknown target type. The success of an ISAR-based target ID system is therefore critically dependent on the quality of these two basic building blocks. In this chapter, ISAR imageries generated from motion compensated measure data and those from computer-simulated synthetic signatures are compared. The objectives are to provide an assessment of the current capabilities and identify possible hurdles in ISAR-based target ID [13].

For this purpose, three sets of images are generated. First, the motion compensated images are generated from radar measurement data of an airplane in flight. Motion compensation is carried out using a joint time-frequency technique that has been reported previously [11]. These images shall be referred as the JTF-mocomp images. Second, a set of reference images is generated by using the aircraft motion data collected during the flight from on-board GPS sensors. Even though these data are available only from cooperative data collection and not in the real target ID scenario, they serve as the ground truth for evaluating the effectiveness of the mocomp algorithm. These images shall be referred as the GPS-reference images. Third, synthetic images are simulated from a CAD model of the aircraft using the electromagnetic signature prediction code Xpatch [14]. These images shall be referred as the Xpatch-synthetic images.

This chapter is organized as follows. Section 2.2 contains the details of methods for generating the JTF-mocomp, the GPS-reference and the Xpatch-synthetic ISAR images. Results are presented showing example images and the correlation between the three sets of images. From the correlation coefficients, two problem areas are identified. In Section 2.3, the jet engine modulation (JEM) line issue in the frontal look region of the target is examined and an algorithm to remove the JEM lines from the measured images is proposed. In Section 2.4, the variable imaging plane problem during certain portions of the flight is examined. Conclusions are given in Section 2.5.

2.2 Measured and Synthetic Image Generation

With the radar I/Q data, the tracking data, the GPS data and the CAD model of the aircraft, measured and simulated 2-D ISAR images can be generated. First, the procedures used to generate the JTF-mocomp, the GPS-reference and the Xpatch-synthetic ISAR images are described. From these results, a comparison to evaluate the effectiveness of the motion compensation algorithm and electromagnetic modeling is carried out.

2.2.1 Motion Compensation Using Joint Time-Frequency Algorithm

In the usual case of ISAR imaging where the complex target motion is not known, motion compensation is needed to form a focused ISAR image. For this purpose, a previously developed adaptive JTF algorithm [11] is used. After the coarse range alignment all the scatterers are assumed to be located in their respective range cells. The radar backscattered signal as a function of dwell time t_D in a particular range cell can be written as

$$E(t_D) = \sum_{k=1}^{N} A_k \exp[-j\frac{4\pi f}{c}(R(t_D) + x_k \cos\theta(t_D) + y_k \sin\theta(t_D))] \tag{2.1}$$

where N_k is the number of point scatterers in that range cell, and A_k, x_k, y_k are respectively the scattering amplitude, down range position and cross range position of the k^{th} point scatterer. $R(t_D)$ is the residual uncompensated translation displacement and $\theta(t_D)$ is the rotational displacement. The JTF technique used here is a search and projection procedure to represent phase behavior of the signal $E(t_D)$. To find the motion parameters, basis functions in the form of

$$h(t) = \exp[-j2\pi(f_0 t + \frac{1}{2} f_1 t^2 + \frac{1}{3} f_2 t^3)] \tag{2.2}$$

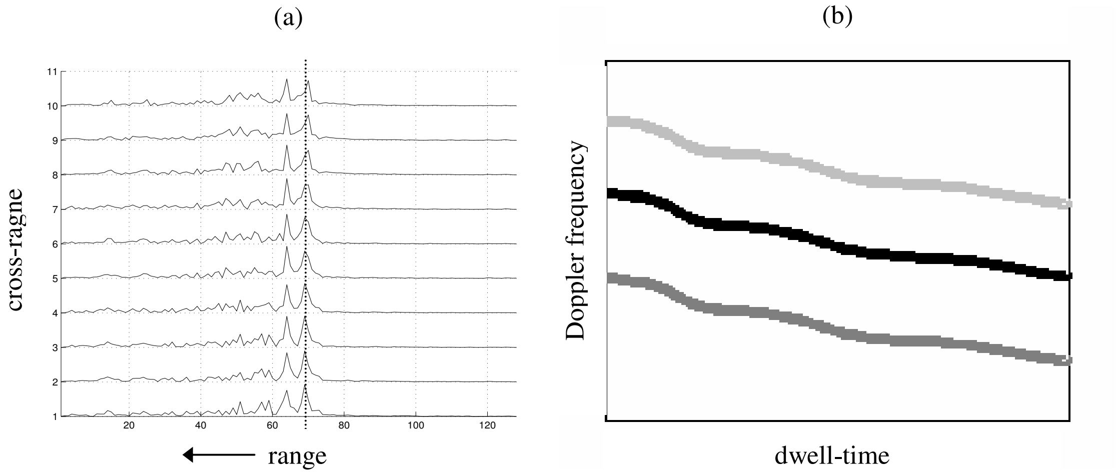

Fig. 2.1 Fine motion compensation is carried out by extracting the Doppler frequency versus dwell time behavior of the strong point scatterer in the signal.

are chosen. The basis function is searched for over the parameter space (f_0, f_1, f_2) to best represent the time-frequency behavior of the signal by maximizing the projection of the signal onto the basis:

$$\max_{f_0, f_1, f_2}\left|\int E(t)h^*(t)dt\right|^2 \tag{2.3}$$

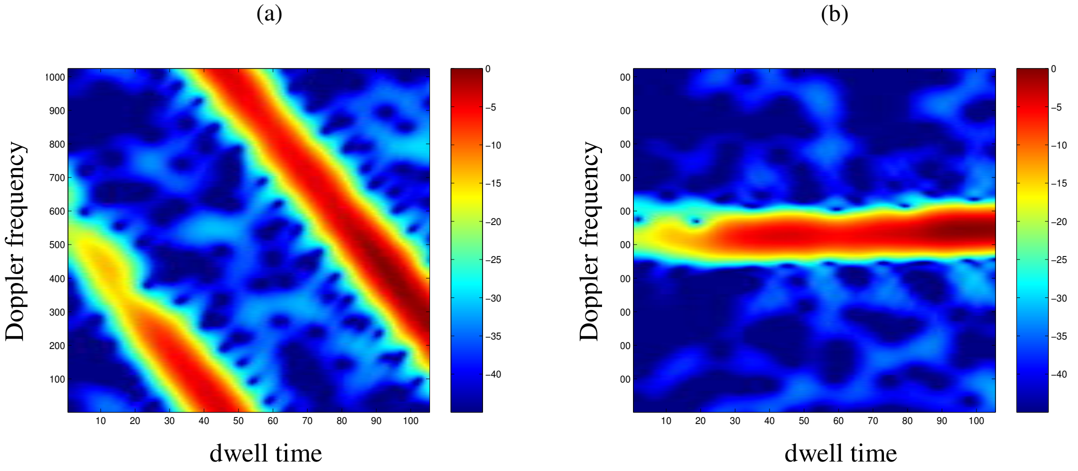

Fig. 2.2 Trajectory of a strong scatterer in the (dwell time)-(Doppler-frequency) plane from measured data. (a) Before JTF motion compensation. (b) After JTF motion compensation.

After the time-varying phase for the strongest point scatterer is found, the original signal is multiplied by the conjugate of this phase factor to compensate for the translation motion. This algorithm can also be extended to multiple range cells to correct for higher order rotation motion. Figures 2.1 and 2.2 show the JTF processing concept**.** After coarse range alignment a particular range bin may contain multiple scatterers with time-varying Doppler frequencies. The (dwell time)-(Doppler frequency) behaviors of these scatterers are illustrated in Figure 2.1b. Figure 2.2a shows the JTF behavior of a dominant scatterer in a range cell from actual measurement data. It is seen from Figure 2.2b that after JTF compensation its trajectory is straightened. After applying JTF motion compensation, the standard FFT processing in the dwell time domain brings the signal into the cross range image domain.

2.2.2 Ground Truth Image Generation Using GPS Data

The motion parameters from on-board GPS sensors collected during the cooperative flight of the airplane are next used to generate the ground truth ISAR images. The resulting reference images can be used to evaluate the quality of the JTF-mocomp images from the last section. Furthermore, motion data can be used to extract azimuth and elevation look angle information for carrying out the electromagnetic simulation of the aircraft.

First, coordinate transformation is carried out since the GPS data are in the fixed Earth system, while the desired azimuth and elevation angles are defined with respect to the local coordinate of the aircraft (see Figure 2.3). The latter information is needed for the simulation process and for determining the absolute scaling of the measured images along the cross range dimension. Unlike JTF motion compensation where the coarse range alignment is carried out based on range profile correlation, here range data from the GPS measurement are used directly for range alignment. In addition, the aspect angle versus dwell time information is used to correct for higher-order rotational motions. The data are reformatted from uniform sampling in dwell time to uniform sampling in aspect angle. The FFT is then used to generate the final ISAR images. Since the look angle information is available, the resulting ISAR images can be scaled in the cross range dimension to absolute physical size.

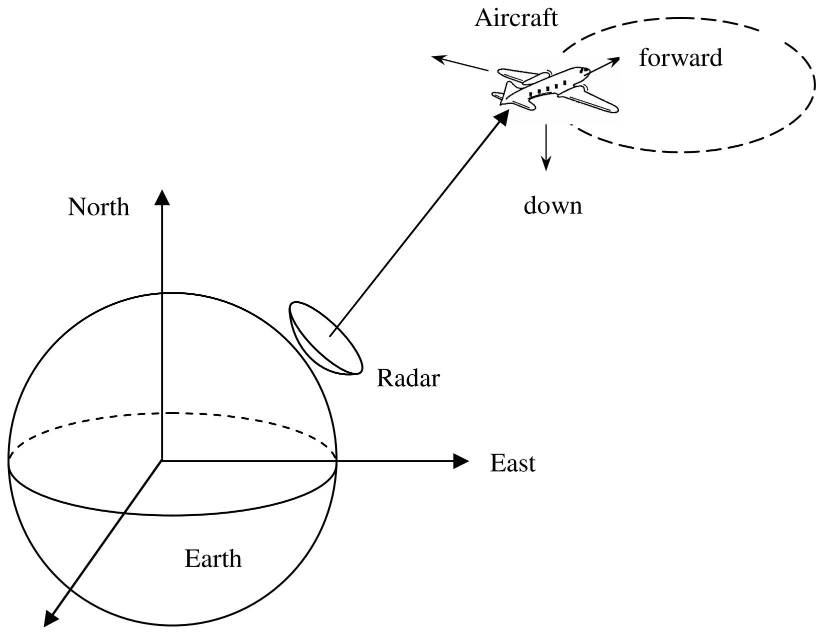

Fig. 2.3 Global and local coordination systems of the problem (figures not drawn to scale).

2.2.3 Synthetic Signature Prediction Using Xpatch

To test the effectiveness of electromagnetic modeling for ISAR imaging, the simulated ISAR images are generated using Xpatch and the radar and aircraft motion parameters from Section 2.2.2. Xpatch is an electromagnetic computation code based on the shooting and bouncing ray method [15]. It can be used to compute the backscattering of complex targets of large electrical sizes. In the Xpatch simulation, rays are shot from the incident look angle and all the multiple reflections are tracked until the rays exit the target (see Figure 2.4). The image is simulated by updating the ISAR image plane one ray at a time using its ray-spread function [16]. The image update is further accelerated by an FFT-based algorithm [17]. Note that this fast image simulation algorithm requires only a single ray trace per image. It is therefore orders of magnitude faster than the conventional method that requires multi-frequency, multi-aspect data. The typical simulation time using this approach is approximately 30 minutes per image on an SGI O2 workstation.

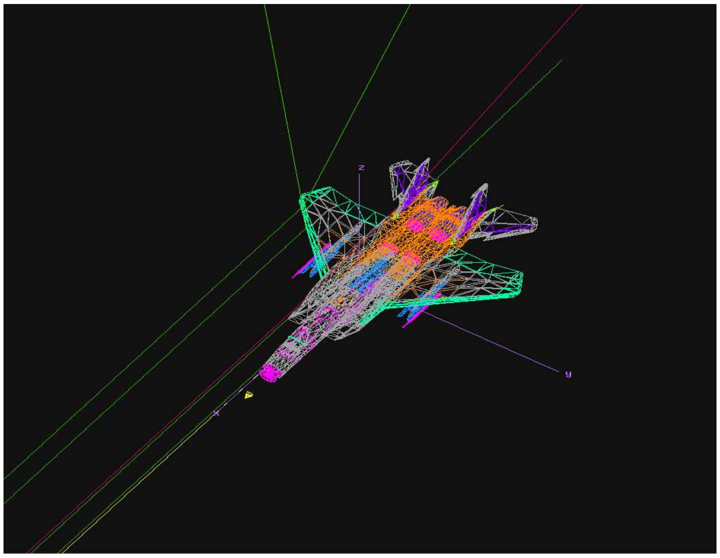

Fig. 2.4 Shooting and bouncing ray technique for radar signature simulation.

While the ISAR images generated from Xpatch contain absolute scaling along the cross range dimension, the ISAR images from the JTF-mocomp process are not calibrated along that dimension since the rotational speed is not known. Here the look angle information derived from the GPS data is used. Prior to making any image comparisons, the Xpatch images are first re-scaled such that they have the same cross range resolution and scaling as the images from the measured data.

2. 3 Image Comparisons

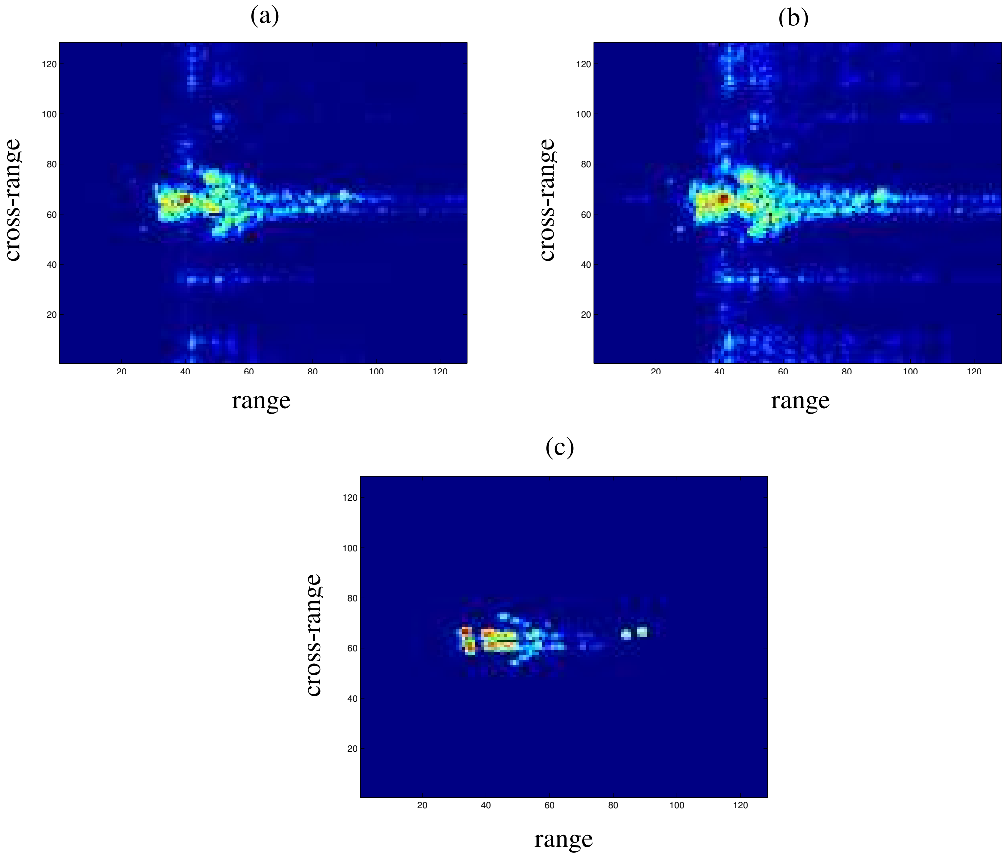

Fig. 2.5 ISAR images from: (a) JTF-mocomp. (b) GPS reference. (c) Xpatch-synthetic.

In this section, image comparisons are made among the three sets of ISAR images: the JTF-mocomp images, the GPS-reference images and the Xpatch-synthetic images. Figure 2.5 shows one set of such comparisons. The look angle is near tail-on of the airplane. The JTF-mocomp image is shown in Figure 2.5a. It is fairly well focused and the features from the tail, the two wings and the fuselage are clearly exposed. The GPS-reference image is shown in Figure 2.5b. It is observed that the agreement between the JTF-mocomp and the GPS-reference images is good. Figure 2.5c shows the corresponding Xpatch-synthetic image. Again the outline of the aircraft is readily observed in this image, although the image is much more focused than the two images from measured data. It is shown that JTF motion compensation works well during most of the fight time. After a side-by-side visual examination, it is found that most mocomp images are in fact slightly better focused than the reference images. It is believed that this is due to the limited accuracy of the GPS sensor data. The synthetic images show good qualitative agreement with the measured images. However, they are in general less diffused than the measured images. This is not surprising since the synthetic image formation assumes no motion errors. Furthermore, the CAD model used does not capture all of the fine details of the actual target.

While the comparison from visual examination shows promising agreement between the three sets of images, an image correlation is undertaken for a more quantitative comparison. Before the correlation, the images are power transformed to account for the different dynamic ranges. Figure 2.6 shows both the correlation coefficient between the JTF and GPS images, and that between the JTF and Xpatch images versus azimuth look angle. From the two curves, it is seen that the JTF-mocomp images agree very well with its GPS-reference counterparts, indicating that blind motion compensation is a very feasible method for processing real-world radar data. The correlation coefficient between the JTF and Xpatch images is in general lower than that between the measured images. In particular, two problem regions can be seen from this plot. First, in the region near nose-on (180 degrees in azimuth), the correlation coefficient is significantly lower. The reason is due to JEM lines in the measured data. This problem is further discussed in Section 2.3 and an algorithm to remove JEM lines is proposed. Second, at some angles around the broadside region (90 degrees in azimuth), the correlation coefficient is also low. The associated JTF images are found to be of low quality. After further investigation, it is found that the image blurring is due to variations in the imaging plane, not the motion compensation processing. This problem is discussed in detail in Section 2.4.

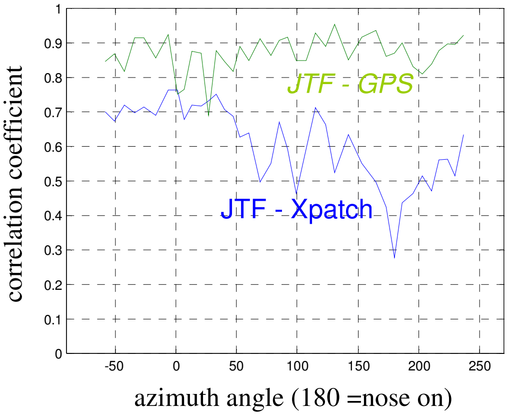

Fig. 2.6 Correlation coefficients between JTF and GPS images, and between JTF and Xpatch images.

2.4 Problematic areas

2.4.1 Non-rigid body motions

Jet engine modulation (JEM) is a phenomenon caused by the high-speed rotational movement of the aircraft engine [18, 19]. For an imaging radar, the typical pulse repetition frequency (PRF) is much slower than the engine rotation frequency. Thus the resulting ISAR image in the frontal region of an aircraft contains an aliased component along the cross range dimension. Such effect is difficult to predict accurately using simulation. Furthermore, JEM lines are noise-like and can corrupt the geometrical features of the target in the ISAR image. For target ID using 2D ISAR imaging, it would be useful to devise an algorithm to remove JEM lines, and therefore enhance the image and the subsequent ID process.

Here, it is assumed that the aircraft consists of a slow moving body with a constant rotational velocity Ω_b and a fast moving engine component with a different rotational velocity Ω_p. Then the received radar return as a function of dwell time can be written as:

$$\begin{aligned} E(t_D) = & \sum_{k=1}^{N_b} A_k \exp[-j\frac{4\pi f}{c}(R(t_D) + x_k \cos(\Omega_b t_D) + y_k \sin(\Omega_b t_D)] \\ & + \sum_{k=N_b+1}^{N} A_k \exp[-j\frac{4\pi f}{c}(R(t_D) + x_k \cos(\Omega_p t_D) + y_k \sin(\Omega_p t_D)] \end{aligned} \quad (2.4)$$

where N is the total number of point scatterers within one range cell, of which N_b are the body scatterers. Usually Ω_p is much greater than Ω_b. While the first term can be meaningfully mapped into the image plane of the target via the Fourier transform, the second term results in serious Doppler smearing across the cross range domain and may overshadow the target features.

The joint time-frequency technique described earlier can also be utilized to separate the fast moving part from the relatively slow moving body [20]. For the component due to target body scattering, the Doppler frequency is

$$f_D^b = \frac{4\pi f}{c}\Omega_b[y\cos(\Omega_b t_D) + x\sin(\Omega_b t_D)] \approx \frac{4\pi f}{c}\Omega_b(y + x\Omega_b t_D) \tag{2.5}$$

while the Doppler frequency due to the fast rotating part is

$$f_D^p = \frac{4\pi f}{c}\Omega_p[y\cos(\Omega_p t_D) + x\sin(\Omega_p t_D)] \tag{2.6}$$

It can be seen that (2.5) is a linear function of dwell time while (2.6) is a sinusoidal function. In the time-frequency plane, the two signals can thus be distinguished. If the signal is further parameterized by basis functions that have linear Doppler frequency behavior as a function of dwell time, the two signals can be separated automatically by their displacement and slope parameters. The adaptive joint time-frequency processing technique is utilized to carry out the parameterization. The basis used is similar to that given in (2.2) with the linear and quadratic phase terms. The project and search procedure given in (2.3) is carried out iteratively. At each iteration, the basis parameters (f_0, f_1) and B_p, which is the maximum projection value of the signal onto the basis, are found. The best basis at stage p is then removed from the signal:

$$E_{p+1}(t) = E_p(t) - B_p h_p(t) \tag{2.7}$$

The searching process is repeated until the energy of the residue signal is smaller than a preset threshold. The signal component due to the target scattering can thus be reconstructed by using all the bases with small displacement f_0 and small slope parameter f_1. Fig. 2.7 shows the correlation between the synthetic images and the measure images after JEM removal. It is observed that the correlation coefficients in the JEM region are increased after the JEM interference is removed from the body.

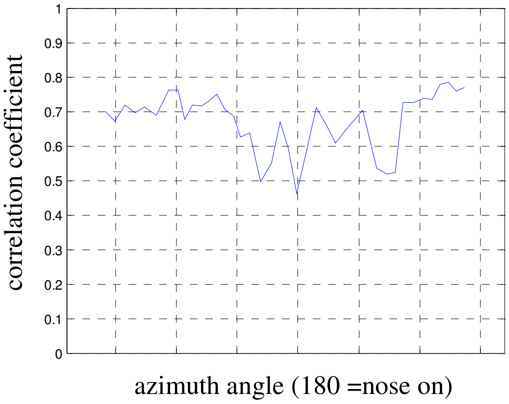

Fig. 2.7 Correlation between JTF and Xpatch images after JEM removal.

2.4.2 Imaging Plane Variation

From the correlation curves, some images generated from the measured data outside of the JEM angular region are also found to be poorly focused. For those frames, it is found that the associated GPS-reference images also fail. If the data quality from the radar did not change abruptly, the cause must not be in the motion compensation algorithm, but rather from extraneous motion during the imaging interval, which cannot be handled by any motion compensation method. Here the possible causes are examined. The movement of the aircraft in space relative to the ground radar consists of radial motion and rotational motion. Because the range alignment process can remove the radial motion, what remains a problem is the 3D rotational motion of the aircraft. Suppose during the imaging interval the rotational motion is described by the look angles (θ,ϕ) on the target. The requirement of a constant rotation axis described by (θ_0, ϕ_0) leads to the following equation that constrains the values of (θ,ϕ):

$$\sin\theta_0 \sin\theta \cos(\phi-\phi_0)+\cos\theta_0 \cos\theta = 0 \tag{2.8}$$

If $\theta_0=0$, eq. (8) requires $\theta=\pi/2$. In this case, the aircraft rotates about its vertical axis and the imaging plane is the top view of the airplane. If $\theta_0=\pi/2$ and $\phi_0=\pi/2$, then $\phi=0$. In this case, the aircraft rotates about its axis along the wing and the imaging plane is the side view of the airplane.

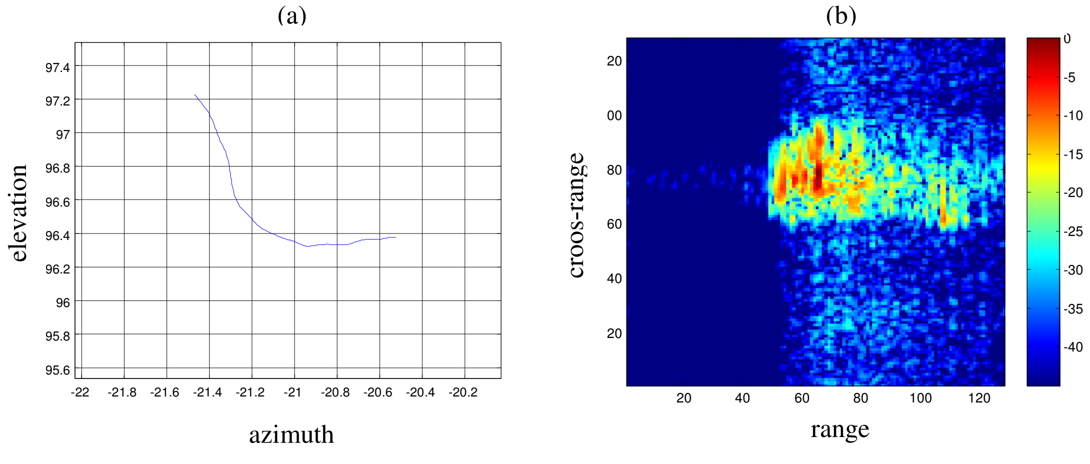

Fig. 2.8 Effect of imaging plane variation on ISAR image.

The images from these two cases will be quite different. If an imaging interval includes both types of motion, the resulting image is expected to be unfocused.

Although this is an extreme example, several cases are observed in the real data where the imaging plane variation in the 128 pulse records leads to bad images. Figure 2.8 shows a particular example of imaging plane variation. From the azimuth-elevation plot in Figure 2.8a derived from the GPS data, two different imaging planes are recognized. During the first half of the 128 records, the aircraft undertakes nearly a vertical rotation, while during the second part it undertakes a horizontal rotation. So a very smeared image is obtained as shown in Figure 2.8b. A better image can be obtained by using only the first part or the second part of the data. The resulting image from the first part of the data is a side view of the aircraft, while the image from the second part of the data is a top view of the aircraft. Unfortunately, the aircraft attitude data on non-cooperative targets are usually not accessible. In such cases, the questions of how to detect imaging plane variation and how to form the best possible images become important research issues. This topic is under current investigation.

2.5 Conclusions

To evaluate the effectiveness of ISAR-based target ID, ISAR images generated from measured data are compared to those from computer simulation. Three sets of images are generated including: (i) motion compensated images from measured data using a joint time-frequency technique, (ii) reference images from measured data and GPS-derived aircraft attitude data, and (iii) synthetic images predicted by Xpatch. Visual examination and correlation analysis are undertaken to compare the three sets of images. Through the comparisons, the following conclusions can be made. First, JTF motion compensation method performed well with real world ISAR data. Second, Xpatch is a feasible tool to generate a synthetic image database for ISAR-based target ID. Two problem areas are also identified. JEM line corruption of the measured images is quite severe in the frontal sector of air targets. A possible algorithm based on joint time-frequency technique is proposed to remove the JEM lines. In addition, the problem of imaging plane variation is identified to be the cause of poor ISAR images during some time of the flight. Further investigation is needed to devise methods to overcome this problem.

Chapter 3 An Algorithm to Detect the Presence of 3D Target Motion from ISAR Data

An algorithm to detect the presence of 3D target motion from ISAR data is presented. Based on the 3D point scatterer model, the effect of 3D motion on ISAR imaging is first examined. It is shown that existing motion compensation algorithms cannot properly focus targets exhibiting 3D motion during the imaging interval. An algorithm is then derived to blindly detect the degree of 3D target motion from raw radar data. It is based on measuring the linearity of phases between two or more point scatterers on the target. The phase estimation is implemented using the adaptive joint time-frequency technique. Examples are provided to demonstrate the effectiveness of the 3D motion detection algorithm with both simulation and real ISAR data. The detection results are corroborated by the truth motion data from on-board motion sensors and correlated with the resulting ISAR images.

3.1 Introduction

Existing motion compensation algorithms usually assume that the rotational motion of a target is confined to a 2D plane during the dwell duration [1-3, 8-12, 21]. the term *2D motion* shall be used to refer to target rotational motion of this type. Under the 2D motion assumption, rotational compensation of a second point on the target will focus the whole target. When there is *3D motion*, i.e., when the rotational motion is not confined to a 2D plane, rotational compensation of a second point cannot focus the whole target.

Recently, several independent research groups have reported that, for aircraft undergoing fast maneuvers or ships on rough seas, the motion of a target may be highly chaotic and does not always obey the 2D motion model [22-24]. As a result, the image formed using the standard motion compensation algorithms is blurred. In [22] and [23], the effect of 3D motion on ISAR imaging is discussed. However, target motions are assumed to be known from other auxiliary sensor data that are usually not accessible in real operational environment. In [24], the imaging interval is adaptively chosen based on the resolved target feature in the radar image to overcome the 3D motion issue. It requires sound knowledge of the target under consideration, which is often not known to the end users of ISAR data.

The objective of this chapter is to develop an algorithm to detect the presence of 3D motion during the imaging interval from ISAR data. Based on the 3D point scatterer model, the effect of 3D motion on existing imaging algorithms is first examined. an algorithm to blindly detect the existence of 3D motion is then developed. For this purpose, only the estimation of phases of several prominent point scatterers is needed. It can be accomplished by the joint time-frequency analysis [11]. With the detection algorithm, it is possible to distinguish the time intervals when the target undergoes smooth 2D motion from those containing more chaotic 3D motion. As a result, the good imaging intervals where focused images are more easily formed can be automatically determined.

The chapter is organized as follows. First, the ISAR imaging problem is formulated in terms of a point scatterer model in Section 3.2. In Section 3.3, the 2D motion assumption in existing motion compensation algorithms is analyzed. The reason why 3D motion is a problem for ISAR imaging is shown. Section 3.4 discusses the 3D motion detection algorithm in detail. Examples from both simulation and measurement data are presented in Section 3.5. The conclusions are given in the last section.

3.2 2D and 3D Motion Models

The standard model used in ISAR processing is the point scatterer model given as

$$E(f,t_D)=\sum_{i=1}^{Ns}\sigma_i(x_i,y_i)\exp\{-j\frac{4\pi f}{c}[r(t_D)+x_i+y_i\varphi(t_D)]\} \tag{3.1}$$

where f is the radar frequency and t_D is the dwell time. The radar echo data $E(f,t_D)$ is in the (frequency)-(dwell time) domain. x and y represent the target range and cross-range positions, respectively. The target consists of N_s point scatterers, with the i^{th} point scatterer depicted by position (x_i,y_i) and strength $\sigma(x_i,y_i)$. The target motion includes both the translational motion described by $r(t_D)$ and the rotational motion described by $\varphi(t_D)$. When there is no translational motion and the rotational motion is uniform, it is seen that a 2D Fourier transform brings the radar data $E(f,t_D)$ into a radar image $\sigma(x,y)$. Otherwise, motion compensation is a critical step in ISAR imaging.

The above model is a 2D problem since the target rotational motion is confined to a 2D plane and described in terms of only one angular parameter φ. When there is 3D motion of the target, a more general 3D model is required:

$$E(f,t_D) = \sum_{i=1}^{Ns} \sigma_i(x_i, y_i, z_i) \exp\{-j\frac{4\pi f}{c}[r(t_D) + x_i + y_i\varphi(t_D) + z_i\theta(t_D)]\} \tag{3.2}$$

In the above expression, a third coordinate z of the target is included to represent the 3D target and another independent angular motion parameter θ is introduced to describe the 3D rotational motion (see Fig. 3.1). It is possible to perform 3D target imaging if the target motion is known exactly [25, 26]. In practical ISAR scenarios, however, the target motion is not accessible. The objectives here are to examine the effect of 3D motion on ISAR imaging and devise an algorithm to detect the presence of 3D motion from the radar data itself, i.e., without any additional knowledge of the target motion.

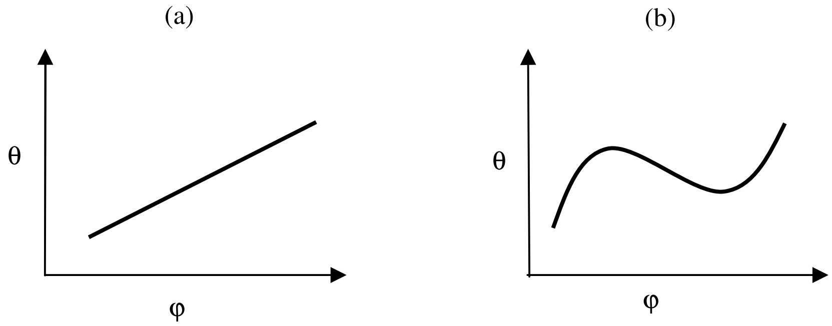

Fig. 3.1 Illustration of 2D motion vs. 3D motion.

3.3 Problem of Existing Motion Compensation Algorithms with 3D Target Motion

First, it is shown that the more general 3D model degenerates into the 2D model under two conditions. The first case is when there is a linear relationship between φ and θ, i.e.,

$$\theta(t_D) = b\varphi(t_D) \tag{3.3}$$

This would cast equation (3.2) into the form

$$E(f,t_D) = \sum_{i=1}^{Ns} \sigma_i(x_i, y_i, z_i)\exp\{-j\frac{4\pi f}{c}[r(t_D) + x_i + (y_i + bz_i)\varphi(t_D)]\} \tag{3.4}$$

Comparing (3.4) with (3.1), it is seen that if $y_i' = y_i + bz_i$ is defined, then the rotational motion is in fact a two-dimensional one and the resulting 2D image $\sigma(x_i, y_i')$ is the projection from the 3D target $\sigma(x_i, y_i, z_i)$ onto the 2D motion plane.

The second case is when the z dimension of the target is so small that the third phase term in (3.2) can be neglected. For example, suppose a radar operates at a frequency of 10 GHz and the θ variation is limited to 0.5 degree. If the target thickness in the z-dimension is less than 0.2 m, then the third phase term is less than $\pi/4$ and the 2D model is adequate.

From the above consideration, it is seen that the 2D model is applicable if either the rotational motion is 2D or the target is of 2D in extent. When there exists 3D motion on a full 3D target, any motion compensation algorithms based on the 2D model are not expected to focus the target well. this issue will now be examined in more detail. Since the translational motion compensation is independent of the models in (3.1) and (3.2), only the rotational motion compensation needs to be investigated. With 2D rotational motion present, the phase of a point scatterer *i* due to the rotational motion is

$$P_i(t_D) = y_i \varphi(t_D) \tag{3.5}$$

Here, the constant $4\pi f/c$ has been suppressed for simplicity. As it is seen from (3.5), the phases of all the point scatterers are linearly related (through the ratio of their cross range positions). If one of the phases is made a linear function of time, then all the phases are linearized simultaneously, and the whole target can be focused after the Fourier transform. This is the basis of most 2D rotational motion compensation algorithms based on the point scatterer model [3, 7, 11, 21]. This concept is illustrated in Figure 3.2. Figure 3.2a shows the phase functions of two point scatterers under 2D rotational motion. Figure 3.2b shows that both points can be made linear functions of time after one of them is forced to be a linear function.

With 3D motion, the phase of a point scatterer due to the rotational motion is

$$P_i(t_D) = y_i \varphi(t_D) + z_i \theta(t_D) \tag{3.6}$$

In this case, the phases of the point scatterers are no longer linearly related. If one of the phases is made a linear function of time, the phases of the other point scatterers are not automatically made linear functions of time, as was the case of 2D motion. Figure 3.2c shows the phase functions of two point scatterers with 3D motion. As it seen from Figure 3.2d, after one point is forced to be of linear phase, the phase of the other point remains nonlinear.

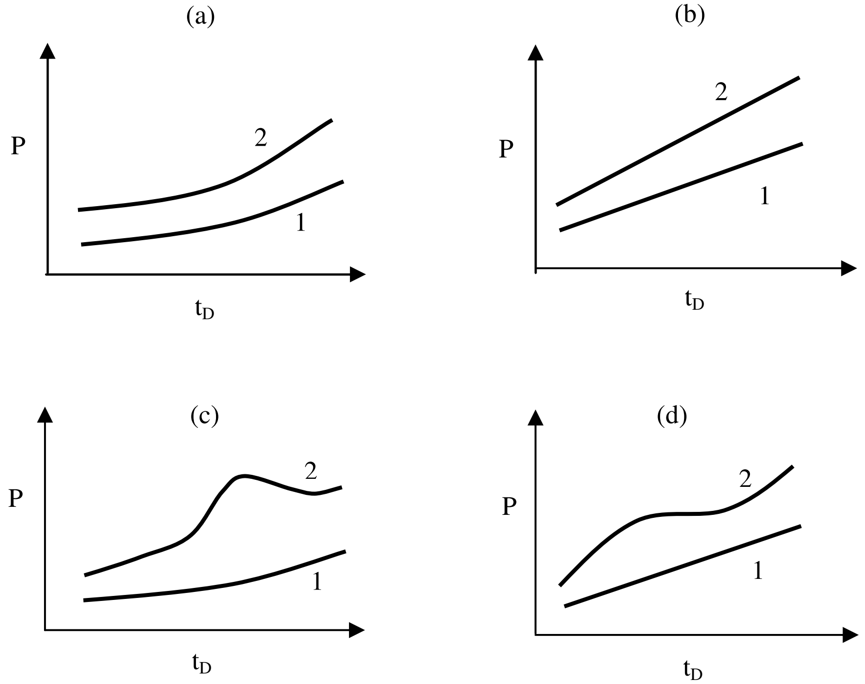

Fig. 3.2 Phase linearization achieved by rotational motion compensation (a) Phases of two point scatterer with 2D rotational motion. (b) Both phases are linearized with rotational motion compensation. (c) Phases of two point scatterers with 3D motion. (d) Only one phase is linearized with rotational motion compensation.

Figure 3.3 illustrates the effects of the rotational motion compensation on the final images under 2D and 3D target motion. The adaptive joint time-frequency (AJTF) algorithm reported in [11] is used for motion compensation. Ten points in 3D space are used to simulate the radar data. Figure 3.3a shows an assumed 2D rotational motion. Figure 3.3b shows the image after the translational motion compensation. The image shows one point being focused in range cell 25 while other points are unfocused due to the rotational motion. Figure 3.3c shows the image after the 2D rotational motion compensation in which a point scatterer in range cell 57 is selected for focusing. All the point scatterers are focused in the image. The situation with an assumed 3D target motion is shown in Figures 3.3d-3.3f. Figure 3.3d shows the assumed 3D motion. Figure 3.3e shows the image after translational motion compensation. Figure 3.3f shows the final image after the 2D rotational motion compensation. The two points in range cells 25 and 57 are focused, as expected. Another point scatterer in range cell 99 is also focused as it happens to be in the same 2D motion plane as the point scatterer in range cell 57. As it can be seen, it is not possible to focus all the points simultaneously with an existing algorithm based on the 2D motion model.

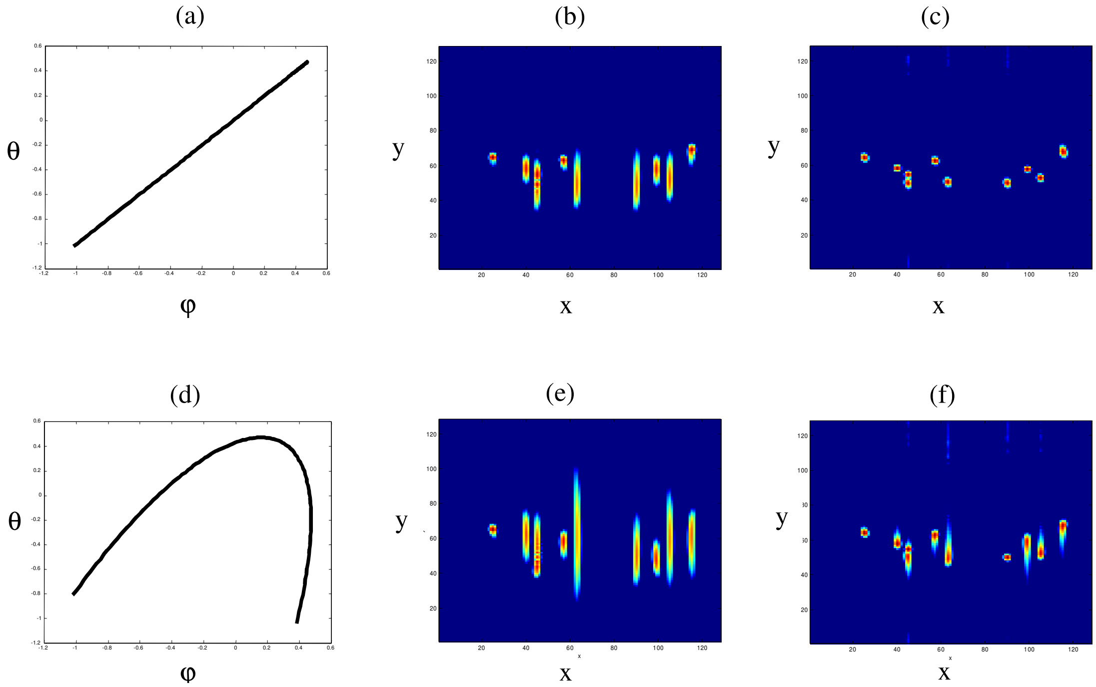

Fig. 3.3 Problem with a typical motion compensation algorithm (a) Target undergoes a 2D motion. (b) Image after translational motion compensation. (c) Image after rotational motion compensation. (d) Target undergoes a 3D motion. (e) Image after translational motion compensation. (f) Image after rotational compensation.

3.4 3D Motion Detection Algorithm

Since existing motion compensation algorithms cannot handle 3D target motion, it is desirable to develop a general compensation algorithm that can accommodate 3D motion. However, this is a difficult task (see [27] for background on this problem) and outside the scope of this work. The goal here is to develop an algorithm to detect the presence of 3D motion from radar data. If those time intervals where 2D target motions are predominant can be reliably detected, the existing 2D motion compensation algorithms can be used to form well-focused ISAR images.

As discussed in the last section, 2D motion can be represented by a linear relationship between θ and φ. Therefore, the objective is to detect the existence of a nonlinear relationship between θ and φ in the 3D motion detection algorithm. First, write the relationship between θ and φ into a linear and a nonlinear part as follows:

$$\theta(t_D) = b\varphi(t_D) + m(t_D) \qquad (3.7)$$

where b is the linear constant and $m(t_D)$ is the nonlinear part which indicates deviation from 2D target motion, or the degree of 3D motion. Next try to gather target motion information by analyzing the phases of two point scatterers on the target. The relationship between the phase functions P_1 and P_2 of two point scatterers can be written as:

$$P_2(t_D) = aP_1(t_D) + n(t_D) \qquad (3.8)$$

The relationship is again decomposed into a linear part, where *a* is the linear constant, and a nonlinear part $n(t_D)$. The goal is to derive a relationship between $m(t_D)$ and $n(t_D)$ so that the presence of *m* can be detected by observing *n*.

After the standard translational motion compensation, the time-varying phase of a point scatter is in the form of

$$P_i(t_D) = \Delta y_i \varphi(t_D) + \Delta z_i \theta(t_D) \tag{3.9}$$

where Δy_i and Δz_i are differential positions of point scatterer *i* relative to the reference point chosen during translational motion compensation. Substituting (3.7) into (3.9) and then evaluating (3.9) at point scatterers 1 and 2 leads to

$$P_1(t_D) = (\Delta y_1 + b\Delta z_1)\varphi(t_D) + \Delta z_1 m(t_D) \tag{3.10a}$$

$$P_2(t_D) = (\Delta y_2 + b\Delta z_2)\varphi(t_D) + \Delta z_2 m(t_D) \tag{3.10b}$$

Next substitute (3.10) into (3.8), which leads to

$$a[(\Delta y_1 + b\Delta z_1)\varphi(t_D) + \Delta z_1 m(t_D)] + n(t_D) = (\Delta y_2 + b\Delta z_2)\varphi(t_D) + \Delta z_2 m(t_D) \tag{3.11}$$

Notice that if there is only 2D motion, then the phases of the two point scatterers must be linear. This means if $m=0$, then $n=0$. By using this fact and equating the coefficients of $\varphi(t_D)$ in (3.11), the constant *a* can be derived:

$$a = \frac{\Delta y_2 + b\Delta z_2}{\Delta y_1 + b\Delta z_1} \tag{3.12}$$

Substituting (3.12) into (3.11), finally leads to

$$m(t_D) = \frac{\Delta y_1 + b\Delta z_1}{\Delta z_2 \Delta y_1 - \Delta y_2 \Delta z_1} n(t_D) \tag{3.13}$$

Equation (3.13) states that once the nonlinear phase term *n* is known, it is proportional to nonlinear motion *m*. Therefore, the steps to determine the degree of 3D target motion are as follows. First, extract the phases of two point scatterers from the radar data. Next, find the nonlinear phase function *n* using a minimum least squares fit of equation (3.8). Once *n* is known, use equation (3.13) to decide on the degree of 3D motion. The remaining issues are: (i) to determine the phase functions of the point scatterers, (ii) to define the degree of nonlinearity and the degree of 3D motion once *n* is known, and (iii) to compare the degree of 3D motion from one imaging interval to another. These three issues are discussed in the following subsections.

3.4.1 Phase Estimation Using Adaptive Joint Time-Frequency Projection

After the translational motion compensation, the radar signal contains only rotational motion. To estimate the phase of a prominent point scatterer, the adaptive joint time-frequency (AJTF) projection technique discussed in [11] is utilized. The radar data in the (range)-(dwell time) domain are used. Within a fixed range cell, the data can be written as

$$E_s(t_D) = \sum_{i=1}^{Nr} \sigma_i \exp(-j\frac{4\pi f_c}{c}(y_i\varphi(t_D) + z_i\theta(t_D)) \tag{3.14}$$

where f_c is the center frequency. Among the N_r point scatterers within the range cell, the phase behavior of the strongest one is expressed as a polynomial function:

$$\phi_M(t_D) = (f_1 t + f_2 t^2 + f_3 t^3 + ..) \tag{3.15a}$$

and consider

$$h(t) = \exp[-j\varphi_M(t_D)] \tag{3.15b}$$

as a basis for the radar signal. The phase parameters are then found by searching for the maximum projection from the radar signal onto the basis function:

$$< f_1, f_2, f_3, ... >= \arg\max | \int E(t_D) h^*(t_D) dt_D | \tag{3.16}$$

Equation (3.16) means that the phase function parameters are estimated to give a maximum projection from the radar data onto the basis function for that prominent point scatterer. In the search procedure, the first term f_1 can be obtained by using the fast Fourier transform, while all other higher order terms f_2, f_3, … are obtained using exhaustive search. Figure 3.4 illustrates the process of AJTF phase estimation. Figure 3.4 shows the radar signal in one range cell with three point scatterers in the joint (dwell time)-(Doppler frequency) plane. The tilted curve associated with the prominent point scatterer 1 implies there exist higher-order terms in the phase function. Figure 3.4b shows the basis function $h(t_D)$. During the search, the position (f_1), tilting (f_2) and curvature (f_3, …) of h are changed until the projection of h onto the radar signal is maximized.

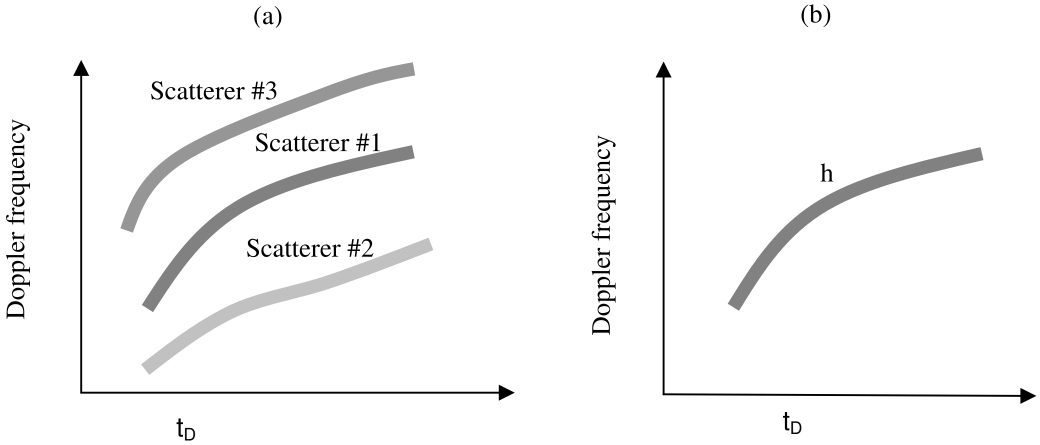

Fig. 3.4 (a) (Dwell time)-(Doppler frequency representation of radar signal in a range cell with three point scatterers. (b) The basis function that is best matched to the dominant point scatterer is found by the AJTF project method.

3.4.2 Measure of Nonlinearity between Two Phase Functions

It is noticed that in (3.8), the two phase functions are represented with a linear relationship plus a nonlinear residual part. After the two phase functions are estimated using the AJTF technique, linear regression can be performed to generate the best-fit linear part. The actual phase deviates from this linear relationship. The deviation, n, is integrated over the dwell time to represent the degree of phase nonlinearity over the imaging interval as follows:

$$N_{12} = \int | n_{12}(t_D) | \, dt_D \qquad (3.17)$$

The process is illustrated in Figure 3.5. The solid line is the actual relationship between the two phase functions P_1 and P_2. The dotted line is the linear approximation of the relationship. The area of the shadowed region is N_{12}.

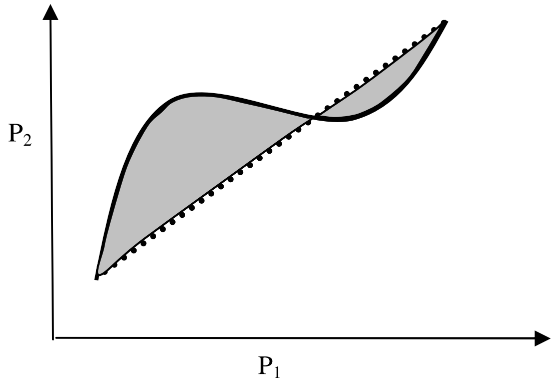

Fig. 3.5 Measure of the nonlinearity of two phase functions.

In a similar fashion, the degree of 3D motion is defined as the deviation from a linear relationship between θ and φ over the dwell interval as follows:

$$M = \int | m(t_D) | dt_D \tag{3.18}$$

Based on (3.13), it is seen that M and N_{12} are directly related:

$$N_{12} = \beta_{12} M \tag{3.19a}$$

where

$$\beta_{12} = \left| \frac{\Delta z_1 \Delta y_2 - \Delta y_1 \Delta z_2}{\Delta y_1 + b \Delta z_1} \right| \tag{3.19b}$$

Thus by finding the observable N_{12}, the degree of 3D motion M to within a proportionality constant can be obtained.

3.4.3 3D Motion Comparison among Different Imaging Intervals

As indicated by (3.19), the phase nonlinearity of two point scatterers N is proportional to the degree of 3D motion M, so the detected phase nonlinearity can be used as a measure of 3D motion. However, it is noticed that the constant of proportionality is dependent on the point scatterer positions. A problem arises when there is a need to compare the detection result from one imaging interval to that from another imaging interval. Since it cannot be guaranteed that the same set of points from frame to frame are tracked, the proportionality constant can change from frame to frame, and M from N across frames cannot be reliably observed. To overcome this difficulty, more than two point scatterers are tracked within each frame and compute N_{ij} for each pairing of scatterers i and j ($i \neq j$). Then an average value $<N_{ij}>$ is generated from all the possible phase relationships. From (3.19),

$$< N_{ij} >=< \beta_{ij} > M \tag{3.20}$$

It is postulated that, from a statistical point of view, $<\beta_{ij}>$ approaches a constant that is independent of frames if a sufficient number of point scatterers is averaged over. If this is true, $<N_{ij}>$ should become a good indicator of M.

The effectiveness of this approach is tested on the detection result by simulation. A set of motion parameters is input and the phase functions based on the 3D motion model are generated. 20 point scatterers from an airplane model are used. A number of point scatterers are then randomly chosen and their phase functions are used to compute $<N_{ij}>$. How the results vary as a different number of point scatterers are used is examined. It is found that the results begin to converge after about 5 scatterers. Fig. 3.6 shows a plot of $<N_{ij}>$ versus the frame number if 5 point scatterers (10 phase pairs) are used. If the number of point scatterers is increased to 10 (45 phase pairs), there is only minor change in the detection output. Therefore, $<N_{ij}>$ can be used to indicate the degree of 3D motion given a sufficient number of point scatterers.

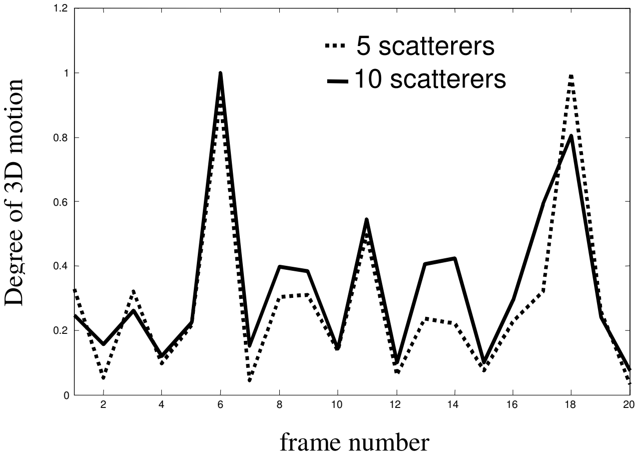

Fig. 3.6 Effect of the number of point scatterers used on 3D motion detection result.

3.5 Results

To demonstrate the effectiveness of the 3D motion detection algorithm, the algorithm is tested on radar data from two targets. The first target is an aircraft, which flew in a large clockwise circle during a 9-minute interval. The target motion data through the GPS (global positioning system) and INS (inertial navigation system) sensors carried on-board the aircraft [28-30] are also available. Figure 3.7 shows the processing flow chart. The GPS/INS data is used to establish the truth target motion. The raw radar data is used as input to the 3D motion detection algorithm. The ISAR images using AJTF motion compensation algorithm can also be generated. It is therefore possible to both compare the detection result with the truth motion, and observe the effect of the 3D motion on the ISAR image quality.

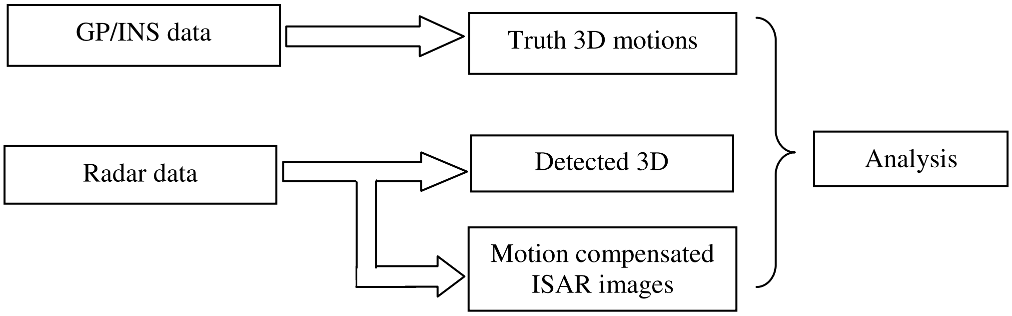

Fig. 3.7 Data processing flow chart.

The 3D motion detection algorithm is first tested on simulated radar data. To generate the simulation data, the actual motion data from the GPS/INS sensors are used in conjunction with a point scatterer model. From the aircraft model, 60 point scatterers are selected to simulate the radar data based on the actual motion data and equation (3.2). Five range cells are then chosen for phase analysis in the detection procedure. Figure 3.8a shows the detected degree of 3D motion for 20 image frames from the simulated radar data. For comparison, Figure 3.8b shows the degree of 3D motion obtained based on the truth motion data. The frames with significant 3D motion are highlighted with circles and the frames with 2D motion are highlighted with diamonds. It is seen that the two results agree fairly well.

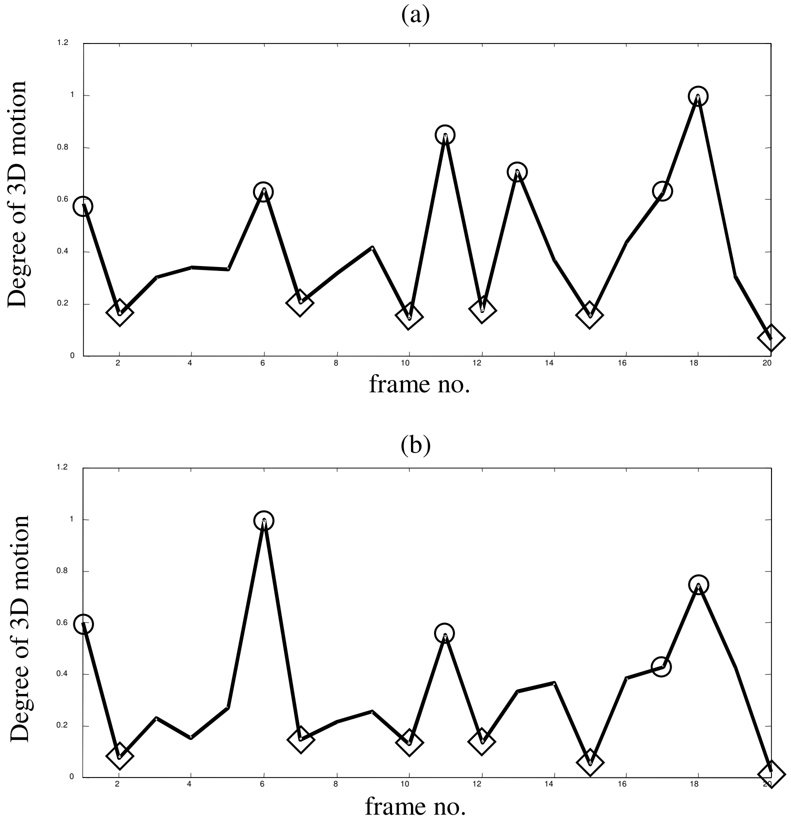

Fig. 3.8 (a) Detected 3D motion from simulated radar data. (b) Degree of 3D motion from truth motion data.

Next, the detection algorithm is tested using the actual radar measurement data. Figure 3.9a shows the detected 3D motion from the radar data over 20 frames. The corresponding imaging interval for each frame is 2.3 seconds while the total flight duration is 5 minutes. The four frames with the most significant 3D motion based on the detection algorithm are labeled as circles. They are frames 6, 14, 17 and 18. Figure 3.9b shows the degree of 3D motion obtained based on the truth motion data. It is observed that the truth motion data indeed contains a high degree of 3D motion at those four frames detected by the algorithm.

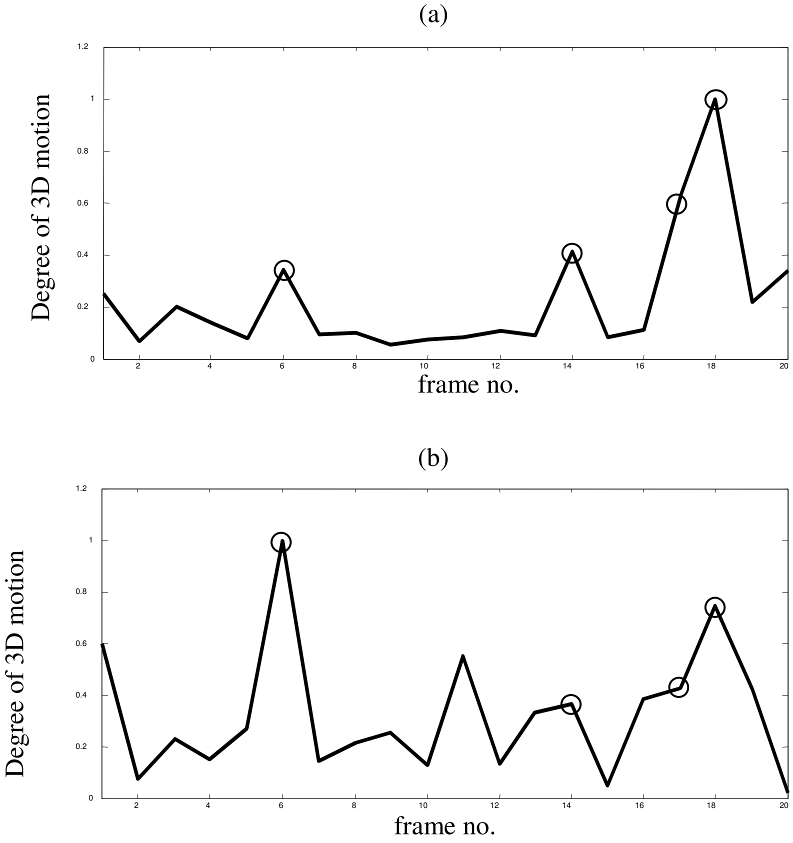

Fig. 3.9 (a) Detected 3D motion from aircraft radar data.
(b) Degree of 3D motion from truth motion data.

To further examine the quality of the ISAR images when 3D motion is present, images are generated using the motion compensation algorithm in Figures 3.10 to 3.13. Figure 3.10a shows the plot of θ vs. ϕ derived from the truth motion data for frame 18, which is a frame found to contain substantial 3D motion. The actual motion is shown in the solid curve and the dashed line is the best-fit 2D motion approximation. It is clear that the solid curve deviates significantly from the dashed line and the actual motion cannot be well approximated with 2D motion. Figure 3.10b shows the resulting image obtained after the motion compensation, and is blurred in the Doppler dimension (vertical axis). As expected, the 2D motion compensation algorithm cannot focus all the points due to the 3D target motion. Figures 3.11a and 3.12b show the same conclusion for frame 14, which is another frame identified as having significant 3D motion. In Figure 3.12, the results are shown for frame 2, which has very little 3D motion. As it can be seen from Figure 3.12a, the actual motion can be well approximated by a line in the θ-ϕ plot. The image shown Figure 3.12b is well focused. In particular, the point scatterers on the target show nearly equal range and Doppler extent, contrary to the previous two images. The aircraft bodyline is clearly recognizable.

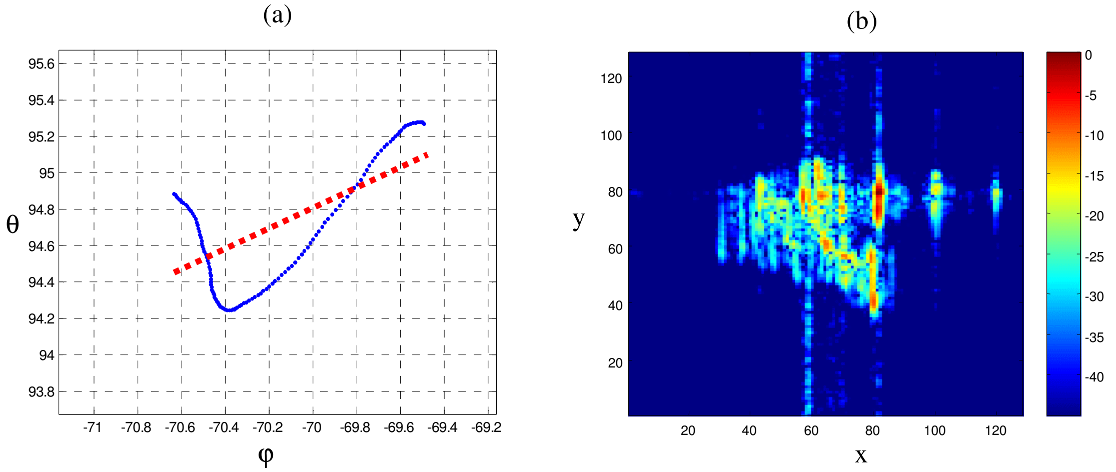

Fig. 3.10 3D motion and resulting ISAR image (frame 18).

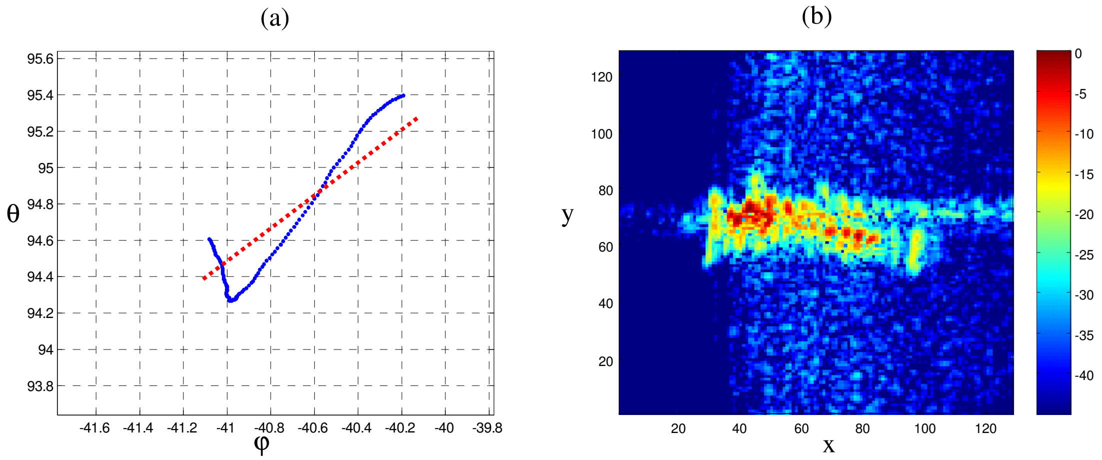

Fig. 3.11 3D motion and resulting ISAR image (frame 14).

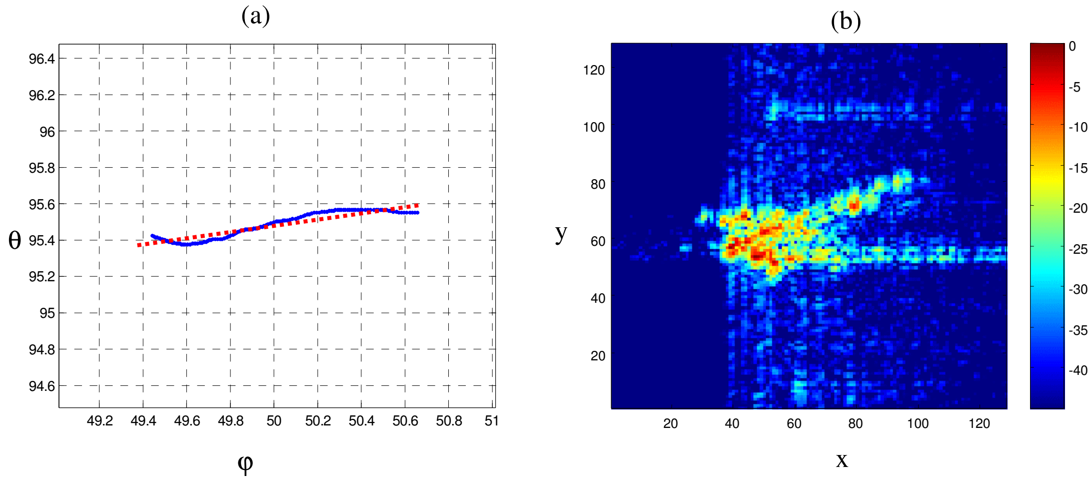

Fig. 3.12 2D motion and resulting ISAR image (frame 2).

From Figure 3.9, it is noticed that there exists a discrepancy in frame 11, where the detection result does not indicate any 3D motion while the truth motion data shows a significant amount of 3D motion. The truth motion is shown in Figure 3.13a, confirming the presence of 3D motion. One explanation is that those prominent points used by the detection algorithm lie nearly on a 2D plane so that they still can be focused. As discussed in Section 3.3, the 2D model is applicable if either the motion is 2D or the target is of 2D in extent. It is likely that the latter condition is met for this frame. This is confirmed by the image shown in Figure 3.13b. It is seen that the image quality is actually decent. Therefore, the detection algorithm objectively reflects the quality of the images generated by 2D motion compensation.

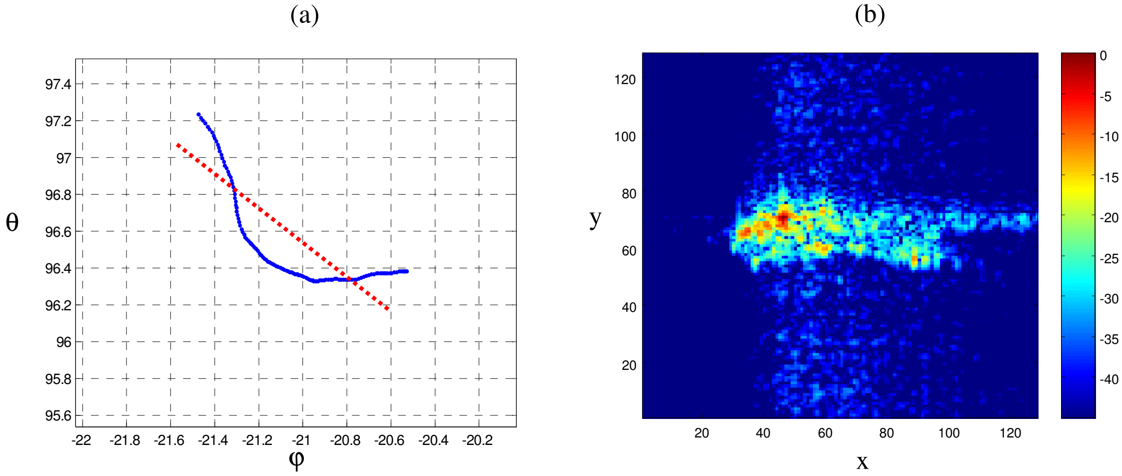

Fig. 3.13 Frame no.11 showing focused ISAR image with 3D motion.

A second data set is used to test the 3D motion detection algorithm. This data set consists of the ISAR data collected from a small ship on the ocean. Because of the surface movement of the sea, the target is believed to have considerable 3D motion during the imaging intervals. The 3D motion detection result is shown in Figure 3.14a with the peaks corresponding to regions with 3D motion. The total data duration is 20 seconds and the imaging dwell time is 0.64 second per frame. For this data set, reliable truth target motion is not available. Instead, the motion compensated images shown in Figures 3.14b to 3.14d are generated to demonstrate the effect of 3D motion on ISAR image quality. The image frame with the largest detected 3D motion, Frame 3, is shown in Figure 3.14b. It is poorly focused. Figure 3.14c shows the image from frame 14, which is the frame with the second highest detected 3D motion. The frame with the smallest 3D motion based on the algorithm, frame 20, is shown in Figure 3.14d. It shows a well-focused ISAR image. This test confirms the effectiveness of the algorithm in detecting good imaging intervals from those imaging intervals containing large 3D motion.

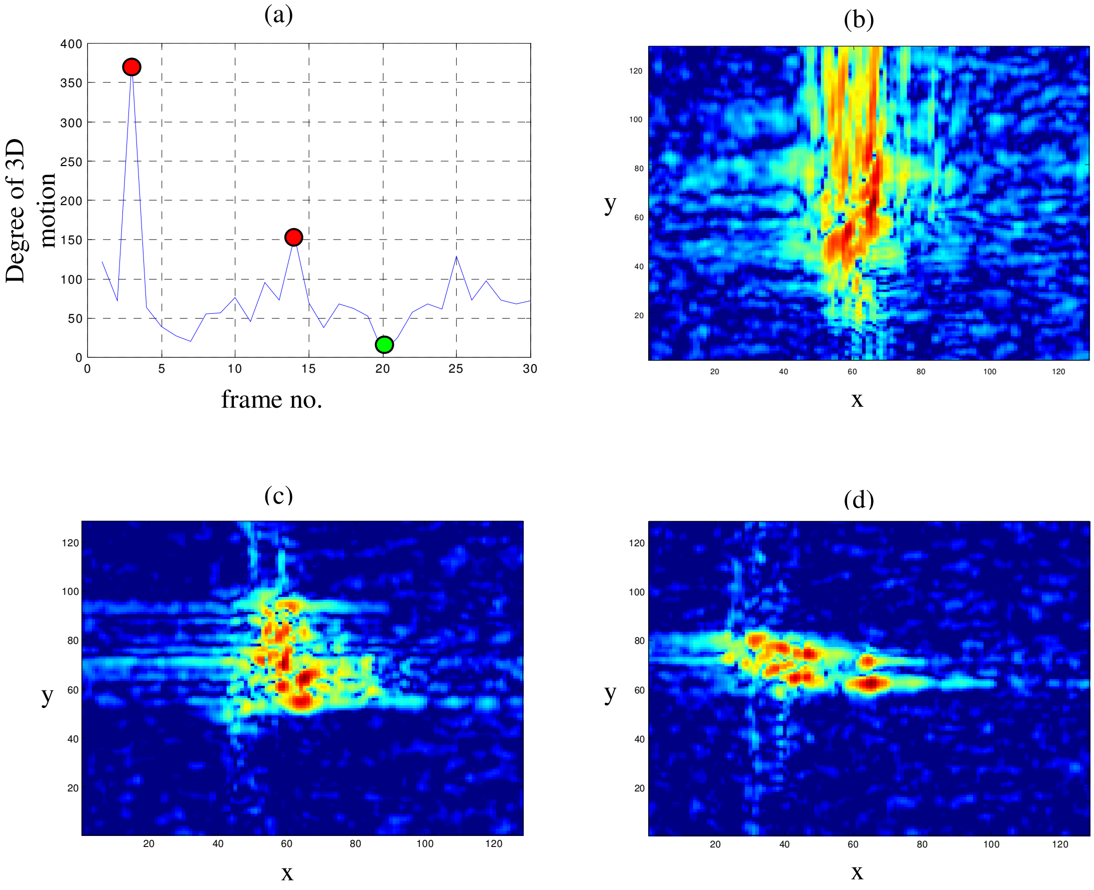

Fig. 3.14 3D motion detection result from radar data of a ship (a) Detected 3D motion. (b) ISAR image from frame 3. (c) ISAR image from frame 14. (d) ISAR image from frame 20.

3.6 Conclusions

In this chapter, the objective is to develop an algorithm to detect the presence of 3D target motion from ISAR data. Based on the 3D point scatterer model, the effect of 3D motion on ISAR imaging is first examined. It was shown that the existing motion compensation algorithms could not properly focus targets exhibiting 3D motion during the imaging interval. An algorithm is then derived to blindly detect the degree of 3D target motion from raw radar data. It is based on measuring the linearity of phases between two or more point scatterers on the target. The phase estimation was implemented using the adaptive joint time-frequency technique. Examples were provided to demonstrate the effectiveness of the 3D motion detection algorithm with both simulation and real ISAR data. The detection results were corroborated with the truth motion data from on-board motion sensors and correlated with the resulting ISAR images. With the detection algorithm, it is possible to distinguish the time intervals when the target undergoes smooth 2D motion from those containing more chaotic 3D motion. As a result, the good imaging intervals where focused images are more easily formed can be automatically selected.

Chapter 4 3D ISAR Image Reconstruction of a Target with Motion Data Using Adaptive Feature Extraction

In this chapter, three-dimensional (3D) inverse synthetic aperture radar (ISAR) image reconstruction with known motion data is studied. In traditional two-dimensional (2D) ISAR imaging, a 2D point scatterer model is adequate to consider the target rotation motion with a fixed rotational axis. However, target motions with a varying rotational axis are sometimes encountered in real situations. Under such cases, the use of a 3D point scatterer model is necessary for 3D ISAR image reconstruction. An adaptive feature extraction algorithm is proposed to reconstruct the 3D image of a target with non-uniformly undersampled radar data over the azimuth and elevation aperture. Simulation results based on actual motion data of air targets demonstrate the effectiveness of the algorithm.

4.1 Introduction

In traditional ISAR imaging, the target is assumed to rotate with a fixed rotational axis during the image formation interval. This motion is termed two-dimensional (2D) motion, since the target motion is confined to a 2D plane. Under this case, only 2D ISAR images can be obtained.

When the target has a varying rotational axis during the imaging interval, the target motion is termed three-dimensional (3D) motion. This can occur on a maneuvering target. Three examples of 3D target motion are shown in Figure 4.1. Figure 4.1a shows a slight deviation from a 2D motion. This can occur when an aircraft undergoes a well-controlled maneuver during the imaging interval [22]. Figure 4.1b shows a severe wave-like 3D motion. This kind of motion is typical of ship targets due to ocean wave modulation [24]. Figure 4.1c shows the target motion data from multiple flight paths. Although each flight path obeys 2D motion, the cumulative data over the angular aperture appear to be 3D.

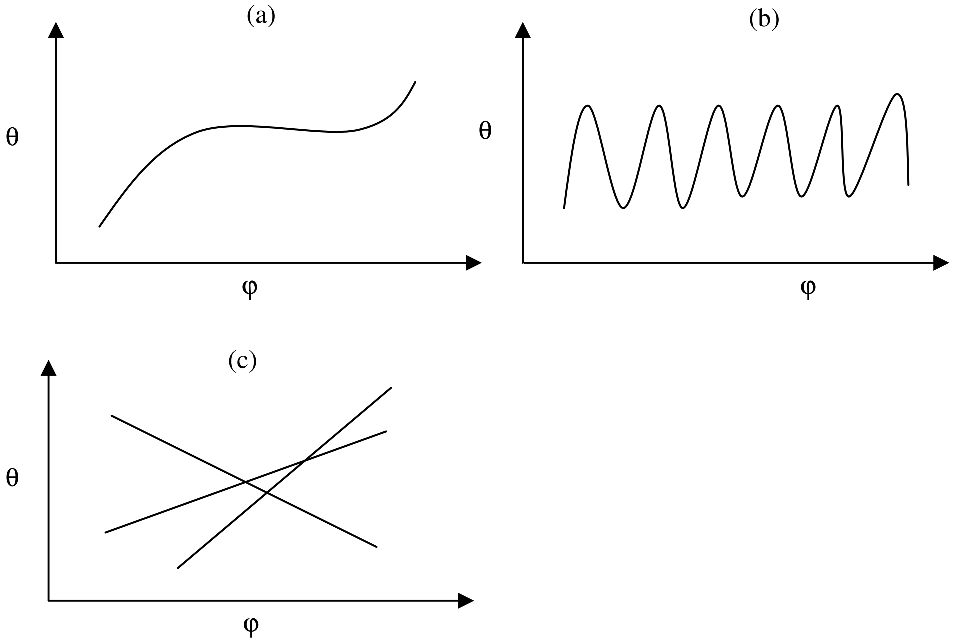

Fig. 4.1 Possible 3D motions encountered in real ISAR data collection. (a) Slight 3D motion deviating from 2D motion. (b) Severe wave-like 3D motion. (c) Multiple flight paths of 2D motion.

For the standard 2D ISAR imaging problem, 3D motion of a target is considered undesirable and its detrimental effect on the 2D ISAR imaging result has been analyzed in [3]. To date, there is no good method to deal with how to image in the presence of unknown 3D motion [27]. However, when the motion data are known, there is an opportunity to produce a 3D image. With the known motion data, the collected radar data is available in the (frequency)-(azimuth)-(elevation) domain. Based on the 3D point scatterer model, 3D ISAR imaging is straightforward based on the Fourier transform.

The problem for 3D ISAR image formation with the Fourier transform is data availability. Governed by the Nyquist sampling theorem, the Fourier transform method requires data that are dense enough in the angular aperture. By examining Figure 4.1, it is usually the case that the available radar data in practice are severely undersampled over the 2D angular aperture. This makes the Fourier transform method unsuitable for the 3D ISAR imaging problem.

In this chapter, the objective is to reconstruct the 3D ISAR image of a target assuming the 3D motion of the target is known. Similar topics have been reported in [25, 26, 31]. In [26], a mosaic 3D image is produced from many 2D images formed using a super-resolution algorithm. In [25], the target height is reconstructed using multiple cuts of elevation data. In [31], a relaxation-based algorithm is used to address the so-called curvilinear SAR problem.

The approach is to use an adaptive feature extraction algorithm based on a general 3D point scatterer model. It is an extension of the previous work in [32], where only 2D motion is considered. Here, both the case of severe and slight 3D motions are considered. When there is severe 3D motion of the target, the goal is to form a 3D ISAR image. When there is only slight 3D motion that deviates from 2D motion, the goal is to achieve a better 2D ISAR image.

This chapter is organized as follows. In Section 4.2, the 3D point scatterer model is introduced to account for 3D target motion. The adaptive feature extraction algorithm is then described in Section 4.3. In Section 4.4, the advantages of this algorithm are shown with some simple point scatterer simulations and the limitations of the algorithm are discussed. The algorithm is then applied to reconstruct 3D images of an aircraft from realistic ISAR motion data. Conclusions are given in the final section.

4.2 3D Point Scatterer Model

A 2D point scatterer model is usually used in traditional ISAR imaging [1, 12]. In this model, the target consists of ideal point scatterers. After range compression, the radar data can be expressed as

$$E(t_D) = \sum_{i=1}^{Ns} \sigma_i \exp\{-j\frac{4\pi f_0}{c}[x_i + y_i\varphi(t_D)]\} \qquad (4.1)$$

where f_0 is the radar center frequency and t_D is the dwell time. x and y represent the target range and cross-range positions, respectively. The target is assumed to consist of N_s point scatterers, with the i^{th} point scatterer depicted by position (x_i,y_i) and strength σ_i.

The above model is valid only if the target rotational motion is confined to a 2D plane and can thus be described in terms of only one angular parameter φ. When there is 3D motion of the target, a more general 3D model is required:

$$E(t_D) = \sum_{i=1}^{Ns} \sigma_i \exp\{-j \frac{4\pi f_0}{c} [x_i + y_i \varphi(t_D) + z_i \theta(t_D)]\} \tag{4.2}$$

In the above expression, a third coordinate, *z*, of the target is included to represent the third dimension of the target and another independent angular motion parameter θ is introduced to describe the 3D motion.

If the target angular motion parameters (ϕ, θ) as a function of dwell time is known, then the radar data are actually in the (azimuth)-(elevation) domain. Therefore, equation (4.2) can be rewritten as

$$E(\varphi, \theta) = \sum_{i=1}^{Ns} \sigma_i \exp\{-j \frac{4\pi f_0}{c} [x_i + y_i \varphi + z_i \theta]\} \tag{4.3}$$

Based on (4.3), it is seen that if both θ and φ are evenly sampled over the 2D angular aperture, a 2D fast Fourier transform with respect to θ and φ can be used to form a 3D radar image in the range *x* and cross ranges *y* and *z* domain. If the data are unevenly sampled yet dense enough, the Fourier transform can still be used to process the radar data. However, when the available data are highly undersampled as those shown in Figure 4.1, the Fourier transform method will not produce any meaningful results. To overcome the undersampling problem, the so-called adaptive feature extraction algorithm is proposed in the next section.

4.3 Adaptive Feature Extraction Algorithm

Adaptive feature extraction (AFE) is a model-based signal processing method that has been used in a previous work for 2D ISAR imaging [32]. It is similar to

CLEAN [33] and the matching pursuit algorithm [34]. After range alignment, the range position is resolved via range compression. The two cross range dimensions are obtained by applying AFE based on the 3D point scatterer model to the radar data within a range bin. The basic idea is to extract the strongest point scatterer first. Then the response from this point scatterer is subtracted from the total signal. The process is then iterated for the remaining point scatterers.

Within a particular range bin, for every possible point scatterer position *(y, z)*, a basis function is reconstructed as the radar signal from a unit point scatterer located at position *(y, z)* using the model depicted in (4.3)

$$h(t_D) = e^{-j\frac{4\pi f_0}{c}[y\phi(t_D)+z\theta(t_D)]} \tag{4.4}$$

To find the strongest point scatterer within the range cell, the basis function is searched for to give rise to the maximum projection from the radar data $E(t_D)$ onto the basis. That is, the position of the strongest point scatterer (y_m, z_m) can be found as

$$\{y_m, z_m\} = \arg\max |< E(t_D), h(t_D) >| \tag{4.5}$$

where the projection is defined as

$$< E(t_D), h(t_D) >= \int E(t_D) h^*(t_D) dt_D \tag{4.6}$$

After the position of the strongest point scatterer is found, the strength σ_m of that point scatterer is simply the projection from the radar data onto the chosen basis function:

$$\sigma_m =< E(t_D), e^{-j\frac{4\pi f_0}{c}[y_m\phi(t_D)+z_m\theta(t_D)]} > \tag{4.7}$$

Once the contribution from the strongest point scatterer to the radar signal is found, it is denoted as

$$E_m = \sigma_m e^{-j\frac{4\pi f_0}{c}(y_m\phi + z_m\theta)} \tag{4.8}$$

E_m is then subtracted from E to find the residual signal:

$$E_{m+1} = E - E_m \tag{4.9}$$

Finally, this process is iterated to find the subsequent point scatterers one at a time until the energy of the residual signal falls below a preset threshold.

To summarize, the steps in the adaptive feature extraction algorithm are as follows:

Step 1. Set up the search space for both y and z.

Step 2. Search for maximum projection from the present signal onto the search space. The two cross range positions and the strength of the strongest point scatterer within the range bin are determined.

Step 3. Remove the response of the point scatterer from the radar signal.

Step 4. Repeat steps 2 and 3 until the energy of the residual signal falls below a predefined threshold.

Step 5. Repeat the above procedures for other range bins.

For this work, the exhaustive search method is used in step 2. It is guaranteed to produce a global maximum for the projection. To further save computation time, the use of genetic algorithm is also explored instead of the exhaustive search for more efficient global optimization [35].

4.4 Results

To demonstrate the use of AFE for ISAR image formation of a target with 3D motion, the result is first compared against that from the Fourier transform. The resolution and noise sensitivity of the algorithm are then studied. After the advantages and limitations of the AFE algorithm being established, 3D images from some simulated radar data based on real motion data from an air target are reconstructed.

4.4.1 Testing on the AFE Algorithm

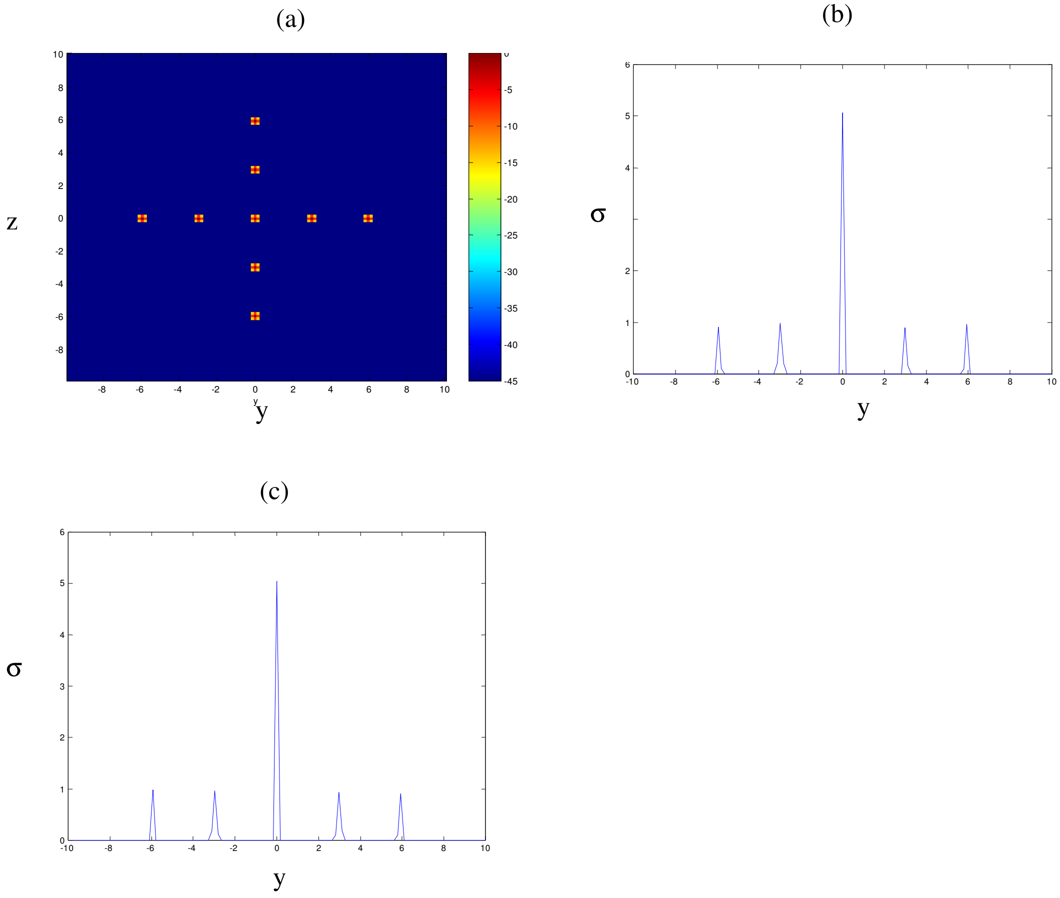

Fig. 4.3 Orignal 9 point scatterers within in one range cell. (a) (y, z) distribution. (b) y projection. (c) z projection.

To test the algorithm, radar data from a fixed range cell are considered and how to resolve the two cross range dimensions using AFE is studied. A target consisting of nine point scatterers of equal strength in the (y, z) plane at a fixed range is shown in Figure 4.2a. The two projections of the point scatterers along the y and the z axes are shown in Figures 4.2b and 4.2c respectively. With the point scatterer model and assumed 3D motion, simulated radar data are generated based on equation (4.2). The center frequency is 10GHz and the bandwidth is 1GHz in the simulation. The AFE algorithm is then applied to the simulated radar data.

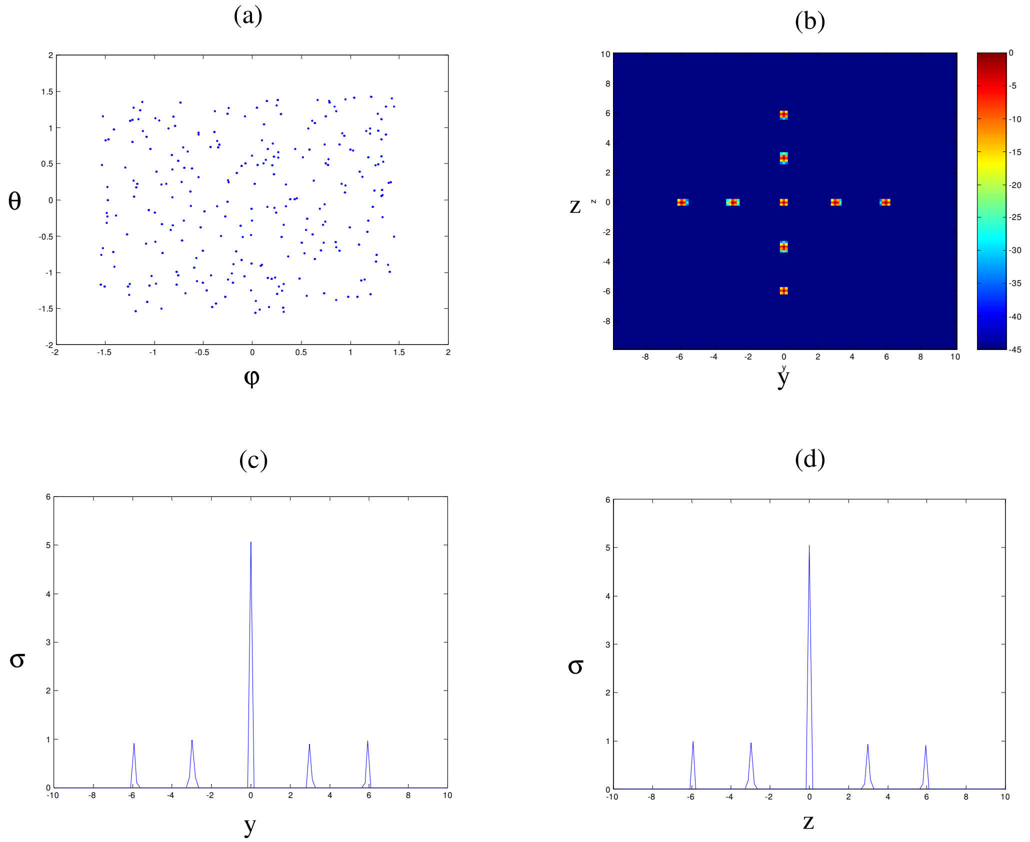
(a) (b) (c) (d)

Fig. 4.3 Reconstruction result using AFE. (a) Motion data in a 3 deg by 3 deg aperture. (b) (y, z) image. (c) y projection. (d) z projection.

The first case considered is severe 3D motion as shown by the azimuth-elevation data in Figure 4.3a. In this figure, 256 data points over a 3-degree azimuth by 3-degree elevation aperture are randomly distributed. The AFE reconstructed image in the (y, z) plane is illustrated in Figure 4.3b. The two projections along the y and the z axes are shown in Figures 4.3c and 4.3d respectively. It can be seen that they agree well with the reference images in Figures 4.2a–4.2c. The small errors are due to finite position resolution in the search space.

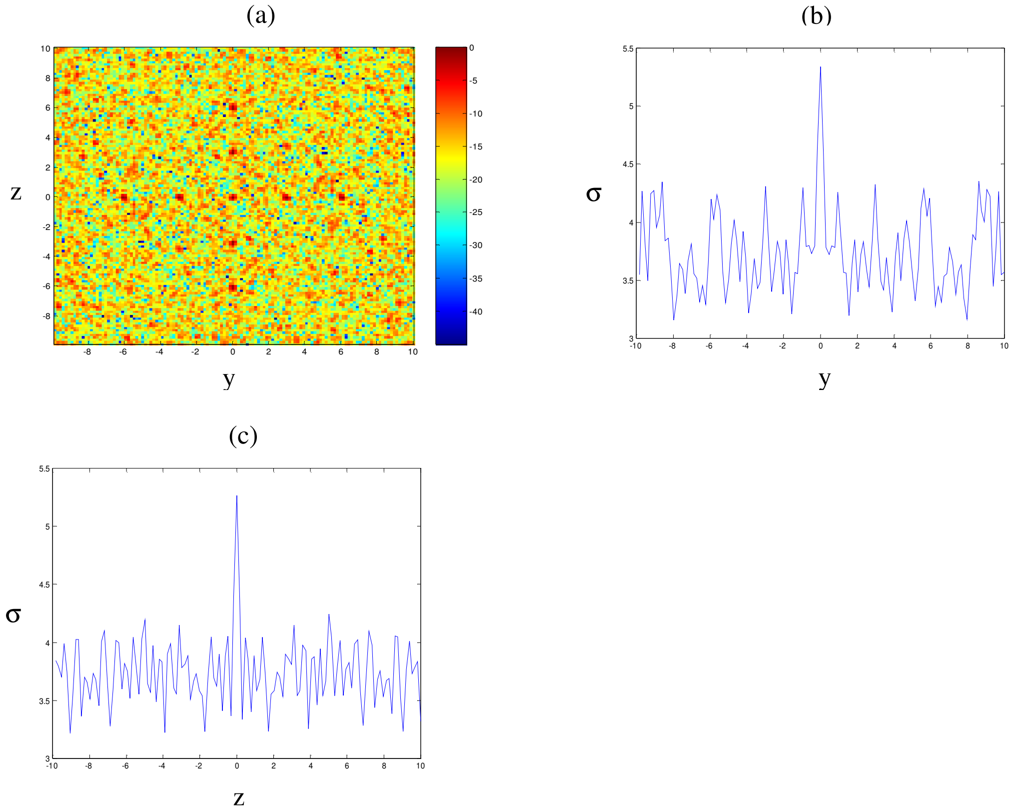

Fig. 4.4 Reconstruction results using the Fourier transform. (a) (y, z) image. (b) y projection. (c) z projection.

Next, the image is generated via the Fourier transform. The result of the (*y*, *z*) image is shown in Figure 4.4. It is obtained by a Fourier transform over the non-uniform angular aperture. The sidelobes are so high that the positions of the point scatterers cannot be easily recognized in the (*y*, *z*) image or the two projections. This is due to the large aliasing effect associated with the undersampled data. The Nyquist sampling in angle is about 0.07 degree, while the actual average sampling of the data is about 0.19 degree. A good image is not expected to be obtained by the Fourier transform method. Therefore, AFE is a much better choice than the Fourier transform to process the undersampled radar data at hand.

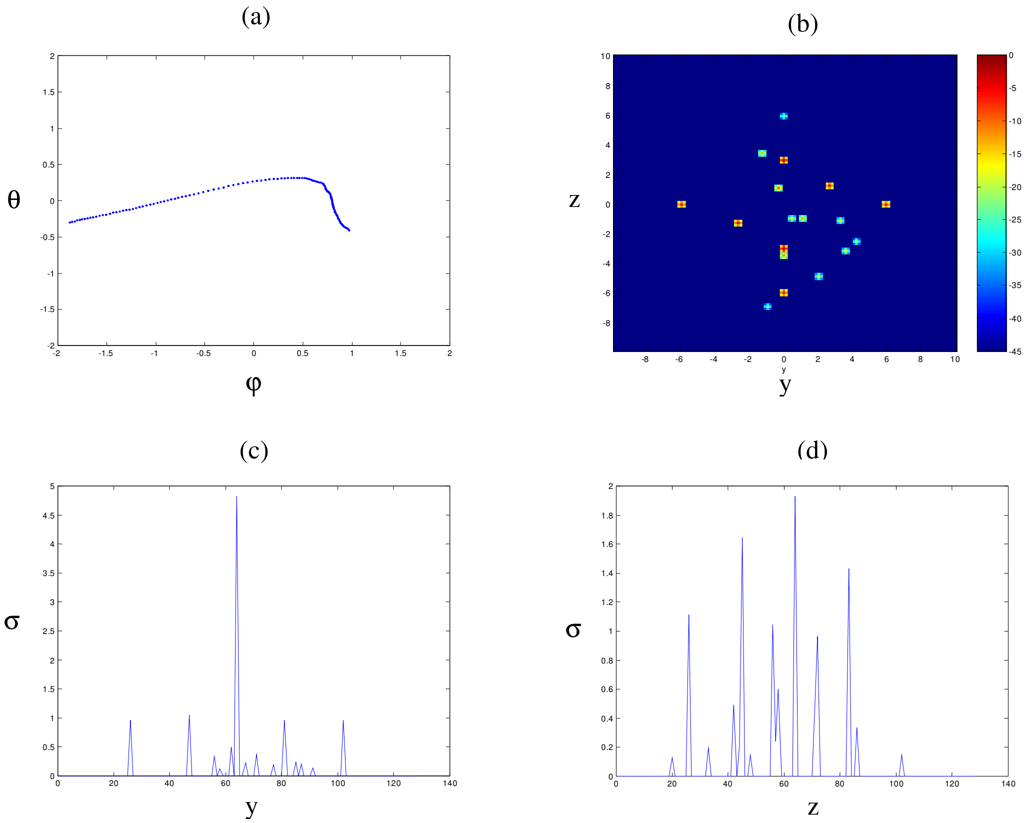

Fig. 4.5 AFE reconstruction from data with a slight 3D motion. (a) Motion data. (b) (y, z) image. (c) y projection. (d) z projection.

The second case considered is slight 3D motion as shown in Figure 4.5a. The motion parameters in this figure are taken from the real motion data of an in-flight aircraft. The azimuth and elevation angles are obtained through coordinate transformation of the original roll, yaw and pitch motions of an instrumented aircraft. As it can be seen, there is a slight 3D motion that deviates from the idealized 2D motion, which should be a line in the θ-φ aperture. In this case, AFE is applied based on both the correct 3D motion model in (4.2) and the approximate 2D motion model in (4.1). In the former case, the AFE search is over the (y, z) space, while in the latter case, the search is a one-dimensional one over the y dimension only. Figure 4.5b shows the (y, z) image resulting from the 3D motion model. The two projections along the y and the z axes are shown in Figures 4.5c and 4.5d. At first glance, the image in Figure 4.5b does not look like the original image in Figure 4.2a at all. However, it can be seen that the y projection in Figure 4.5c agrees fairly well with the original y projection in Figure 3b. On the other hand, the z projection in Figure 4.5d is very different from the original z projection in Figure 4.2c. The reason for the poor performance is that the variation in φ is only one-fifth of the variation in θ, which makes the image resolution in z much lower than the image resolution in y. The resolution of the AFE algorithm is discussed in more detail in 4.4.2.

Figure 4.6 shows the AFE result based on the 2D motion model. Only the y projection is available from the one-dimensional AFE search. The y positions from this figure do not reflect the true y positions of the 9 point scatterers shown in Figure

4.2b. The mistake here is due to model mismatch. Although the variation in the elevation angle θ is only one-fifth of the variation in the azimuth angle φ, this slight 3D motion cannot be ignored in processing the radar data. Therefore, the full 3D motion model in conjunction with the AFE algorithm is needed for image formation in the presence of 3D motions.

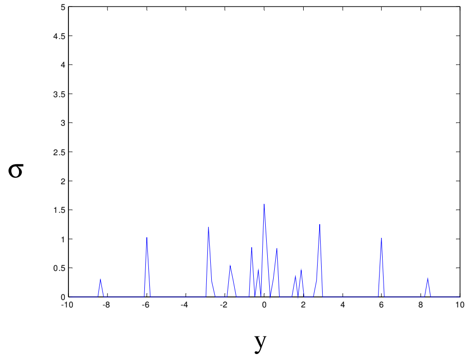

Fig. 4.6 AFE reconstruction from data with a slight 3D motion based on a 2D motion model.

4.4.2 Resolution and Sensitivity of the AFE Algorithm

As seen in the last section, even though the AFE algorithm can overcome the undersampling problem, the resulting image resolution is still controlled by the aperture size. To further illustrate this, the 3 degree by 3 degree aperture in Figure 4.3a is scaled to a 0.3 degree by 3 degree aperture in Figure 4.7a, while still populating the aperture with 256 data samples. The same 9 point scatterers and radar parameters are used to simulate the radar data. Only the motion data is different. The AFE reconstruction results are shown in Figures 4.7b-4.7d. As it can be seen by a comparison between Figures 4.7 and 4.2, the image resolution in the *y* direction remains essentially unchanged, while the image resolution in the *z* dimension gets much worse. Therefore, the AFE resolution in position is inversely proportional to the angular aperture. This is exactly the same as the Fourier transform.

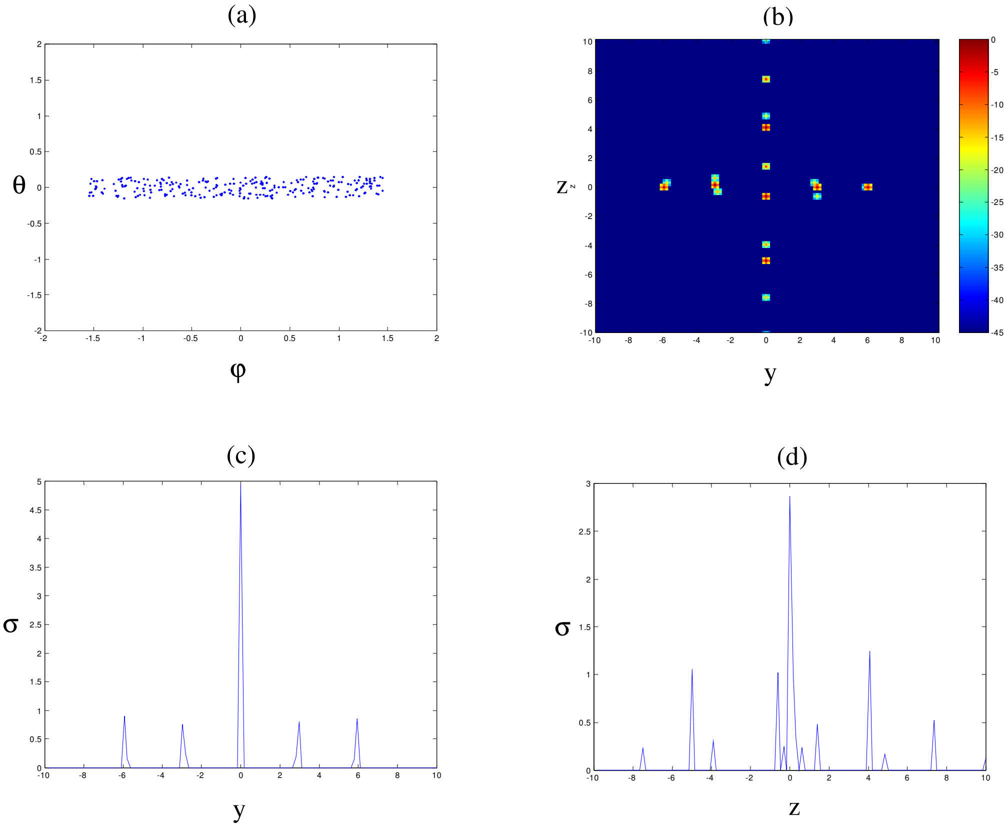

Fig. 4.7 Reconstruction results using AFE. (a) Motion data in a 3 deg by 0.3 deg aperture. (b) (y, z) image. (c) y projection. (d) z projection.

Like many other model-based signal processing techniques, the adaptive feature extraction algorithm is sensitive to data error. The algorithm sensitivity is studied by adding some noise to the data. Two types of errors are considered. The first is the radar data error. Figure 4.8a shows the reconstructed image when the radar data is contaminated with -20dB of white noise. The second source of error is the motion parameter error. Figure 4.8b shows that the result with 1% random error in the motion parameters. It is shown that the algorithm is more sensitive to error in the motion parameters than that in the radar data. To alleviate the angular motion error, preprocessing the motion data according to *a priori* knowledge of the motion is suggested. For example, the motion data can be limited to low-order polynomial functions of dwell time if the motion of the target is believed to be smooth.

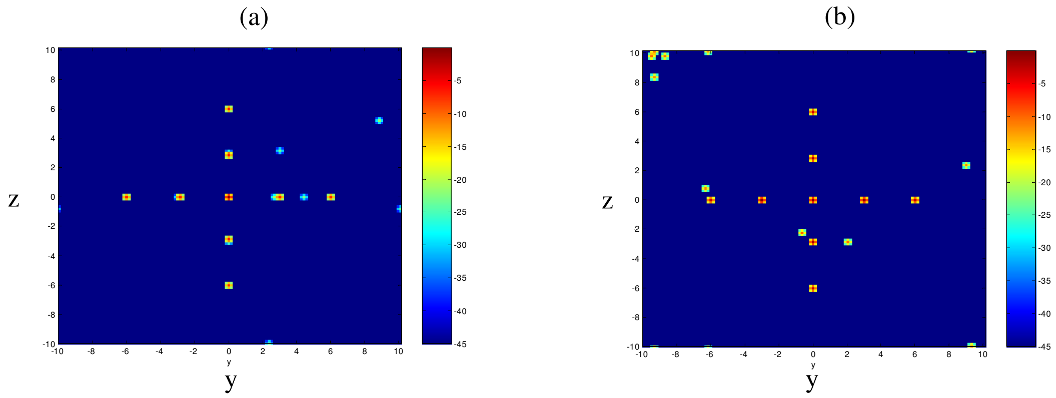

Fig. 4.8 Reconstruction using noisy data. (a) -20dB white noise in the radar data. (b) 1% randomness in the angular positions.

4.4.3 Aircraft Imaging with Real 3D Motion Data

A full simulation is done with point scatterers from an aircraft model. 401-point scatterers with equal strength are used to model the example aircraft as shown in Figure 4.9a. The three projections of the original target corresponding to the top view, side view, and front view of the aircraft are shown in Figures 4.9b-4.9d. The 3D motion data in Figure 4.10 shows a 5 degree by 5 degree angular window in both azimuth and elevation. They are from the actual flight paths of an aircraft. To simulate the radar data, the same radar parameters in the previous examples are used. The goal is to reconstruct a 3D image from the range profiles simulated at these angles. Again, the highly non-uniform, undersampled distribution of the radar data in the angular aperture requires the use of the 3D motion model and the AFE algorithm in order to reconstruct a 3D image.

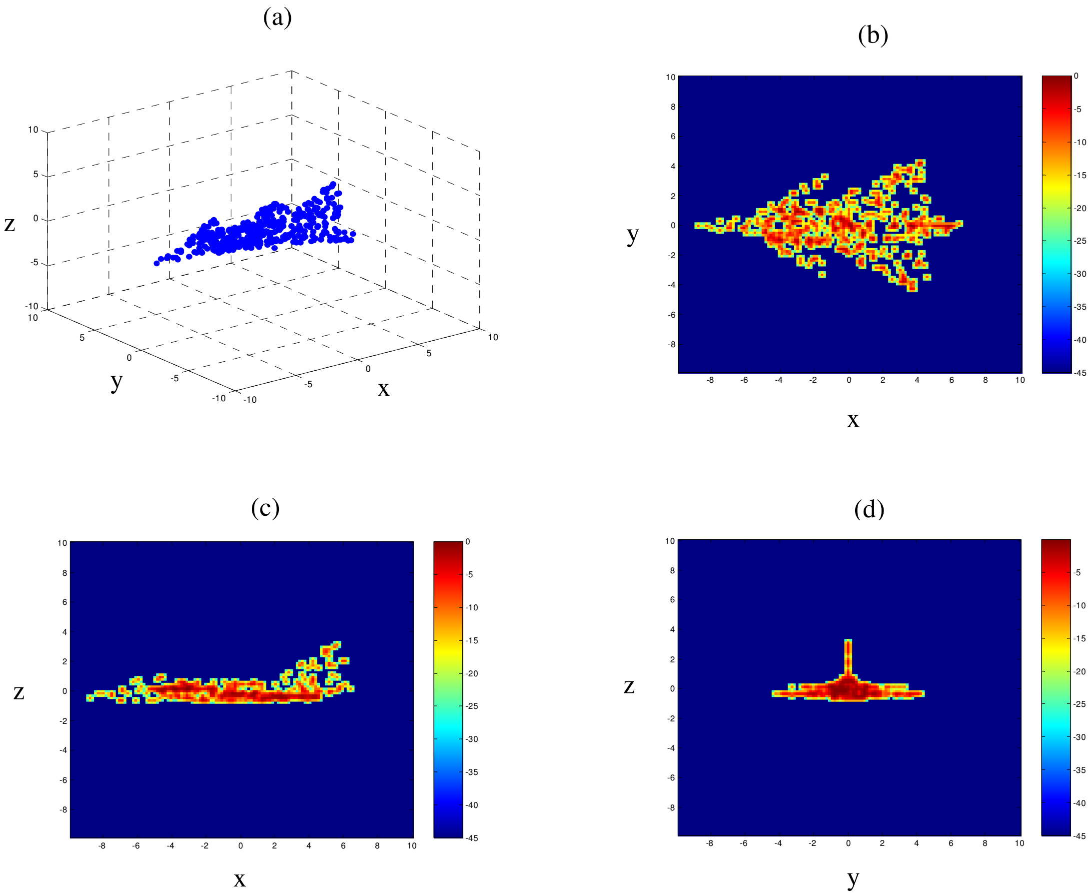

Fig. 4.9 Point scatterer representation of an aircraft. (a) 3D point scatterer representation. (b) Top view. (c) Side view. (d) Front view.

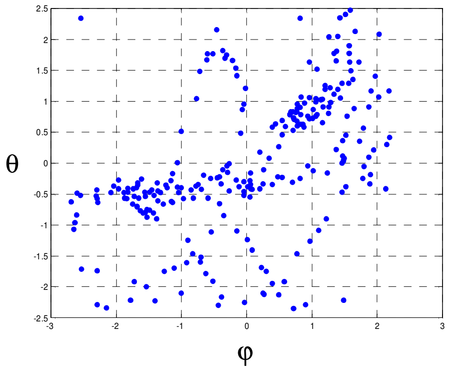

Fig. 4.10 3D motion data from an air target.

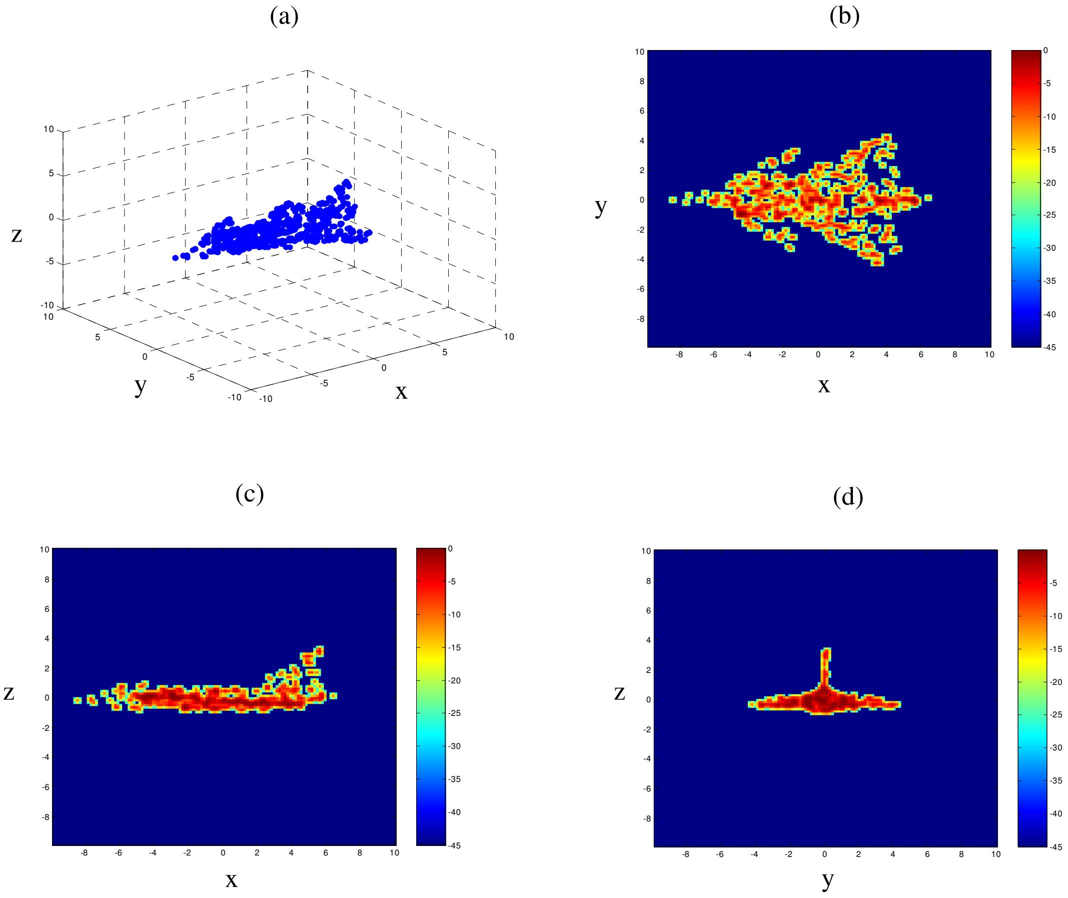

Fig. 4.11 3D image reconstructed by AFE based on the 3D motion model. (a) 3D view of the top 600 extracted point scatterers (b) Top view. (c) Side view. (d) Front view.

For 3D image construction, the positions and strengths of the point scatterers in 3D space are needed to be found. The range location x_s is directly obtained from the range profiles. Then for every range cell within the range profile, a collection of point scatterers with two cross-range locations (y_s, z_s) and point scatterer strength σ_s are extracted from the AFE iterations. The result is an image $\sigma_s(x_s, y_s, z_s)$, representing the scattering strength of scatterers in 3D space. The scatterers according to their strengths are sorted and the top 600 point scatterers are kept. The positions of those point scatterers are shown in Figure 4.11a. The top view, side view, and front view of the reconstructed 3D image are shown in Figures 4.11b-11d, respectively. They agree very well with the three projections from the original 3D point scatterers in Figure 4.9. Such features as the fuselage, the wings, and the vertical tail fin are correctly constructed. The algorithm has also been tested on real radar data of an air target.

4.5 Conclusions

The problem of 3D ISAR imaging of a target with known motion data is discussed in this chapter. The 3D motion model is necessary to form a 3D image of the target with 3D motion. The adaptive feature extraction algorithm along with the 3D motion model is proposed to process non-uniform, undersampled radar data collected over a 2D angular aperture. The advantages of the AFE algorithm are clearly demonstrated when compared to either the Fourier transform or the AFE based on 2D motion model. It is found that the resolution of the AFE image is limited by the aperture size in the corresponding motion direction. The sensitivity of the method is also discussed. Simulation with a 3D point scatterer model of an aircraft shows that the resulting 3D images carry much more information than the range profiles or the 2D ISAR images alone. One advantage of the algorithm is that the data collection scheme is very flexible. Therefore, it is a viable tool for target feature extraction when the 3D motion data associated with the target are available.

The significance of this work is twofold. First, when there is known target motion, 3D motion is taken into account based on the 3D motion model. It is not treated as an error term as in traditional 2D ISAR imaging. Second, when there is unknown target motion, this work provides an intermediate step toward blind 3D ISAR image formation. Instead of doing the more challenging 3D motion compensation directly, the 3D motion might first be estimated from the radar data. This method can then be used to form a 3D image.

So far, we have addressed the problem of the first motion assumption- a 2D motion assumption. 3D motion detection has been discussed in the last chapter and 3D motion detection has been discussed in this chapter. The problem of violation of the second motion assumption- the rigid-body motion assumption will be addressed in the next chapter.

Chapter 5 ISAR Feature Extraction from Non-Rigid Body Targets Using Adaptive Chirplet Signal Representation

This chapter addresses the problem of feature extraction from inverse synthetic aperture radar (ISAR) data collected from targets with rotating parts. In traditional ISAR imaging, rigid-body motion is usually assumed. When non-rigid body motions are present, it is not possible to obtain a focused image of both the target and the rotating part. To solve this problem, the radar signal is first parameterized using the adaptive chirplet signal representation. The signal from the body and that from the rotating part are then separated in the parameter space. Point scatterer simulation results show that better geometrical feature about the body and better micro-Doppler feature about the rotating part can be extracted after the separation. The algorithm is also demonstrated using the measurement data from an in-flight aircraft and a walking person.

5.1 Introduction

Recently, there has been increasing interest in studying the so-called micro-Doppler phenomenon [36, 37] for radar target identification applications. Micro-Doppler is used to describe the fine Doppler feature from some moving part on the target that is different from the main body Doppler feature. In most of the conventional work on inverse synthetic aperture radar (ISAR) imaging, the target is assumed to have rigid-body motion [1-3, 8-12]. However, non-rigid body targets can often be found in real-world situations. As a simple case, a target may consist of a main body and a rotating part. For example, an in-flight aircraft with jet engine rotation, a ship with scanning antenna motion and a ground vehicle with spinning tire motion all involve this type of configuration. Under these conditions, difficulties in understanding the resulting ISAR image arise due to the violation of the rigid-body assumption.

In this chapter, the objective is to extract better target features from ISAR data when a target has a rotating part besides the main body. The challenge is that the body image is contaminated due to the interference from the rotating part. It is also more difficult to extract the motion information from the rotating part as it is overshadowed by the body returns. The approach is to first parameterize the radar signal using the adaptive chirplet representation [38, 39]. The chirplet basis is a four-parameter function localized in the joint time-frequency plane. While both Gaussian [9] and chirp-type [20] bases have been reported for joint time-frequency processing of ISAR data, the chirplet basis is selected to represent the radar signal in this chapter. Since both amplitude modulation (AM) and frequency modulation (FM) are part of the basis, chirplet can more efficiently represent the radar signal from a target with a rotating part. With the adaptive chirplet representation, different motion behaviors of the target components are mapped into different parameters of the corresponding bases. Consequently, the returns from the body and the rotating part can be more easily separated. After the separation, better target feature extraction can be realized by processing the two parts individually. This includes both the extraction of the geometric features from the main body and the micro-Doppler features from the moving part.

The chapter is organized as follows. In Section 5.2, the model and formulation of the problem are presented. After a close examination of the point scatterer signal model of a target with individual motions, it is shown that the chirplet basis is well suited for parameterizing and separating the rotating part signal from the main body signal. In Section 5.3, the chirplet-based adaptive signal representation algorithm is tested with point scatterer simulation data. Section 5.4 shows the results from two sets of measurement data. The first data set is from an in-flight aircraft with jet engine rotation motion. The second data set is from a walking person with arm swing motion. Conclusions are given in Section 5.5.

5.2 Signal Model and Formulation

5.2.1 Point Scatterer Model of Radar Signal from Target with Rotating Part

The point scatterer model is usually used in radar imaging to model the radar signal scattered by an unknown target. In this model, the radar return signal is expressed as a sum of point scatterer responses:

$$E(f,t)=\sum_{m=1}^{M}\sigma_m e^{-j\frac{4\pi f}{c}[R_m(t)+x_m\cos\theta_m(t)+y_m\sin\theta_m(t)]} \tag{5.1}$$

where the radar signal E is a two-dimensional function of transmitting radar frequency f and pulse dwell time t. The target consists of M point scatterers, each with position (x_m , y_m) and complex scattering coefficient σ_m. Suppose the radar is stationary, the target motion is described by the translation motion $R_m(t)$ and the angular motion $\theta_m(t)$ for each scatterer.

A rigid body target is usually assumed in traditional ISAR imaging, i.e. all the point scatterers in (5.1) share the same translation motion $R_m(t)$ and rotational motion $\theta_m(t)$. Here, a non-rigid body target consisting of two parts- a main body and a rotating part- shall be considered. In this case, the model in (5.1) can be simplified by using different motions for the two parts while still applying the rigid-body assumption for each part. This leads to

$$\begin{aligned} E(f,t) &= E_B(f,t) + E_R(f,t) \\ &= \sum_{m=1}^{M} \sigma_m e^{-j\frac{4\pi f}{c}[R_B(t)+x_m \cos\theta_B(t)+y_n \sin\theta_B(t)]} + \sum_{n=1}^{N} \sigma_n e^{-j\frac{4\pi f}{c}[R_R(t)+x_n \cos\theta_R(t)+y_n \sin\theta_R(t)]} \end{aligned} \tag{5.2}$$

with subscripts *B* and *R* denoting the body and the rotating part, respectively.

Both the main body and the rotating part move with respect to the radar. The difference is that the rotating part has an additional rotation motion besides all the motions of the main body. For the main body, during the imaging interval the small angle approximation usually used in ISAR imaging can be applied. That is,

$$\begin{cases} \cos\theta_B(t) \approx 1 \\ \sin\theta_B(t) \approx \theta_B(t) \end{cases} \tag{5.3}$$

It is also assumed that a standard motion compensation algorithm [3, 11, 41] has been utilized to remove both the translation motion and the non-uniform rotational motion from the body, after which

$$\begin{cases} R_B(t) = 0 \\ \theta_B(t) = \omega_B t \end{cases} \tag{5.4}$$

where ω_B is the effective body rotation rate after the motion compensation.

For the rotating part, the motion relative to the main body is rotation only. This implies that the rotating part has the same translation motion as that of the body, i.e.

$$R_R(t) = 0 \tag{5.5}$$

However, the small-angle approximation does not hold for the rotating part. Since its rotation rate is usually much larger than that of the main body, a rotating scatterer might undergo many cycles while the main body rotates only a few degrees during the imaging interval. Substituting equations (5.3) – (5.5) into (5.2)

$$E(f,t) = \sum_{m=1}^{M} \sigma_m e^{-j\frac{4\pi f}{c}[x_m + y_m \omega_B t]} + \sum_{n=1}^{N} \sigma_n e^{-j\frac{4\pi f}{c}[x_n \cos\theta_R(t) + y_n \sin\theta_R(t)]} \tag{5.6}$$

which is the radar signal from a target with a rotating part in the two-dimensional (frequency, dwell time) domain after motion compensation of the main body. Since it is more efficient to process range compressed data, (5.6) is Fourier transformed with respect to *f* and bring the radar data into the (range, dwell time) domain. The radar signal through a fixed range cell *r* is given by

$$\begin{aligned} E_r(t) = \sum_{m=1}^{M} \sigma_m e^{+j\frac{4\pi f_c}{c}(r - x_m - y_m \omega_B t)} + \\ \sum_{n=1}^{N} \sigma_n \operatorname{sinc}\left\{ \frac{2\pi f_{bw}}{c} \left[r - x_n \cos\theta_R(t) - y_n \sin\theta_R(t) \right] \right\} e^{+j\frac{4\pi f_c}{c}[r - x_n \cos\theta_R(t) - y_n \sin\theta_R(t)]} \end{aligned} \tag{5.7}$$

where f_{bw} is the bandwidth of the radar.

Some observations can be made here about (5.7). There exist substantial differences between the main body signal and the rotating part signal. Each body scatterer in the first term has constant amplitude σ_m and constant Doppler frequency -$(2f_c/c)\omega_B y_m$ with respect to *t*. However, the signal of each rotating scatterer in the second term contains both AM and FM components. This can be seen by the presence of the time-varying function $\theta_R(t)$ in both the *sinc* and the exponential terms. Consequently, a second Fourier transform of (5.7) with respect to *t* will focus the target body in cross range, but not the rotating part return. This results in the observed interference from the rotating part in the ISAR image.

5.2.2 Chirplet Basis

The chirplet basis function [38, 39] is well suited for parameterizing the AM-FM radar signal in (5.7). A chirplet is a four-parameter basis in the form of

$$h_k(t) = \left(\frac{\pi}{\alpha_k} \right)^{\frac{1}{4}} e^{-a_k (t-t_k)^2} e^{-j2\pi f_k (t-t_k) - j\pi\beta_k (t-t_k)^2} \tag{5.8}$$

where t_k is the time center of the signal, f_k is the center frequency, β_k is the frequency modulation rate, and α_k defines the time extent of the signal. The joint time-frequency plot of a chirplet function is illustrated in Figure 5.1a.

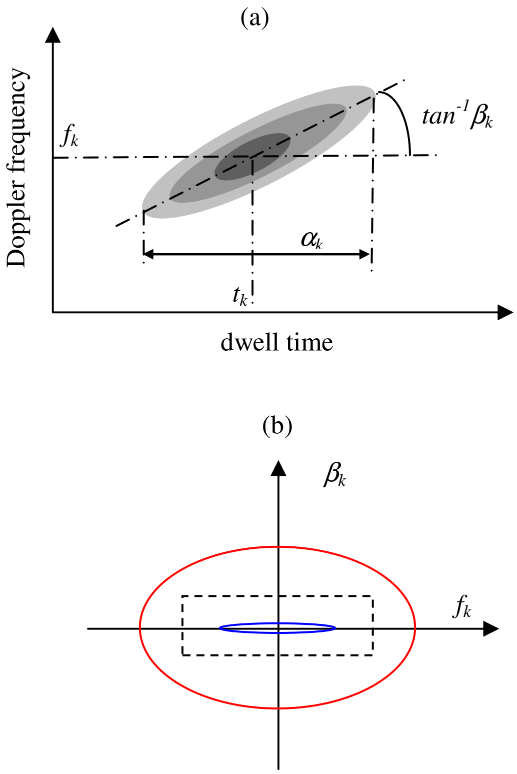

Fig. 5.1 (a) Joint time-frequency representation of a chirplet basis. (b) Distribution of chirplet parameters for the main body (blue) and rotation parts (red), and separation thresholds (dashed).

Actually, chirplet basis is one of the many options that can be used to model the radar signal accurately. However, there are some attractive attributes of this basis. First, the basis function is an AM-FM signal, which approximately reflects the time-frequency structure of the radar signal in (5.7). Second, the chirplet basis is a well-understood basis with only four parameters. Only moderate computation time is needed to search for the basis parameters. Third and most importantly, the parameters of the chirplet can be used to separate the two components of the signal. This is because signals from the main body and the rotating part are captured by chirplet bases with different parameters.

To see this more explicitly, assume a first order rotational motion in the time neighborhood of each chirplet:

$$\theta_R(t) = \theta_c + \omega_R(t - t_k), \quad |t - t_k| < \varepsilon \tag{5.9}$$

where θ_c is the angle at the time center and ε is a small number. The rotating part is assumed to have a constant rotation rate ω_R during the small time interval although it could have more complex motions during the whole imaging interval.

After substituting (5.9) into (5.7), the first and second derivatives of the phase term are taken with respect to t and compared to those from (5.8) to arrive at expressions for f_k and β_k. The results can be written as

$$\begin{aligned} f_k &= -\frac{2f_c}{c}\omega_R[x_n \sin\omega_R(t - t_k) - y_n \cos\omega_R(t - t_k)] \\ &= -\frac{2f_c}{c} l_n \omega_R \sin[\omega_R(t - t_k) - \zeta_n] \end{aligned} \tag{5.10a}$$

$$\beta_k = -\frac{2f_c}{c} l_n \omega_R^2 \cos[\omega_R(t - t_k) - \zeta_n] \tag{5.10b}$$

where (l_n, ζ_n) are the polar representations of (x_n, y_n). It can be seen from equations (5.10a) and (5.10b) that the parameters f_k and β_k are distributed along an ellipse as follows:

$$\frac{f_k^2}{(l_n\omega_R)^2} + \frac{\beta_k^2}{(l_n\omega_R^2)^2} = \left(\frac{2f_c}{c}\right)^2 \tag{5.11a}$$

where the size and the axial ratio of the ellipse are controlled by ω_R and l_n. Similarly, the equation to associate the chirplet parameters with the main body signal is given by

$$\frac{f_k^2}{(l_m\omega_B)^2} + \frac{\beta_k^2}{(l_m\omega_B^2)^2} = \left(\frac{2f_c}{c}\right)^2 \tag{5.11b}$$

where the scatterer radial length l_m and the rotation rate ω_B are used for the main body.

Even though (5.11a) and (5.11b) have exactly the same form, the main body and the rotating part are separable in the parameter space because of their different motions. Essentially, while the sizes of the two parts are comparable, the rotating part rotates much faster than the main body during the imaging interval, i.e.

$$\omega_R >> \omega_B \tag{5.12}$$

Consequently, the chirplet parameters f_k and β_k for the main body and the rotating part are distributed very differently in the parameter space. A rotating part scatterer is represented as a larger and rounder ellipse while a body scatterer is represented as a smaller and flatter ellipse. Actually, the ellipse for the main body is nearly a line segment on the f_k axis since the first term of (5.7) is assumed to have zero Doppler rate. The different distributions of the chirplet parameters are illustrated in Figure 5.1b, where the outer ellipse represents the rotating part signal while the inner one represents the main body signal. A simple criterion to separate the two parts can thus be defined: the body signal has small f_k and β_k while the rotating part signal has either large f_k or β_k.

Another interesting observation from the above discussion is that the main body and the rotating part signals have large overlaps in f_k while they have little overlap in β_k. Therefore, the Doppler rate is more important than the Doppler frequency in separating the two signal components. This point will be further illustrated in the examples later.

5.2.3 Signal Separation Based on Adaptive Chirplet Signal Representation

The radar signal is decomposed into a set of chirplet bases using the adaptive signal representation [34, 40]. The radar signal in a fixed range cell with returns from both the body and the rotating part, which is labeled as $E_r(t)$ in (5.7), is used. Next, $E_r(t)$ is parameterized using a series of chirplet basis functions as follows:

1. Set index $k = 1$ and the residual signal $R_k(t)=E_r(t)$.
2. Find the k^{th} chirplet $h_k(t)$. The parameters of the chirplet are found by maximizing the projection from the residual signal $R_k(t)$ onto the basis, i.e.

$$\{t_k, f_k, \alpha_k, \beta_k\} = \arg\max \left|\left\langle R_k(t), h_k(t)\right\rangle\right| \tag{5.13a}$$

where the inner product is defined as

$$\left\langle R_k(t), h_k(t) \right\rangle = \int R_k(t) h_k^*(t) dt \tag{5.13b}$$

The coefficient of the chirplet is the corresponding projection:

$$c_k = \left\langle R_k(t), h_k(t) \right\rangle \tag{5.14}$$

3. Subtract the extracted signal from the residual and increment k by one:

$$\begin{aligned} R_{k+1}(t) &\leftarrow R_k(t) - c_k h_k(t) \\ k &\leftarrow k+1 \end{aligned} \tag{5.15}$$

4. Repeat steps 2 and 3 until k reaches a preset number or the energy of the residual signal is below some preset threshold. Suppose N chirplets are found from this procedure, the radar signal is parameterized as

$$E_r(t) \approx \sum_{k=1}^{N} c_k \left(\frac{\pi}{\alpha_k} \right)^{\frac{1}{4}} e^{-a_k (t-t_k)^2} e^{-j2\pi f_k (t-t_k)} e^{-j\pi\beta_k (t-t_k)^2} \tag{5.16}$$

After parameterization of the radar signal, the body signal can be separated from the rotating part signal using the criteria discussed previously. Those chirplets with small f_k and β_k are classified as the main body components and the chirplets with either large f_k or large β_k as the rotating part components. The final body-only signal and the rotating part signal are assembled from the corresponding chirplet bases according to (5.16).

Following the separation, the main body signal and the rotating part signal can be processed individually for better information extraction. Based on the discussion about equation (5.7), for the target body the feature of interest is the geometrical information in the ISAR image. A better body image can be reconstructed after removing the rotating part components. For the rotating part signal, it may be impossible to also construct a focused image of the rotating part if the PRF of the radar is too low. However, it is possible to extract useful information about the motion of the rotating part from the separated data.

5.3 Point Scatterer Simulation Results

Our algorithm is first tested with point scatterer simulation data. Six point scatterers are used in the simulation with five points representing the rigid body and one representing the rotating part. The positions and the strengths of the six scatterers are shown in Figure 5.2. Scatterer 6 rotates around scatterer 2 at a rate of 6.67Hz and a rotation radius of 20cm. The radar is assumed to have a 10GHz center frequency, 800MHz bandwidth, and 1400Hz PRF. The target body rotates about 4 degrees over 384 pulses during the data collection time.

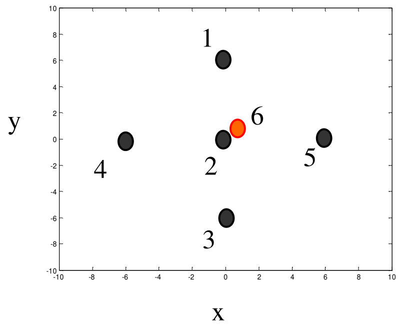

Fig. 5.2 Point scatterer representation of the original target consisting of five rigid points (1-5) and one rotating point (6) with strengths 2, 5, 2, 1, 1, and 3.33, respectively.

Simulated radar data is generated using the point scatterer model in equation (5.6). The resulting radar image is shown in Figure 5.3. The three point scatterers in the center range cell are shadowed by a noisy vertical micro-Doppler band due to the motion of the rotating point scatterer. The objective is to reconstruct the five body scatterers and to estimate the rotation rate of the rotating scatterer from the radar signal.

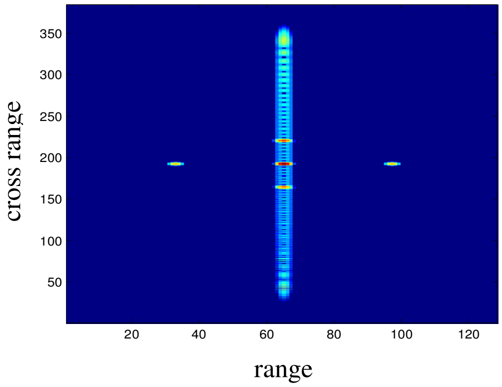

Fig. 5.3 Simulated ISAR image of the target with non-rigid body motion.

Different behaviors of the body and the rotating part are better identified in the joint time-frequency domain. The spectrogram obtained from the short time Fourier transform is shown in Figure 5.4 using the data in range cell 65, which contains responses from scatterers 1, 2, 3 and 6. In this figure, interesting features about the target are observed. First, there are three horizontal Doppler lines. The one at zero Doppler is due to scatterer 2. The two at +/- 100 Hz are due to scatterers 1 and 3. Second, there is a sinusoidal like micro-Doppler curve due to the rotating scatterer 6. Amplitude modulation of this signal is also observed. The spectrogram of the parameterized signal with 100 chirplets is shown in Figure 5.5. Fairly good agreement between the original signal and the parameterized signal is seen.

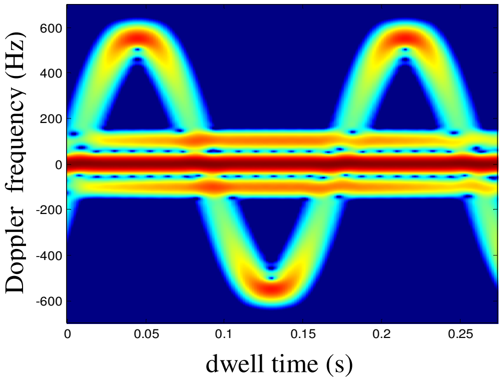

Fig. 5.4 Spectrogram of the radar signal through range cell 65.

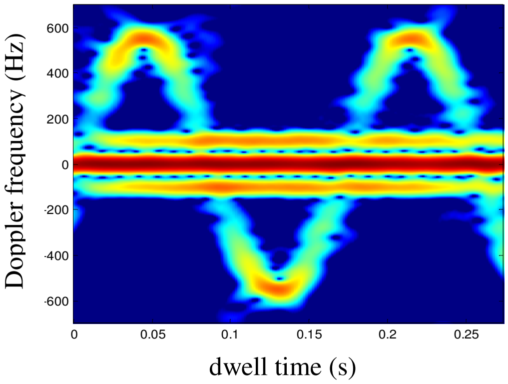

Fig. 5.5 Spectrogram of the parameterized radar signal using 100 chirplet bases.

A simple threshold of 3200Hz/sec on the Doppler rate and 300Hz on the Doppler frequency is used to discriminate the static and dynamic part of the target. The resulting radar signals are shown in Figures 5.6a and 5.6b, for the rigid body and the rotating part, respectively. It is seen that the body with nearly constant Doppler and the rotating part with fast changing Doppler are separated.

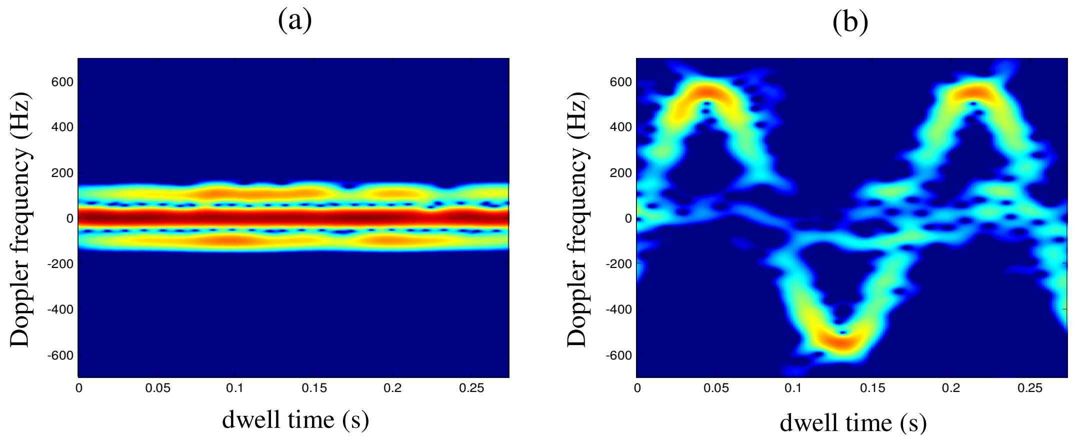

Fig. 5.6 Separated body and rotating part signal. (a) Spectrogram of the three main body scatterers. (b) Spectrogram of the rotating part.

The same procedure is used to parameterize and separate the radar signals from range cells 60 to 70. After removing the rotating part interference, the final ISAR image is shown in Figure 5.7. The five scatterers of the static body are now correctly focused. To get more information about the rotation motion, an autocorrelation analysis of the separated rotating point signal is shown in Figure 5.8a. The period of the rotation motion is determined to be 0.15sec from this figure. This agrees with the truth rotation rate of 6.67Hz. For comparison, the autocorrelation of the raw radar signal before separation is shown in Figure 5.8b. It is difficult to detect the periodicity from the plot as the rotating scatterer signal is heavily contaminated by the large body return.

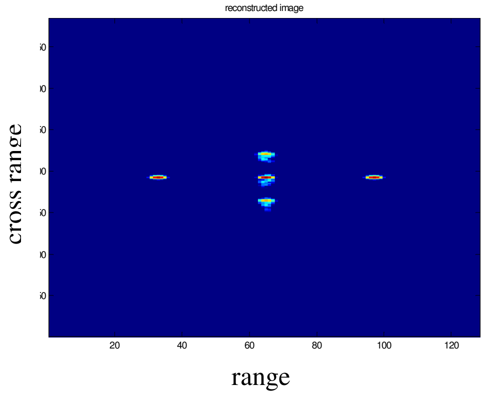

Fig. 5.7 Reconstructed ISAR image using the main body signals only.

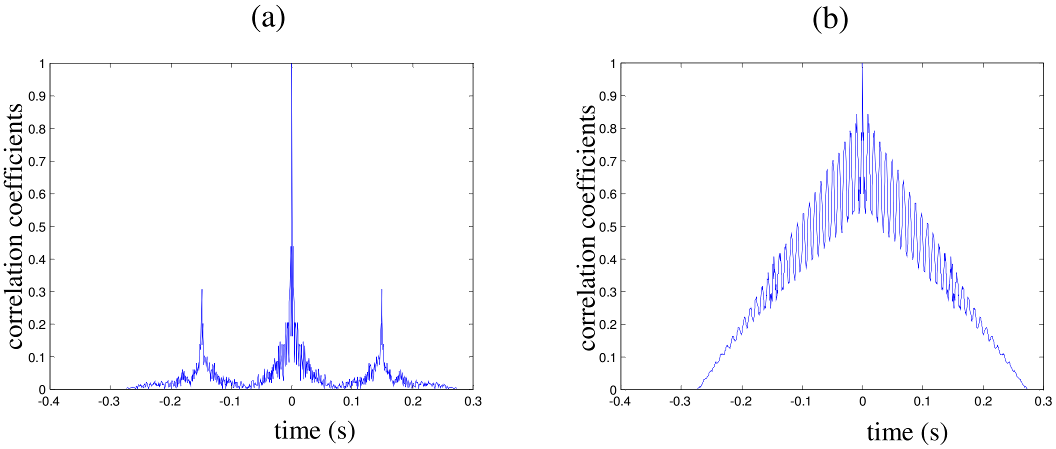

Fig. 5.8 Rotation rate estimation using autocorrelation. (a) Result from the rotating part signal after separation. (b) Result from the original signal before separation.

5.4 Measurement Data Results

The algorithm is next applied to two sets of measurement data. The first data set is the radar data collected from an in-flight aircraft during the frontal view of the target. The second data set is the radar data collected from a walking person. In both cases, the goal is to separate the main body signal from the rotating part return for better target feature extraction.

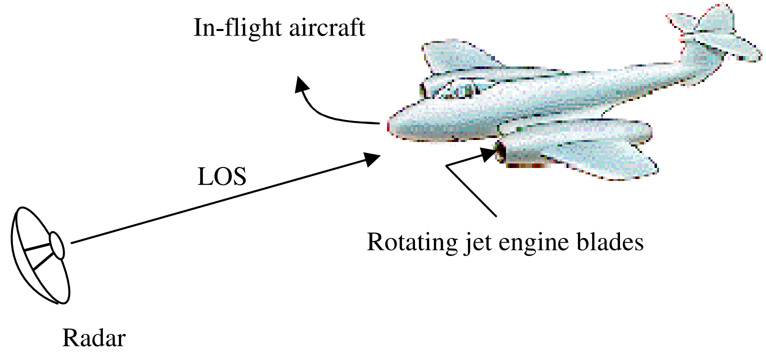

Fig. 5.9 ISAR imaging of an aircraft during frontal view.

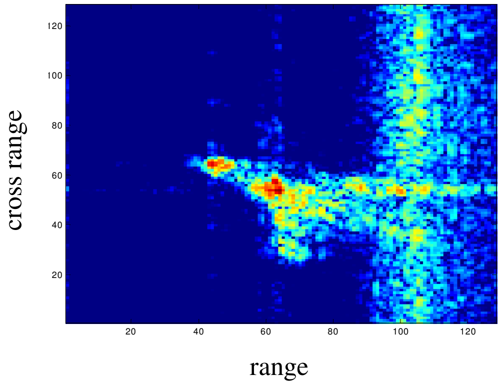

Fig. 5.10 ISAR image of the aircraft with JEM lines.

5.4.1 Jet Engine Modulation Removal from an In-flight Aircraft

The geometry of the problem is shown in Figure 5.9. The radar collects backscattering data from an in-flight aircraft. The resulting ISAR image obtained using a joint time-frequency based motion compensation algorithm [9] is shown in

Figure 5.10. A vertical noisy band due to the rotating engine blades is observed, which is the well-known jet engine modulation (JEM) phenomenon [19]. The geometry of the aircraft body is obscured due to the presence of the JEM lines.

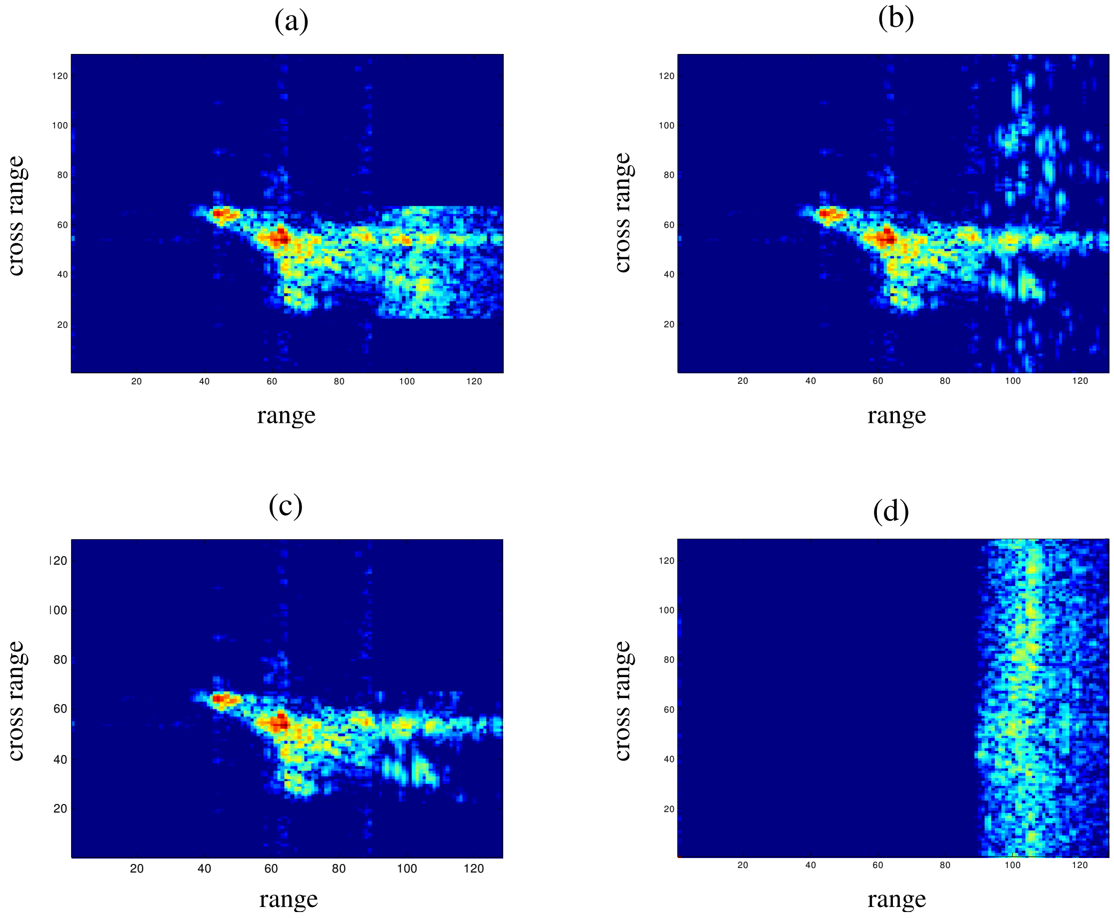

Fig. 5.11 Aircraft body and JEM line separation. (a) Body ISAR image with Doppler frequency gating only. (b) Body ISAR image with Doppler rate gating only. (b) Body ISAR image based on both Doppler frequency and Doppler rate parameters. (d) Separated JEM signal.

Simple Doppler gating is typically used to alleviate the problem. The result in Figure 5.11a is generated by putting zeros in cross range cells 1 to 32 and 62 to 128 in the image area with JEM lines. The high Doppler frequency components in the jet engine return are removed in this manner. However, it is seen that in areas where the JEM lines overlap with the target image, this technique does not work well, as it cannot distinguish the aircraft body signal from the JEM signal with low Doppler frequency.

Using the chirplet-based adaptive signal representation, the radar signal is first parameterized. Figure 5.11b is the reconstructed ISAR image using a separation criterion based on β_k only, i.e., those chirplet bases with large β_k from the parameterized signal are removed. It is much better than Figure 5.11a in revealing the aircraft body feature. This confirms the previous observation that the Doppler rate is a better discriminator than the Doppler frequency in separating the two signals. Finally, both β_k and f_k are used to separate the two signals. The aircraft body image reconstructed from chirplet bases with both small β_k and small f_k is shown in Figure 5.11c. An even better representation of the aircraft body feature is seen in the JEM region. The JEM signal is also displayed in Figure 5.11d. The signal is aliased because of the low PRF of the radar in comparison with the rotation rate of the engine blades. This example shows that this algorithm works despite the strong Doppler aliasing of the rotating part signal.

5.4.2 Arm Swing Rate Estimation from a Walking Person

The second data set is the measured radar data collected from a walking person. The geometry of the problem is shown in Figure 5.12. Two types of motion are involved: the translation motion of the person's body and the swinging motion of the arms (or legs). Figure 5.13 shows the range profiles after coarse range alignment using amplitude correlation. Due to the limited range resolution relative to the target size, it is very hard to tell any useful features about either the body or the arms in this figure. Figure 5.14 is the spectrogram of the radar signal through range cell 32. Interesting target features are revealed in this figure. The horizontal Doppler line is due to the body motion as the person walks at a relatively constant speed during the 1.28*s* dwell interval. The sinusoidal-like curve shows the micro-Doppler phenomenon from the swinging arm motion. The Doppler spread is caused by the varying speed of the arm and the changing angle between the instantaneous swinging motion and the radar incident wave. The periodicity of the arm motion is also observed.

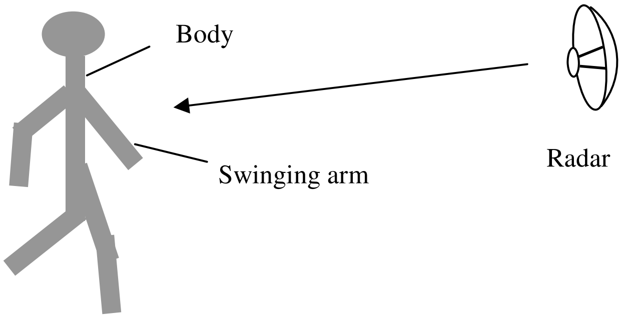

Fig. 5.12 ISAR imaging of a walking person.

To separate the body and the arm returns, the adaptive chirplet representation is applied. After the parameterization, the body return is again separated from the arm return by classifying those bases with large Doppler frequency f_k or large Doppler rate β_k as contributions from the arms. The spectrograms of the separated body and arm signals are shown in Figures 5.15a and 5.15b, respectively. The main features about the target are kept after the separation, indicating good accuracy of the parameterization. A significant de-noising effect is also observed from the parameterization. This is because noise in the measured data does not have the time-frequency characteristics of a chirplet and it is left in the residual signal after the parameterization. The arm-swing period can be easily estimated from the arm-only data by taking the autocorrelation of the time sequence. The peaks in Figure 5.16a correspond to the period of the signal, which is found to be 0.44*s*. Based on this swing rate and the speed of the person (2.3*m/s*) estimated from the same radar data, the stride size of the person is determined to be about 1.0*m*. For comparison, the autocorrelation of the original data without the joint time-frequency processing is also generated (Figure 5.16b). In that case, the radar return from the arm is overshadowed by the body return and the peaks in the autocorrelation function are significantly less pronounced.

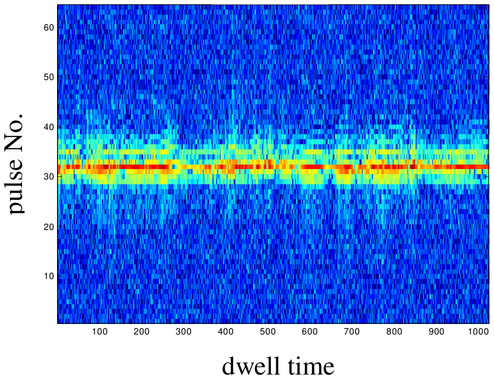

Fig. 5.13 Radar data after range compression.

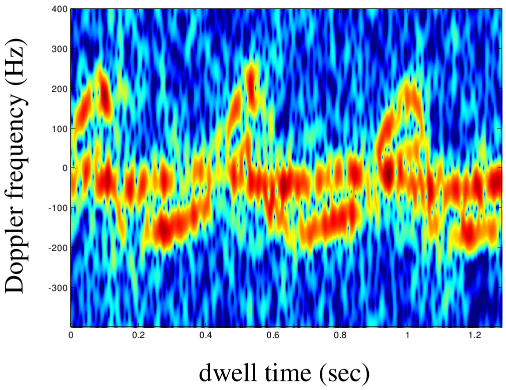

Fig. 5.14 Spectrogram of the radar signal containing body and arm components.

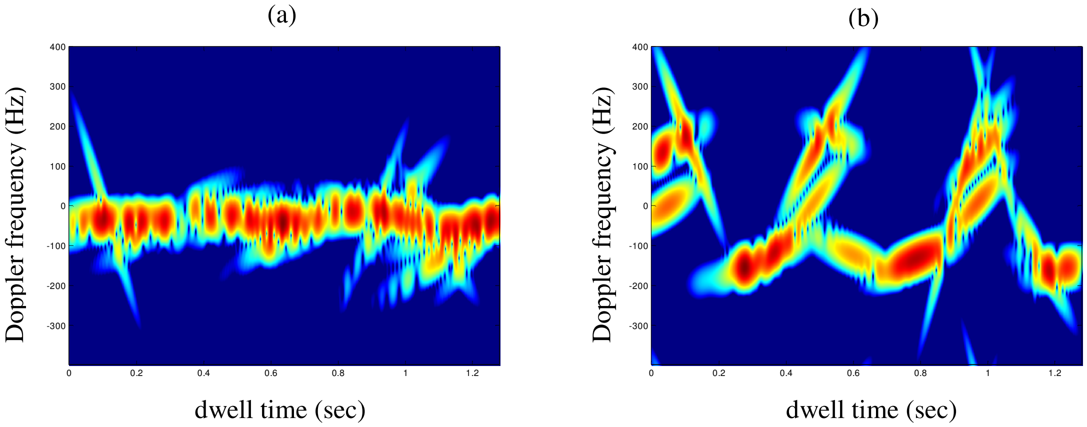

Fig. 5.15 Separated signal components of (a) the body, and (b) the swinging arm.

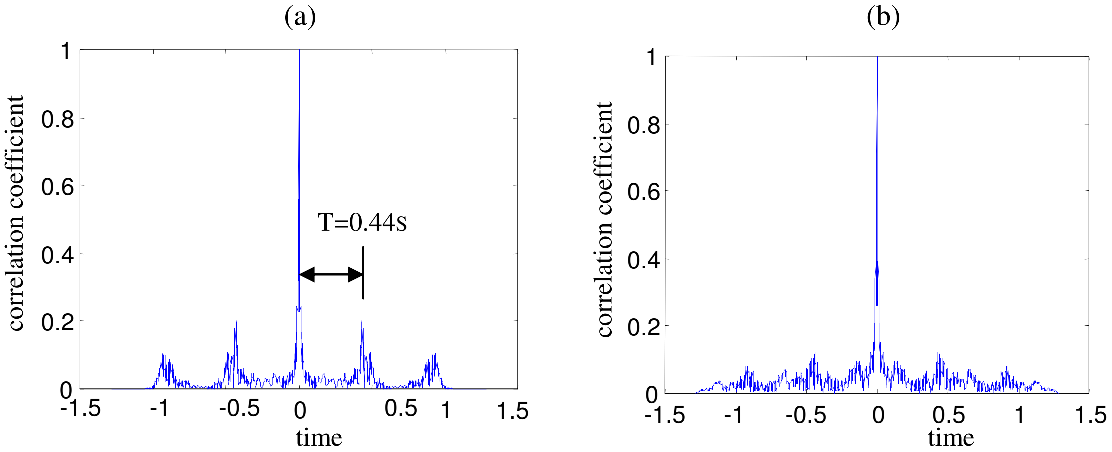

Fig. 5.16 Arm swing rate estimation using autocorrelation.
(a) After signal separation. (b) Before signal separation.

5.5 Conclusions

In this chapter, a chirplet-based adaptive signal representation algorithm is applied to extract features from ISAR data of a target with a rigid main body and a rotating part. Because the micro-Doppler feature of the rotating part is very different from the body Doppler, the two interfere with each other if processed together. To overcome this problem, the two parts are parameterized and separated using the adaptive signal representation. In particular, after formulating an AM-FM model for the radar signal, the four-parameter chirplet basis is used to account for the time and frequency localization of the signal. After the parameterization, the separation is achieved by a criterion based on the extracted Doppler frequency and Doppler rate parameters. The algorithm has been successfully tested with point scatterer simulations and applied to two measurement data sets. In the aircraft data, a better aircraft body image is reconstructed after the separation. In the walking person data, a more accurate estimation of the arm swing rate is acheived. The results demonstrate the potential application of this algorithm for target identification using ISAR data from non-rigid body targets.

Chapter 6 Use of Genetic Algorithms in ISAR Imaging of Targets with Higher Order Motion

In this chapter, genetic algorithms (GA) are proposed for inverse synthetic aperture radar imaging. GA is used for motion parameters search in place of exhaustive search in the adaptive joint time-frequency algorithm. While maintaining the same accuracy, GA has lower computational complexity, especially for targets with higher order motions.

6.1 Introduction

As discussed in previous chapters, phase estimation is critical in fine motion compensation. Compared to the amplitude, the phase of the radar signal is much more sensitive to the change in range. Based on the concept of signal parameterization reported in [34, 40], an adaptive joint time-frequency (AJTF) algorithm was proposed in [11] for phase estimation of a prominent point scatterer. In this method, the target motion is modeled as a polynomial function and an exhaustive search procedure is used to find the motion parameters that are embedded in the phase of the prominent point scatterer. While the performance of this algorithm is very good [23], the main bottleneck in this procedure is the computational complexity associated with the parameter search. When the target motion is highly irregular, i.e., when the number of parameters needed to model the motion is large, the use of the exhaustive search becomes prohibitively expensive.

In this chapter, the objective is to reduce the computation time associated with the motion parameter search in the AJTF procedure. The proposed approach is to incorporate genetic algorithms (GA) [42] into the AJTF search process. (Some preliminary work on this topic was reported in [35].) In contrast with conventional optimization methods, GA is a population-based, statistical search technique. It borrows such concepts as inheritance and mutation from the biological evolution process [43]. As a global optimization technique, GA is known to be very easy to implement and applicable to many design and inverse problems [44].

This chapter is organized as follows. In Sections 6.2 and 6.3, the methodology is outlined. The AJTF analysis for ISAR motion compensation is described in Section 6.2. Genetic algorithms are introduced in Section 6.3. The next two sections include results and analysis. In Section 6.4, simulations with point scatterers are provided to validate the use of GA for phase estimation. Measurement data processing results are shown in Section 6.5. Finally, conclusions are given in Section 6.6.

6.2 ISAR Motion Compensation Using Joint Time-Frequency Projection

In this chapter, the attention is restricted to rigid body targets with a fixed rotational axis. It is also assumed that the target undergoes only a small angular rotation within the dwell interval. Under these assumptions[1], a two-dimensional point

---

[1] The conventional motion assumptions for ISAR imaging are considered in this chapter. Those assumptions may not hold for moving ground vehicles or small ships. The reader is referred to [49-51] for a detailed discussion of those more challenging scenarios.

scatterer model relates the radar data to a moving target through the following equation

$$E(f,t_D)=\sum_i \sigma_i \exp\{-j\frac{4\pi f}{c}[r(t_D)+x_i+y_i\varphi(t_D)]\}\tag{6.1}$$

where f is the frequency and t_D is the dwell time. In this model, the radar data is comprised of the sum of responses from a collection of point scatterers. (x_i,y_i) denotes the point scatterer position while σ_i denotes the scatterer strength. The target motion includes both translation motion $r(t_D)$ and rotational motion $\varphi(t_D)$.

After range compression and range alignment to place all the point scatterers in their correct range bins, the radar signal through one range cell r can be expressed in the form of

$$E_r(t_D)=\sum_i \sigma_i \exp\{-j\frac{4\pi f_0}{c}[\Delta r(t_D)+x_i+y_i\varphi(t_D)])\tag{6.2}$$

where f_0 is the center frequency of the radar and the index includes only those point scatterers in the particular range cell. The residual translation motion is depicted as $\Delta r(t_D)$. After the coarse alignment procedure, the residual translation motion is smaller than the range resolution. However, it can still be larger than the radar wavelength. Both the residual translation motion $\Delta r(t_D)$ and the rotational motion $\varphi(t_D)$ can be expanded into polynomial functions of the dwell time as

$$\begin{aligned}&\Delta r(t_D)=a_1t_D+a_2t_D^2+a_3t_D^3\ldots\\&\varphi(t_D)=b_1t_D+b_2t_D^2+b_3t_D^3\ldots\end{aligned}\tag{6.3}$$

where any coefficients beyond the first order are detrimental to ISAR image formation. To solve the ISAR motion compensation problem, these motion parameters are needed to be determined and the unwanted nonlinear phase terms from the radar data are needed to removed.

This task can be accomplished using the AJTF procedure [11]. The essential idea of this procedure is to find the basis function that most resembles the strongest signal component in equation (6.2). For problem here, a basis function in the form of

$$h(t_D) = \exp[-j\frac{4\pi f_0}{c}(f_1 t_D + f_2 t_D^2 + f_3 t_D^3 ..)] \tag{6.4}$$

is used. The best basis is found by searching for parameters f_1, f_2, f_3, … that maximize the projection from the radar signal onto the basis, i.e.,

$$< f_1, f_2, f_3, \cdots >= \arg\max |< E_r(t_D), h(t_D) >| \tag{6.5}$$

where the projection is formulated as the inner product of the two functions as

$$< E_r(t_D), h(t_D) >= \int E_r(t_D) h^*(t_D) dt_D \tag{6.6}$$

In eq. (6.5), the linear coefficient f_1 can be found efficiently with the fast Fourier transform (FFT). Coefficients for the nonlinear phase terms, f_2, f_3, …, must be determined through a more time-consuming search.

After the motion parameters of the prominent point scatterer are found, the translation motion compensation is carried out by multiplying the radar data with the conjugate of this basis. Since all the point scatterers share the same translation motion in equation (6.2), this operation will remove the translation motion of the whole target. Rotational motion compensation can also be carried out by estimating the phase of a second point scatterer in a different range cell. After phase estimation, the data can be resampled in dwell time to make the phase linear [3, 41].

6.3 Use of Genetic Algorithms for Phase Parameter Search

As discussed in the last section, ISAR motion compensation can be formulated as a parameterization process for both translation motion and rotational motion. In [11], a brute-force search procedure is employed to carry out the parameterization. This means that the solution space is exhaustively searched for the maximum projection. Genetic algorithms (GA) are investigated here to search for the motion parameters to reduce the computation time. It should be pointed out that although a structured tree-search is an easy and straightforward way to decrease the computational complexity, it does not always lead to a global optimum.

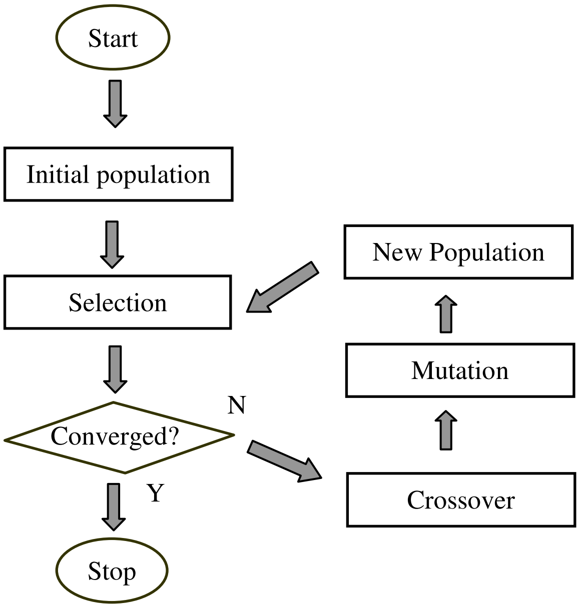

Fig. 6.1 Flowchart of GA.

GA is a global optimization method based on concepts from ecological systems [42, 43, 45]. The flowchart of a typical GA process is illustrated in Figure 6.1. It starts by setting up the parameters for both the physical problem and the GA implementation. GA operates on a population of many individuals. The initial population is randomly generated within the searching space. The goodness of the solution is then evaluated based on an objective function. The objective function is chosen as the projection magnitude from the radar signal onto the basis function (see equation (6.5)) (although other objective functions such as entropy can also be used). The search is carried out in a range cell with a prominent point scatterer. When such a good range cell is not available, multiple range cells can be used to improve the GA phase estimation accuracy. If the solution is satisfactory, the process is done. Otherwise, a new generation is produced for the next evaluation-reproduction iteration. To make up individuals in the new generation, some good parents are selected from the previous generation and two operations called crossover and mutation are applied to produce children in the next generation. Whether or not crossover and mutation occur is determined randomly. The crossover and mutation probabilities are chosen based on the tradeoff between two conflicting requirements. Increasing the variation in the new generation brings a chance for better solutions, but it tends to lose the features of the good solutions from the previous generation.

Roughly speaking, there are two kinds of GA. One is binary-coded GA [42]. The other is real-coded GA [46]. In the former, the physical parameters to be searched are first discretized into binary bits. There is a one-to-one mapping between a physical parameter C and its N-bit binary representation $c_1, c_2, \dots, c_N$ as follows:

$$C = \frac{C_{\max} - C_{\min}}{2^N - 1} \sum_{i=1}^{N} c_i 2^{i-1} + C_{\min} \tag{6.7}$$

where the $[C_{min}, C_{max}]$ is the valid search space for C. A candidate solution of the problem is expressed in the form of a chromosome, which is the collection of bits representing all the parameters. For crossover, a random break point in the chromosome is picked. The bits before the point from one parent are combined with the bits after the point from another parent to form one child. Another child is generated in the reverse fashion. For mutation, a single bit is randomly picked and its valued is inverted. The crossover and mutation operations for binary-coded GA are depicted in Figure 6.2a.

(a)

Crossover $\left.\begin{array}{r}\mathbf{10111101}\\ \mathit{01101010}\end{array}\right\}\begin{array}{l}\mathbf{1011}\mathit{1010}\\ \mathit{0110}\mathbf{1101}\end{array}$

Mutation $\mathbf{10\underline{1}11101} \rightarrow \mathbf{10\underline{0}11101}$

(b)

Crossover $\left.\begin{array}{r}\boldsymbol{C_1}\\ \boldsymbol{C_2}\end{array}\right\}\begin{array}{l}\alpha \boldsymbol{P_1} + (1-\alpha)\boldsymbol{P_2}\\ (1-\alpha)\boldsymbol{P_1} + \alpha \boldsymbol{P_2}\end{array}$

Mutation $\boldsymbol{C} \rightarrow \alpha \boldsymbol{P} + (1-\alpha)\boldsymbol{P_e}$

Fig. 6.2 Examples of crossover and mutation operations in binary and real-coded GA. (a) Binary-coded GA. (b) Real-coded GA.

In real-coded GA, there is no coding-decoding process and the algorithm directly operates on the physical parameters. For crossover, a linear combination is usually used as follows

$$\begin{cases} C_1 = \alpha P_1 + (1-\alpha) P_2 \\ C_2 = (1-\alpha) P_1 + \alpha P_2 \end{cases} \tag{6.8}$$

where two children (C_1, C_2) are reproduced from two parents (P_1,P_2). α is a random number between 0 and 1 to ensure that the new parameters will not fall out of range. For mutation, a child C that is different from the parent P is needed. For this purpose, a solution P_e is picked up randomly from the searching space and linearly combined with P to generate C as in equation (6.8). The crossover and mutation operations for real-coded GA are depicted in Figure 6.2b.

The basic theory in GA, the schemata theory, seems to favor the use of binary-coded GA [45]. Most work on GA has followed this path. Recently, researchers have also experimented with real-coded GA and have observed some advantages in convenience and accuracy [47]. In the next section, both binary-coded and real-coded GA will be tested in the phase estimation problem.

The GA process is usually stopped using criteria based on the performance of the available solutions in the present generation. In this chapter, the true maximum projection value is not known. Therefore, the GA process is stopped when the projection value does not increase after a certain number of generations.

6.4 Point Scatterer Simulation

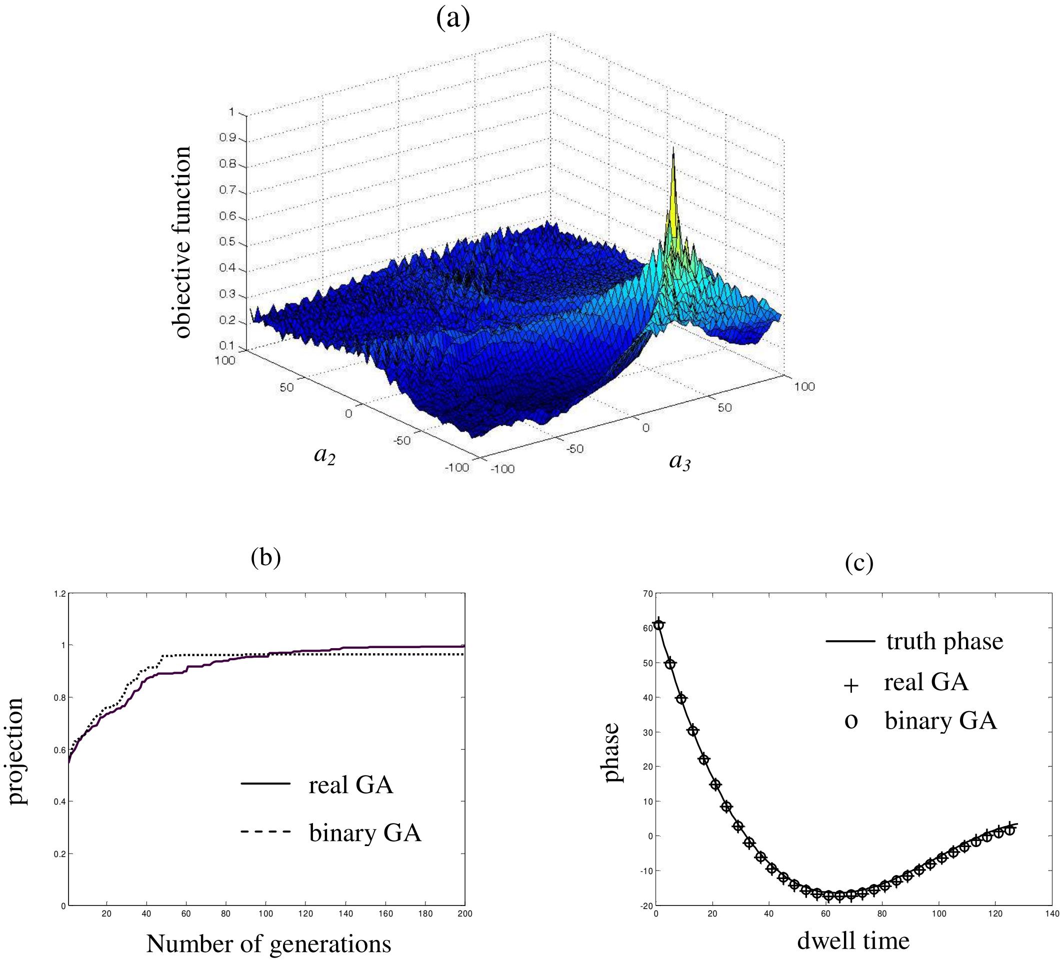

Fig. 6.3 GA for third-order phase estimation. (a) Multi-modal objective function. (b) GA convergence curves. (c) GA-estimated phase compared to the original truth phase.

Point scatterer simulations are first used to test the use of GA for ISAR motion compensation. The accuracy of GA phase estimation is first tested. In this example, two point scatterers with amplitudes 1 and 0.2 are used. They are located within one range cell and contain third-order translation motion (i.e., the coefficients

a_1, a_2 and a_3 in equation (6.3) are significant while all higher-order coefficients are zero). Both binary-coded GA and real-coded GA are run to search for a_2 and a_3 for this simple phase estimation problem. The population size is 50. In both cases, the crossover probability is 0.8 and the mutation probability is 0.3. For exhaustive search, the search for a_2 and a_3 is carried out on a 128 by 128 grid. A 7-bit representation is chosen in binary-coded GA and the same discrete space is searched as in the exhaustive search. The actual objective function surface is plotted in Figure 6.3a. Many local maxima are observed, indicating this would be a challenging problem for a local optimization method. Figure 6.3b shows the GA convergence curve, with the real-coded GA result in solid line and the binary-coded GA result in dashed line. Since GA is a statistical approach, not exactly the same result is obtained from each GA run. To decrease the statistical variation, the results in Figure 6.3b are obtained by averaging over 20 GA runs. It is seen that after about 150 generations the two projection curves nearly converge to the truth value of 1. It is also observed that real-coded GA produces a slightly higher projection value. Figure 6.3c shows the resulting phase from a single GA run after 200 generations. The estimated phase from binary-coded GA is plotted in circles, the phase from real-coded GA in crosses, and the original phase function in solid line. Very good agreement among the three results is observed, meaning good accuracy from the two GA results.

In the second example the computational complexity of GA is compared to exhaustive search for different orders of motion. As pointed out earlier, the main problem with exhaustive search for motion parameter extraction is the computational load. This problem becomes more acute when the order of the motion is high. Again, two point scatterers with amplitudes 1 and 0.2 are used. The radar data from these two point scatterers are generated with some preset motion. Exhaustive search, binary-coded GA, and real-coded GA are then applied for the phase estimation problem with different orders of motion. The same GA parameters as in the previous example are used and the results are averaged over 20 runs. The exhaustive search is known to have an exponential complexity of *O(exp(n))*. As expected, the resulting computation time in logarithm scale shows up as a straight line in Figure 6.4a. For GA, no theoretical complexity formulation is available in general. (The complexity of *O(n log n)* is claimed for selected test functions in [48].) Both binary-coded GA and real-coded GA are run up to sixth-order motion (i.e., search for 5 parameters) and plot the results in Figure 6.4a. It is observed that both binary-coded GA and real-coded GA have much lower complexity than exhaustive search. The difference in complexity between the two GA is only minor. The projection values from binary-coded GA and real-coded GA are next plotted in Figure 6.4b as circles and crosses, respectively. It is seen that the real-coded GA results are closer to the truth value of 1.0 than the binary-coded GA results, especially for higher-order motions. Since binary-coded GA searches on a finite grid as in exhaustive search, it can never get solutions that surpass the exhaustive search result. On the other hand, real-coded GA has the ability to search for any real values within the search range. Consequently, real-coded GA has more chance of finding a better solution. The same trend is also observed with measurement data and will be discussed further in the next section.

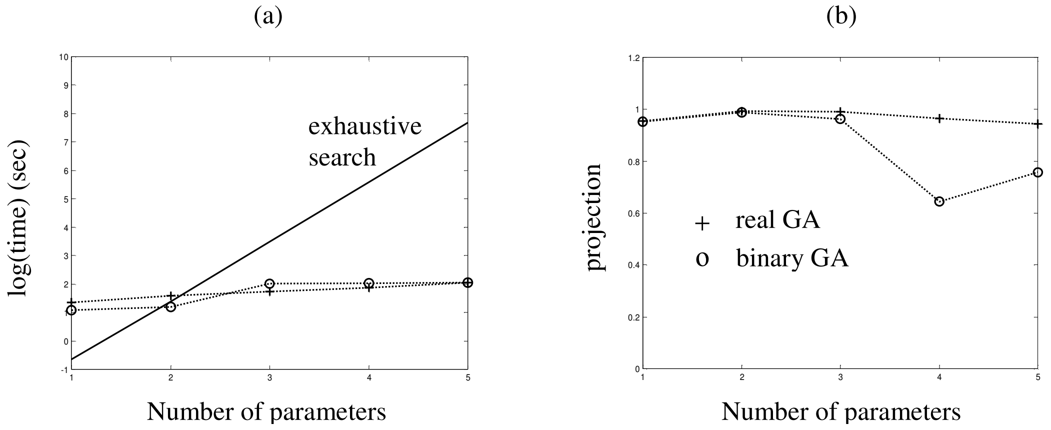

Fig. 6.4 Performance of GA compared to exhaustive search. (a) Computational complexity. (b) Accuracy.

6.5 Measurement Data Processing

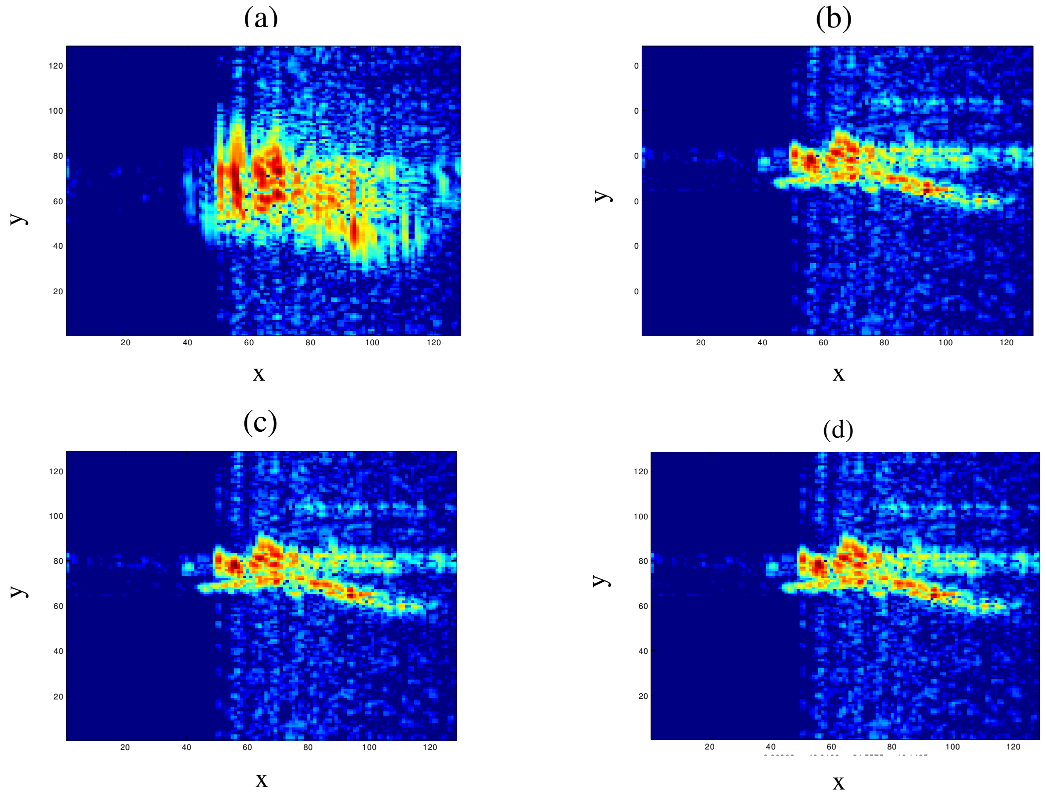

Fig. 6.5 Translation motion compensation applied to measurement data using a third-order motion model. (a) Image before fine motion compensation. (b) Binary-coded GA. (c) Real-coded GA. (d) Exhaustive search.

GA is next applied on some measurement data. The data were collected from an in-flight aircraft using ground radar. 128 pulses are processed to form an ISAR image. This corresponds to an imaging interval of about 2.5 seconds. GA is evaluated for fine motion compensation. For the first data set, the image without any fine motion compensation is shown in Figure 6.5a. This image is unfocused due to the residual motion. A range cell with a dominant scatterer (range cell 79) is selected and GA is applied to estimate the phase based on a third-order translation motion model. The resulting images from binary-coded and real-coded GA are shown in Figures 6.5b and 6.5c, respectively. It is observed that the two GA images are as focused as the reference image in Figure 6.5d obtained using exhaustive search. The corresponding projection values are 2401 and 2595, as compared to the exhaustive search result of 2401.

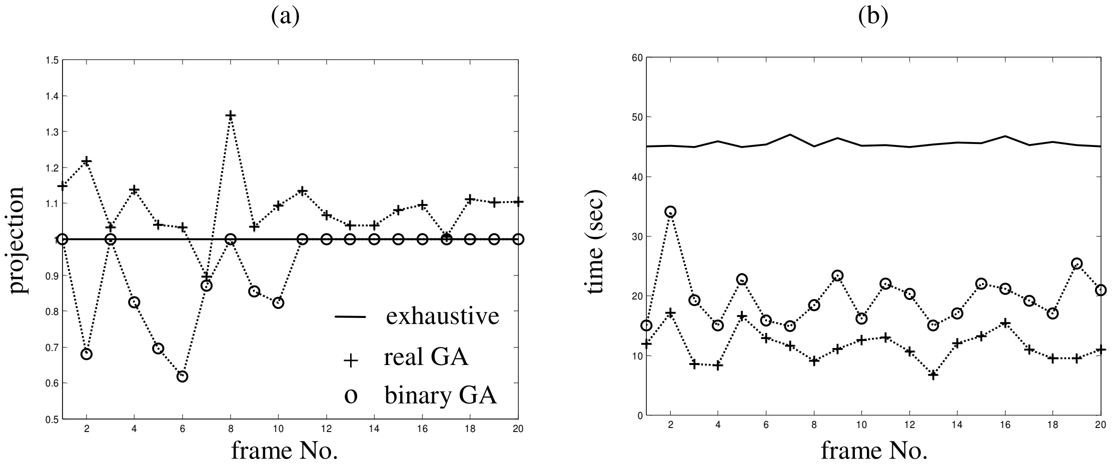

Fig. 6.6 Comparison of the performance of GA and exhaustive search using measurement data. (a) Projection value. (b) Computation time.

This comparison is continued using 19 other imaging intervals. Figure 6.6a shows the projection values (normalized with respect to the exhaustive search result) for the 20 frames. For 19 out 20 frames, real-coded GA gives larger projection values than exhaustive search. The resulting images are either on par or slightly better focused than those obtained from exhaustive search. For binary-coded GA, 7 frames have lower projection values and are of inferior image quality to those from exhaustive search. The other 13 frames have exactly the same projection values as the exhaustive search result. Similar to the conclusion earlier based on the simulation data, the experience with the measurement data indicates that real-coded GA consistently outperforms binary-coded GA in terms of accuracy. The computation time using Matlab codes on a Pentium III 750MHz PC is summarized in Figure 6.6b. While there is little change in the computational time for exhaustive search from one frame to another, the times for binary-coded and real-coded GA exhibit large variations in these single run results due to the statistical nature of GA. The average times for the binary-coded and real-coded GA are 19.5 seconds and 11.5 seconds, respectively. This is compared to the 45.5 seconds from exhaustive search. Finally, it is noted that for these 20 frames the third-order model is adequate to model the translation motion. Inclusion of higher-order translation motion or rotational motion does not improve the image quality for this data set.

For a second data set, third-order translation motion compensation is first applied using real-coded GA. The resulting image is shown in Figure 6.7a. It is seen that the selected dominant point scatterer at range cell 64 is not well focused. This means that the target contains higher motion that cannot be fully compensated by the third order motion model. This fact is also revealed by the spectrogram of the

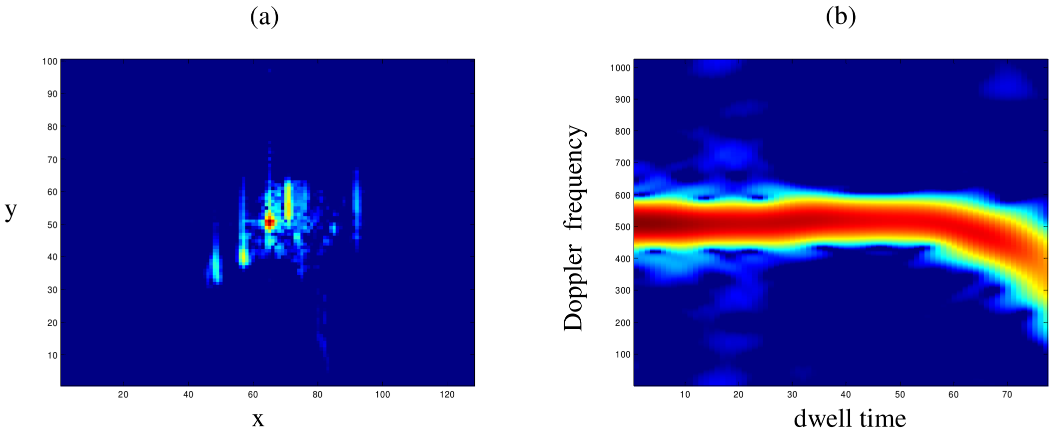

Fig. 6.7 Motion compensation example for another measurement data set. (a) Image after third-order translation motion compensation using real-coded GA. (b) Spectrogram of the signal in range cell 64.

compensated signal in Figure 6.7b, as a curved JTF trajectory is observed for the scatterer. Next, a fourth-order motion model is tried and the real-coded GA result is shown in Figure 6.8a. From this figure, the reference point scatterer is better focused and the spectrogram of the signal is straightened in Figure 6.8b. Fifth-order translation motion is also attempted, and the result does not show much improvement. However, it is observed that other point scatterers in Figure 6.8a are still smeared. This is confirmed by the spectrogram of the signal at a different range cell (number 71) shown in Figure 6.8c, which shows that the signal trajectory is curved in the spectrogram. Thus rotational motion must exist in this data. Fourth-order rotational motion compensation using real-coded GA. As shown in Figure 6.9a, the whole target is much better focused after the compensation. The spectrograms of the signal at both range cells become straightened in Figures 6.9b and 6.9c. While real-coded GA takes 45 seconds for the phase estimation problem, the computation time for fourth-order exhaustive search is estimated to be over 50 minutes based on the complexity curve in Figure 6.4a. Therefore, the time savings of GA over exhaustive search is quite significant in this real-world example.

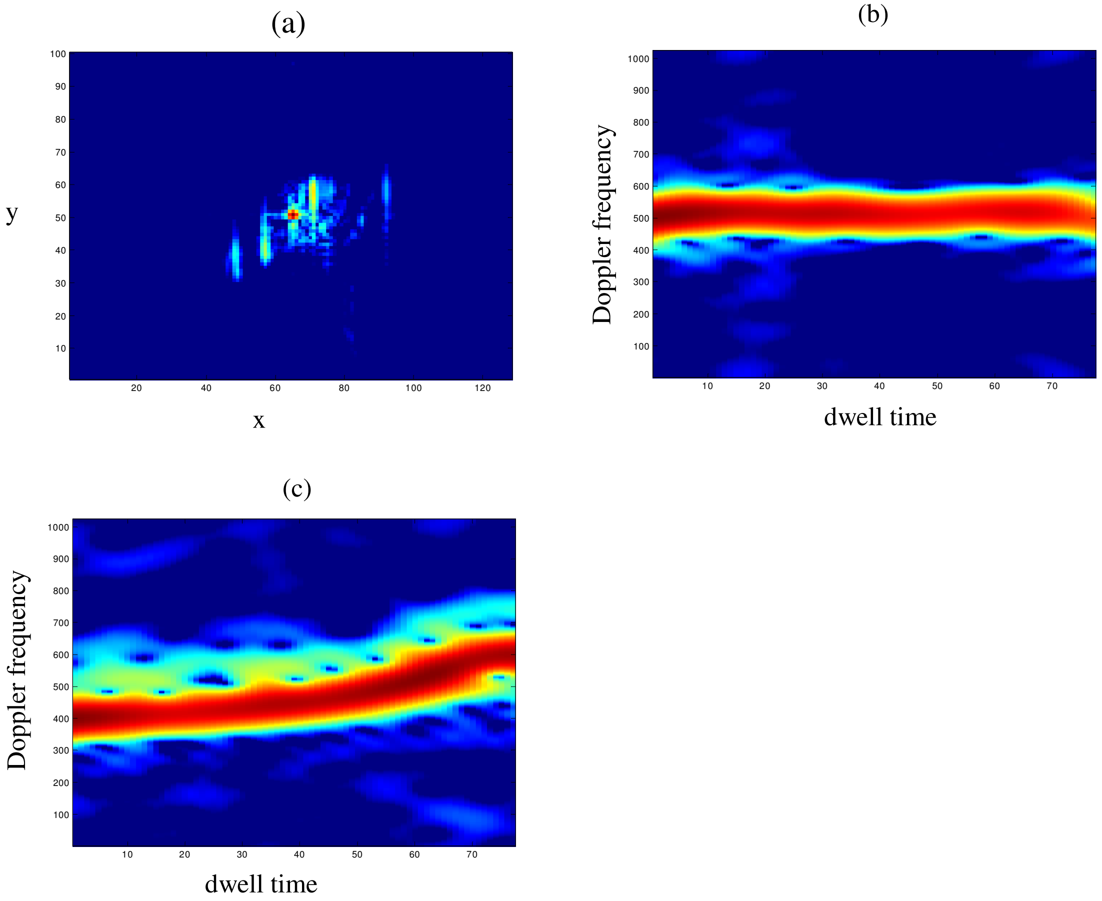

Fig. 6.8 Higher-order translation motion compensation. (a) Image after fourth-order translation motion compensation using real-coded GA. (b) Spectrogram of the signal in range cell 64. (c) Spectrogram of the signal in range cell 71.

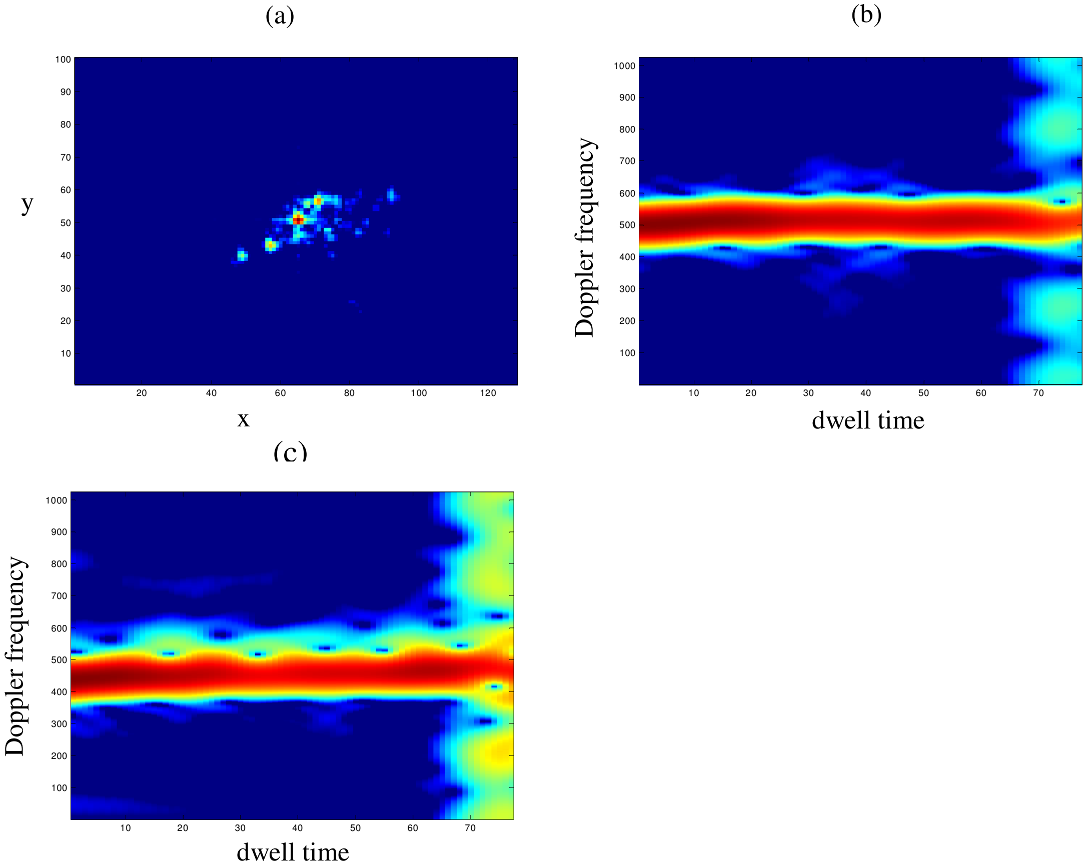

Fig. 6.9 Higher-order rotational motion compensation. (a) Image after fourth-order rotational motion compensation using real-coded GA. (b) Spectrogram of the signal in range cell 64. (c) Spectrogram of the signal in range cell 71.

6.6 Conclusions

In this chapter, genetic algorithms have been applied to ISAR motion compensation. Based on the adaptive joint time-frequency analysis, GA is used in the phase estimation of prominent point scatterers on the target. The resulting parameterized phases are then used for translation and rotational motion compensation. Both binary-coded GA and real-coded GA have been implemented and tested using simulation and measurement data. It is found that real-coded GA outperforms binary-coded GA in terms of accuracy in the phase estimation problem. It is also shown that the computational complexity of the GA search is much less than that of exhaustive search. The time savings can become especially significant when the target exhibits higher order motions.

Chapter 7 Conclusions

In this chapter, a summary of the previous chapters is given. The main contributions of the dissertation are also highlighted. Further work on ISAR imaging from moving targets is discussed at the end of the chapter.

7.1 Summary

Chapter 1 is the introduction to ISAR imaging. The problem of ISAR imaging is defined, including a comparison of ISAR with SAR and IFSAR imaging modes, two dimensional (frequency, angle) data collection to achieve range and cross-range resolution, and the applications of ISAR imaging. For better understanding of the later chapters, background knowledge about ISAR imaging is covered, including the point scatterer model and the standard motion compensation process. The dissertation is mainly motivated by the complex target motions which violates the motion assumptions used in conventional ISAR imaging algorithms.

Chapter 2 is a comparison of ISAR images from measured data and synthetic signatures. three sets of ISAR images have been generated, including JTF bind motion compensated ISAR images, GPS truth motion compensated ISAR images, and Xpatch simulated ISAR images. Correlation analysis and visual examination show good overall matches among the three image sets. Two problems for ISAR imaging of aircraft have also been identified. The first case of problem arises when the target has 2D motion with fixed rotational axis during the imaging interval. The other happens during the front view of the aircraft when the target with rotating jet engine blades is a non-rigid body.

In chapter 3, an algorithm to detect the presence of 3D motion from the radar data is presented. A discussion of 2D motion and 3D motion model is made. The implications of using existing motion compensation algorithms for targets with 3D motions are illustrated. A 3D motion detection algorithm has been proposed based on phase linearity analysis of multiple point scatterers. The detection algorithm is applied to two measurement data sets. One is from an aircraft with on-board GPS sensors. The detection result is compared with the truth motion data. The other one is from ship over the sea surface with no truth motion data. A good correlation between the degree of 3D motion and quality of resulting ISAR images is observed.

Chapter 4 deals with the 3D image reconstruction from targets with 3D motions. When the target motion data is available, 3D image reconstruction is possible. The traditional Fourier-based method suffers from the high side-lobes with undersampled radar data over the angular aperture in real-world situation. The adaptive feature extraction algorithm has been applied to overcome this problem. Simulated model aircraft data results show that more target features are contained in the reconstructed 3D ISAR image that a 2D image.

In chapter 5, feature extraction from targets with non-rigid body motions is discussed. When a target consists of a main body part and a rotating part, problem arises when traditional ISAR imaging is applied as the rigid-body motion assumption is violated. Based on the AM-FM radar signal model, chirplet is chosen as the basis to adaptively represent the radar signal. After parameterization, the two components can be separated based on the Doppler and the Doppler rate parameters. The algorithm has been applied to measured aircraft data. After the JEM signal is removed, better reconstruction of the aircraft body image is achieved. For the measured radar data from a walking person, a better estimation of the arm swing rate is achieved after the body signal is removed.

Chapter 6 presents the use of genetic algorithms for targets with higher order motions. When the number of parameters to model the target motion is large, the exhaustive search process in JTF phase estimation is very time consuming. Genetic algorithms are used to reduce the computational complexity of phase estimation. Both binary and real-coded GA are studied. Based on both simulation and measurement data, the time savings of GA over exhaustive search can be significant, especially for targets with higher order motions.

7.2 Contributions

The contributions and significance of this dissertation research are summarized below:

1) An evaluation of existing ISAR imaging algorithms is made by comparing JTF motion compensated images with GPS reference ISAR images and Xpatch simulated ISAR image. Good performance of the JTF motion compensation is observed when the 2D rotational motion and rigid-body motion assumption is

applicable. Problems due to the existence of 3D rotational motion and non-rigid body motion are also identified.

2) For the target with 3D rotational motion, an algorithm is developed to detect the existence of 3D motion blindly from the radar data based on the phase linearity analysis. Detected degree of 3D motion is useful information about the target motion and it is helpful for good imaging interval selection. When the target 3D motion is know, adaptive feature extraction is used for 3D image reconstruction from the undersampled radar data. The resulting 3D image provides more detailed target features than a 2D image.

3) For non-rigid body motions, chirplet basis is selected to adaptively represent the AM-FM structure of the radar signal. With adaptive chirplet signal representation, the main body and rotating part signal can be easily separated according to the Doppler and Doppler rate parameters of the extracted bases. Using this method, a better ISAR image of the aircraft body is achieved after the JEM signal is removed from the radar data collected from an in-flight aircraft. Better arm swing rate estimation is also achieved after the body signal is removed from the radar data collected from a walking person.

4) Genetic algorithms are used to reduce the computational complexity of the exhaustive search process in JTF phase estimation. The time savings could be significant when the target has higher order translation or rotational motions.

5) The methods have been tested with point scatterer simulation and applied to measurement data. They are expected to improve the performance of current ISAR imaging algorithms in real-world situations.

7.3 Further work

Many issues still need to be addressed before ISAR imaging as a target identification tool becomes fully operational. First, more work on target feature extraction from ISAR data is needed. Although a focused ISAR image itself contains useful geometrical features, information about the target motion is also needed when the target undergoes a complex motion during the imaging interval. Micro-Doppler feature extraction from a target with rotating parts has been studied in this research. Another interesting example not considered is the vibration motion of the whole body or part of the target. The vibration might indicate the anomaly of the target or its surrounding environment.

Another important topic in radar data processing that warrants further research is the scattering model. Presently, the full wave model is too complex and not useful for field radar data processing. The point scatterer model is exclusively used in this dissertation due to its simplicity and good approximation for single scattering phenomenon. However, image artifacts will arise when there is multiple scattering from a target with duct and cavity-like structures. Though this is a very challenging problem, an intermediate model that incorporate multiple scattering and yet manageable for the real-time radar imaging process might be possible.

Innovative system configuration is another promising research topic in ISAR imaging. The radar systems which generated the measurement data for this dissertation are sophisticated and expensive. With the development of RF and microwave hardware technology and advanced sensor array signal processing techniques, a multifunctional, reconfigurable radar system with better cost performance than before is possible. For example, most of the existing ISAR data come with a fixed PRF, which is usually too low to capture signal from fast moving parts. Along with the existing PRF to resolve the Doppler from the target main body, a radar with multiple or even variable PRF configuration could be useful for micro-Doppler feature extraction.

In summary, an optimal ISAR imaging system relies on developments in data model, signal processing and radar sensor design. A radar data model is needed to better understand the target motion and the wave-target scattering mechanism before useful information can be extracted out of the radar data. Model-based signal processing integrates the data models into the practical operations of the information extraction process. Data diversity through a smart radar system configuration should make information extraction even more robust.

Bibliography

[1] C. C. Chen and H. C. Andrews, "Target motion induced radar imaging," *IEEE Trans. Aerospace Electron. Syst.*, vol. 16, pp.2-14, Jan. 1980.

[2] D. L. Mensa, *High Resolution Radar Imaging*, Artech House, Dedham, MA, 1981.

[3] W. G. Carrara, R. S. Goodman and R. M. Majewski, *Spotlight Synthetic Aperture Radar - Signal Processing and Algorithms*, Artech House, Boston, MA, 1995.

[4] C.A. Balanis, *Advanced Engineering Electromagnetics*, New York, 1989.

[5] M. Hazlett, D.J. Andersh, S.W. Lee, H. Ling, C.L. Yu, "XPATCH: a high-freequency electromagnetic scattering prediction code using shooting and bouncing rays," *Proceedings of SPIE*, vol. 2469, pp. 266-275, Jun. 1995.

[6] *User's Manual for FISC (Fast Illinois Solver Code)*, Center of Computational Electromagnetics, Univ. of Illinois, Champaign, IL, and DEMACO, Inc., Champaign, IL, Jan. 1997.

[7] D. E. Wahl, P. H. Eichel, D. C. Ghiglia and C. V. Jakowatz, "Phase gradient autofocus- a robust tool for high resolution SAR phase correction*," IEEE Trans. Aerospace Electron. Syst.*, vol. 30, no. 3, pp. 827-835, July 1994.

[8] Z. Liu, R. Wu and J. Li, "Complex ISAR imaging of maneuvering targets via the Capon estimator," *IEEE Trans. Signal Processing*, vol. 47, no. 5, pp. 1262-1271, May 1999.

[9] L.C. Trintinalia and H. Ling, "Joint time-frequency ISAR using adaptive processing," *IEEE Trans. Antennas Propagat.*, vol. AP-45, pp. 221-227, Feb. 1997.

[10] V. C. Chen and S. Qian, " Joint time-frequency transform for radar range-Doppler imaging," *IEEE Trans. Aerospace Electron. Syst*., vol. 34, No. 2, pp 486-499, Apr. 1998.

[11] Y. Wang, H. Ling and V. C. Chen, "ISAR motion compensation via adaptive joint time-frequency technique," *IEEE Trans. Aerospace Electron. Syst.*, vol. 34, pp.670-677, Apr. 1998.

[12] A. Ausherman, A. Kozma, J. L. Waker, H.M. Jones and E. C. Poggio, "Developments in radar imaging," *IEEE Trans. Aerospace Electron. Syst.,* vol. 20, pp.363-400, Apr. 1984.

[13] H. Ling, Y. Wang, J. Li, R. Bhalla and V.C. Chen, "ISAR image formation of TIRA data using adaptive joint time-frequency processing," *NATO Sensors and Electronics Technology Symposium on High Resolution Radar Techniques*, Granada, Spain, Mar. 1999.

[14] D. J. Andersh, M. Hazlett, S. W. Lee, D. D. Reeves, D. P. Sullivan and Y. Chu, "XPATCH: a high-frequency electromagnetic-scattering prediction code and environment for complex three-dimensional objects," *IEEE Antennas Propagat. Mag.*, vol.36, pp.65-69, Feb. 1994.

[15] H. Ling, R. Chou and S.W. Lee, "Shooting and bouncing rays: Calculating the RCS of an arbitrary shaped cavity," *IEEE Trans. Antennas Propagat.*, vol. 37, pp.194-205, Feb. 1989.

[16] R. Bhalla and H. Ling, "Image-domain ray-tube integration formula for the shooting and bouncing ray technique," *Radio Science*, vol. 30, pp.1435-1446, Sept.-Oct. 1995.

[17] R. Bhalla and H. Ling, “A fast algorithm for signature prediction and image formation using the shooting and bouncing ray technique,” *IEEE Trans. Antennas Propagat.*, vol. AP-43, pp.727-731, July 1995.

[18] F. E. Nathanson, *Radar Design Principles*, pp.173-183, McGraw-Hill, New York, 1969.

[19] M. Bell and R. A. Grubbs, “JEM modeling and measurement for radar target identification,” *IEEE Trans. Aerospace. Electron. Syst.*, vol. 29, pp. 73-87, 1993.

[20] Y. Wang, H. Ling and V.C. Chen, “Application of adaptive joint time-frequency processing to ISAR image enhancement and Doppler feature extraction for targets with rotating parts,” *SPIE 43rd Annual Meeting, Radar Processing, Technology, and Applications*, pp. 156-163, San Diego, CA, July 1998.

[21] S. Werness, W. Carrara, L. Joyce and D. Franczak, “Moving target imaging algorithms for SAR data,” *IEEE Trans. Aerospace Electron. Syst.*, vol. 26, no. 1, pp. 57-67, Jan. 1990.

[22] V. C. Chen and W. J. Miceli, “Effect of roll, pitch and yaw motions on ISAR imaging,” *SPIE Proc. Radar Processing, Technology and Applications VI*, vol. 3810, pp. 149-158, Denver, CO, Jul. 1999.

[23] J. Li, Y. Wang, R. Bhalla, H. Ling and V. C. Chen, “Comparison of high-resolution ISAR imagery from measured data and synthetic signatures,” *SPIE Proc. Radar Processing, Technology and Applications VI*, vol. 3810, pp. 170-179, Denver, CO, July 1999.

[24] A. W. Rihaczek and S. J. Hershkowitz, “Choosing imaging intervals for identification of small ships,” *SPIE Proc. Radar Processing, Technology and Applications VI*, vol. 3810, pp. 139-148, Denver, CO, July 1999.

[25] S. Xiao and D. C. Munson, “Spotlight-mode SAR imaging of a three-dimensional scene using spectral estimation techniques,” *Proc. IEEE Inter. Geosci. and Remote Sensing Symp.*, vol. 2, pp. 642-644, Seattle, WA, July 1998.

[26] J. T. Mayhan, K. M. Cuomo and J. E. Piou, “High resolution 3D ‘snapshot’ ISAR imaging,” *IEEE Trans. Aerospace Electron. Syst.*, vol. 37, no. 2, pp. 630-641, Apr. 2000.

[27] M. A. Stuff, “Three-dimensional analysis of moving target radar signals: methods and implications for ATR and feature-aided tracking,” *SPIE Proc. Algorithms for Synthetic Aperture Radar Imagery VI,* vol. 3721, pp. 485-496, Aug. 1999.

[28] K. Rosenbach and J. Schiller, "Non co-operative air target identification using radar imagery: identification rate as a function of signal bandwidth," *IEEE 2000 Inter. Radar Conference*, pp. 457-462, Alexandria, VA, May 2000.

[29] T. Sparr, S. E. Hamran and E. Korsbakken, "Estimation and correction of complex target motion effects in inverse synthetic aperture imaging of aircraft," *IEEE 2000 Inter. Radar Conference*, pp. 457-462, Alexandria, VA, May 2000.

[30] H. Ling and J. Li, "Application of adaptive joint time-frequency processing to ISAR image formation," *Proc. of the 10th IEEE workshop on Statistical Signal and Array Processing*, pp. 476-479, Pocono Manor, PA, Aug. 2000.

[31] J. Li, Z. Bi and Z.-S. Liu, "Autofocus and feature extraction in curvilinear SAR via a relaxation-based algorithm," *IEE Proc. Radar, Sonar Navig.*, vol. 146, no. 4, pp. 201-207, Aug. 1999.

[32] Y. Wang and H. Ling, "Adaptive ISAR image construction from nonuniformly undersampled data," *IEEE Trans. Antennas and Propagat.*, vol. 48, pp. 329-331, Feb. 2000.

[33] J. Tsao and B. D. Steinberg, “Reduction of sidelobe and speckle artifacts in microwave imaging: the CLEAN technique,” *IEEE Trans. Antennas and Propagat.*, vol. 36, no.4, pp. 543-556, Apr. 1988.

[34] S. G. Mallat and Z. Zhang, “Matching pursuits with time-frequency dictionaries,” *IEEE Trans. Signal Processing*, vol. 41, no. 12, pp. 3397-3415, Dec. 1993.

[35] J. Li and H. Ling, “ISAR motion detection and compensation using genetic algorithms,” *SPIE Proc. Wavelet Applications VIII*, vol. 4391, pp. 380-388, Orlando, FL, Apr. 2001.

[36] V.C. Chen, “Analysis of radar micro-Doppler with time-frequency transform,” *Proc. of the 10th IEEE workshop on Statistical Signal and Array Processing*, pp. 463-466, Pocono Manor, PA, Aug. 2000.

[37] E. F. Greneker, J. L. Geisheimer, D. Asbell, “Extraction of micro-Doppler data from vehicle targets at x-band frequencies,” *SPIE Proc. Radar Sensor Technology VI*, vol. 4374, pp. 1-9, Orlando, FL, Apr. 2001.

[38] S. Qian, D. Chen and Q. Yin, "Adaptive chirplet based signal approximation," *Proc. ICASSP*, vol. III, pp. 1871-1874, May 1998.

[39] A. Bultan, “A four-parameter atomic decomposition of chirplets,” *IEEE Trans. Signal Processing*, vol. 47, pp. 731-745, Mar. 1999.

[40] S. Qian and D. Chen, “Signal representation using adaptive normalized Gaussian functions,” *Signal Processing*, vol. 36, no. 1, pp. 1-11, Mar. 1994.

[41] A. W. Rihaczek and S. J. Hershkowitz, *Radar Resolution and Complex-Image Analysis*, Artech House, Boston, MA, 1996.

[42] D. E. Goldberg, *Genetic Algorithms in Search, Optimization and Machine Learning*, Addison-Wesley, Reading, MA, 1989.

[43] M. Mitechell and C. E. Taylor, “Evolutionary computation: an overview,” *Annual Review of Ecology and Systematics*, vol. 30, pp. 593-616, 1999.

[44] Y. Rahmat-Samii and E. Michielssen (eds.), *Electromagnetic Optimization by Genetic Algorithms*, John Wiley & Sons, New York, NY, 1999.

[45] J. H. Holland, *Adaptation in Natural and Artificial Systems: an Introductory Analysis with Applications to Biology, Control, and Artificial Intelligence*, The University of Michigan Press, Ann Arbor, MI, 1975.

[46] D. E. Goldberg, “Real-coded genetic algorithms, virtual alphabet, and blocking,” *Complex Systems*, vol. 5, pp. 139-167, 1991.

[47] F. Herrera, M. Lozano, and J. L. Verdegay, “Tackling real-coded genetic algorithms: operators and tools for behavioral analysis,” *Artificial Intelligence Review*, vol. 12, pp. 265-319, 1998.

[48] R. Salomon, “Genetic algorithms and the O(n ln n) complexity on selected test functions,” *Proc. Artificial Neural Networks in Engineering (ANNIE'95)*, pp. 325-330, ASME Press, New York, NY, 1995.

[49] A. W. Rihaczek and S. J. Hershkowitz, *Theory and Practice of Radar Target Identification*, Artech House, Boston, MA, 2000.

[50] J. Li and H. Ling, “An algorithm to detect the presence of 3D target motion from ISAR data,” *Multidimensional Systems and Signal Processing-Special Issue on Radar Signal Processing*, accepted for publication, Aug. 2001.

[51] J. Li and H. Ling, “ISAR feature extraction from non-rigid body targets using adaptive chirplet representation,” *2002 IEEE APS International Symposium Digest*, pp. 294-297, San Antonio, TX, Jun. 2002.

Vita

Junfei Li was born in Hubei, China in 1971, the son of Mingjin Li and Xiaoxiu Chen. He received his B.S. and M.S. degrees in electrical engineering from Northwestern Polytechnical University, Xi'an, China, in 1992 and 1995, respectively. He was a Research Engineer with the Institute of Remote Sensing Applications, Chinese Academy of Sciences from 1995 to 1998. He was a Ph.D. student worked as a Graduate Research Assistant in the Department of Electrical and Computer Engineering at the University of Texas at Austin from 1998 to 2002. His research interests include radar signal processing and imaging, microwave remote sensing, inverse scattering, RF and microwave engineering.

Permanent address: 2501 Lake Austin Blvd Apt H107, Austin, TX 78703

This dissertation was typed by the author.